REPORT 1282

A SPECIAL METHOD FOR FINDING BODY DISTORTIONS THAT REDUCE THE WAVE DRAG OF WING AND BODY COMBINATIONS AT SUPERSONIC SPEEDS [1]

By Harvard Lomax and Max. A. Heaslet

SUMMARY

For a given wing and supersonic Mach number, the problem of shaping an adjoining fuselage so that the combination will have a low wave drag is considered. Only fuselages that can be simulated by singularities (multipoles) distributed along the body axis are studied. However, the optimum variations of such singularities are completely specified in terms of the given wing geometry. An application is made to an elliptic wing having a biconvex section, a thickness-chord ratio equal to 0.05 at the root, and an aspect ratio equal to 3. A comparison of the theoretical results with a wind-tunnel experiment is also presented.

INTRODUCTION

The most simplifying assumptions that still permit the construction of a mathematical model general enough to contain quantitative information about steady three-dimensional supersonic flow are those basic to the development of linearized theory. Of these, the two principal assumptions are that the viscosity effects are negligible and the perturbation velocities are almost everywhere small enough to be neglected relative to the flight or free-stream velocity. Under such restrictions the flow field can be described in terms of a perturbation velocity potential φ obeying the equation

$$\beta^2\varphi_{xx} - \varphi_{yy} - \varphi_{zz} = 0 \tag{1}$$

where $\beta^2 = M^2 - 1$ and the reference coordinate system [2] is shown in figure 1. Further, the wave drag of any object in a flow field governed by equation (1) can be evaluated (see, e. g., ref. 1) by means of the equation

$$D = -\rho_0 \int_{-\infty}^{\infty} dx \int_0^{2\pi} d\theta \left[\lim_{r \to \infty} (r\varphi_r\varphi_x) \right] \tag{2}$$

where x, r, and θ are cylindrical coordinates also defined in figure 1.

General solutions to equation (1) are numerous and classical. In applying these solutions to the interpretation of physical phenomena the usual approach is to fit them to the given boundary conditions, that is, to make the flow field simulated by them conform to the shape of the disturbing object as well as to a uniform free stream at infinity. Hence,

from this point of view, the choice of a type of general solution to be used in analyzing a particular problem with the least mathematical effort depends on the geometric form of the object under consideration. For example, general solutions based on Green's theorem are well adapted to the study of forces on single planar wings in a steady supersonic flow. On the other hand, the general solution given by Lamb (ref. 2)—which is composed of an infinite set of multipole distributions disposed along a line—is well adapted to the study of the flow around fuselage-like objects.

In this report use is made of certain general solutions to equation (1) but with a deviation from the usual approach mentioned above. One considers, in fact, two different kinds of solutions which represent separately, in a given
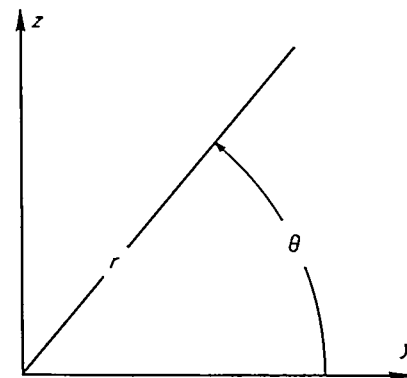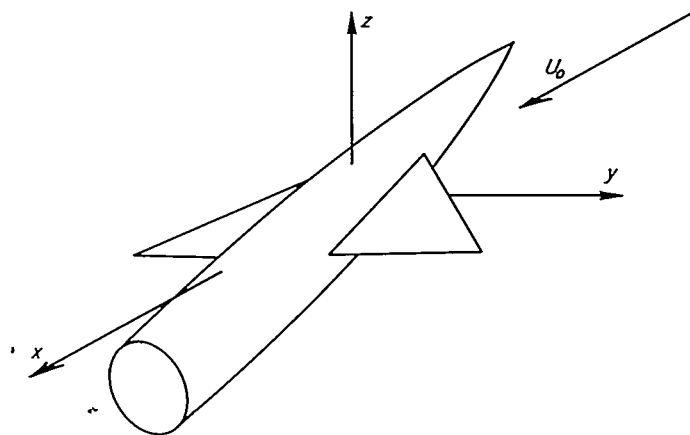

Figure 1.—Reference coordinate systems.

vicinity, different classes of real objects and, by means of equation (2), finds optimum combinations of these solutions from the viewpoint of low wave drag. The analysis involved in solving this problem has, in general, a distinct mathematical advantage over the problem of calculating the drag of a given object; namely, that the immediate problem of finding a shape with a relatively low wave drag is divorced from any detailed reference to the shape itself. It is true, of course, that the stream surface representing this shape must eventually be found and, in fact, a limitation on the applicability of the method is given by the requirement that this shape be real. However, the problem of finding the shape of the object when φ is known is a matter of direct calculation.[3] One should also be careful to notice that the optimum solutions obtained by this procedure are not necessarily true optimums but purely relative to the choice of solutions used in the analysis.

LIST OF IMPORTANT SYMBOLS

A	wing aspect ratio
$A_n(x)$	$(-\beta)^n$ times the nth derivative of the nth multipole distribution $a_n(x)$ (See eq. 16.)
a	semi-root-chord of elliptic wing
$a_n(x)$	strength of nth-order multipole distribution multiplying $\cos n\theta$
$B_n(x)$	$(-\beta)^n$ times the nth derivative of the nth multipole distribution $b_n(x)$
b	semispan of elliptic wing
$b_n(x)$	strength of nth-order multipole distribution multiplying $\sin n\theta$
C_D	drag coefficient, $\dfrac{D}{qS}$
C_p	pressure coefficient, local pressure minus static pressure divided by q
D	wave drag
D_n	wave drag associated with nth-order cancellation multipole distribution (See eq. (59).)
L_0',L_0	maximum fore-and-aft extent of wing equivalent multipole distribution
$L'(\theta),L(\theta)$	maximum fore-and-aft extent of wing equivalent multipole distribution for angle θ
M	free-stream Mach number
q	free-stream dynamic pressure, $\dfrac{\rho_o U_o^2}{2}$
$\bar{r}$	$\dfrac{\beta R}{L_o}$
$\bar{r}_e$	see equation (46)
R	radius of body
S	area of wing plan form
$S_w(x,\theta)$	normal projection of wing cross-sectional area measured in oblique planes
t	maximum thickness of wing root chord
U_o	speed of free stream
V	volume
x,y,z	Cartesian coordinate system, x parallel to free-stream direction
x,r,θ	cylindrical coordinate system, x parallel to free-stream direction

$\alpha_n(x)$	strength of nth-order optimum cancellation multipoles (See eq. (36).)
β	$\sqrt{M^2-1}$
λ_u	slope of wing upper surface, measured relative to free-stream direction
μ	$\tan^{-1}(\beta \cos \theta)$
ρ_o	free-stream density
φ	perturbation velocity potential

DEFINITION OF THE PROBLEM

The problem of designing an airplane to have a minimum wave drag must be stated quite precisely. If the aerodynamicist is approached with the question, "Given an aerodynamic shape, can its wave drag be lowered?" he can always reply that any volume of material having a wave drag can always be reshaped within a space of finite dimensions so that it will have less wave drag at a given Mach number. Such an answer is interesting but, at present, not very useful to the airplane designer. There is first, of course, the basic criterion that the total drag should be minimized at a given lift and minimizing a component part of this total without holding the other parts fixed does not necessarily yield the lowest possible drag for a given set of restraints. For example, the configuration illustrated in figure 2 has no wave
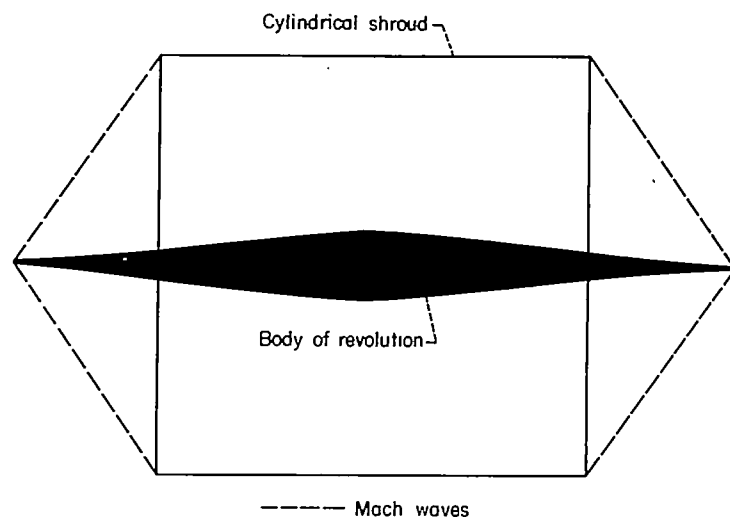

FIGURE 2.—Body and shroud with zero wave drag.

drag when traveling at zero angle of attack; but it has a relatively high friction drag, because of the large amount of wetted area, and its drag due to lift could also be relatively high. Completely aside from all such performance considerations, however, are many other important considerations that are unfortunately more or less vaguely defined from an aerodynamic point of view. For example, an airplane must contain a certain amount of usable volume, the shaping of individual parts is limited by structural requirements, and the arrangement of these parts must not seriously harm the airplane stability and control. The interrelation of all such separate demands presents an extremely complex design problem making it difficult to deviate too far from the reliable shapes set by experience.

As a result of the above-mentioned difficulties, the aerodynamicist who is concerned with discovering a practical

---

[3] From a mathematical point of view the essence of the method outlined above is that the analysis involves the solution to direct problems, that is, problems of integration. Calculating the drag of a given body, on the other hand, involves the solution to inverse problems, that is, problems involving the inversion of integral equations.

airplane shape having low wave drag finds the real definition of his problem somewhat obscure. In a sense his first problem is, literally, to pose a problem; that is, to impose a minimum number of arbitrary but pertinent restraints within the framework of which the wave drag is to be minimized. Even when this has been done, he still is concerned with the question of uniqueness, since optimum shapes are not necessarily unique even when several restraints are imposed. Consider, for example, the problem of finding the Busemann biplane which will have minimum wave drag at a given Mach number for a fixed section strength, volume, and wetted area. If the design Mach number is 1.41, one such design (on the basis of linearized theory) is shown in figure 3 where the chord-gap ratio, h/c, is equal to $\frac{1}{2}$. The resulting variation of the wave drag is shown in the upper part of figure 4. However, when the gap is closed to the point where h/c equals $\frac{1}{4}$, the variation of wave drag, shown in the lower part of figure 4, is the same within the interval $1.28 \leq M \leq 1.66$ and everywhere else is lower. It is likely that one would have first discovered the former solution, yet to the accuracy of the theory used, the latter is obviously preferable.

With the above observations always in mind, attention will be directed in this report to the analysis of simplified configurations composed of two distinct types of volume: planar types, that is, wing-like volumes, thin in one dimension and bounded by surfaces that never deviate far from a reference plane; and rectilinear types, that is, fuselage-like volumes longer in one dimension than in the other two and disposed more or less symmetrically about a straight line.

In particular the following problem is posed:

Given a thin nonlifting wing, what is the shape of an adjoining fuselage, the stream surface of which is simulated by a line of multipoles in the same plane as the wing, that will minimize the wave drag of the combination at a given Mach number?

BASIC CONCEPTS

A LINE OF SOURCES

The velocity potential induced at the point x,r,θ by a group of sources distributed along the x axis, starting at $-L_o$, is well known to be given by

$$\varphi(x,r,\theta) = -\frac{1}{2\pi} \int_{-L_o}^{x-\beta r} \frac{a_o(\xi)d\xi}{\sqrt{(x-\xi)^2 - \beta^2 r^2}} \qquad (3)$$
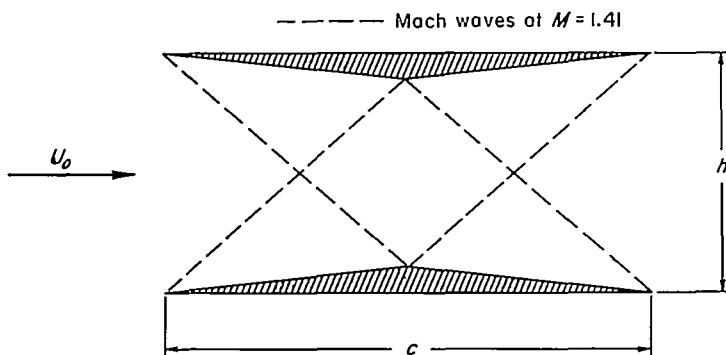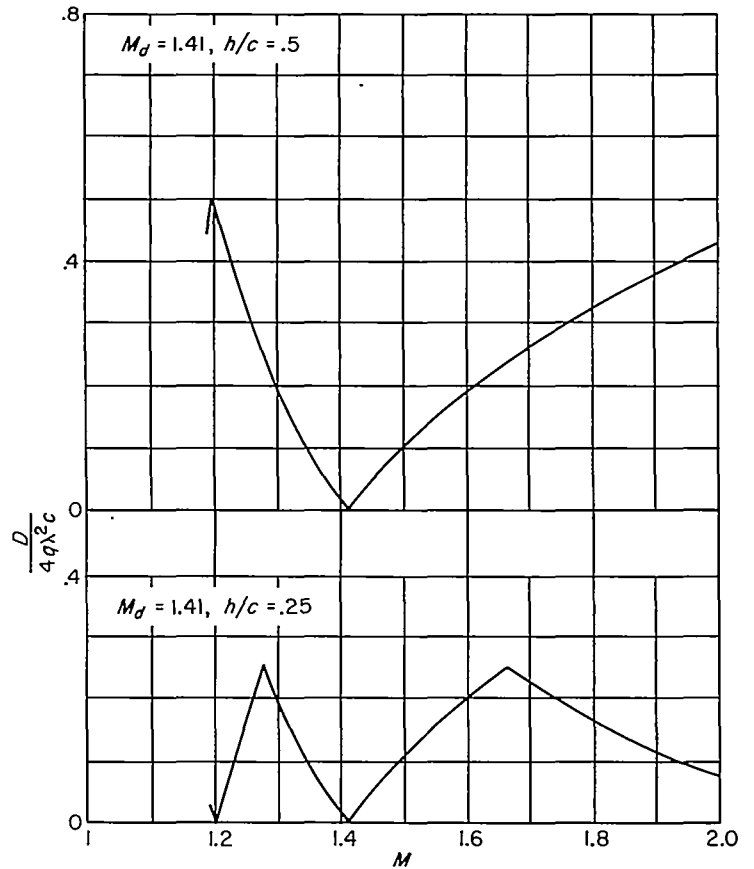
FIGURE 3.—Busemann biplane.

FIGURE 4.—Drag variation for double-wedge Busemann biplanes.

where $a_o(\xi)$ is the source strength per unit of length. In order to calculate wave drag one needs only the value of φ as r approaches infinity. This asymptotic value is simple enough to find provided it is observed that, as r is increased, x should also be increased so the potential can be studied in the vicinity of the Mach waves radiating from the disturbing object. Hence, set

$$x = x_o + \beta r \qquad (4)$$

so for a given r, x_o measures the streamwise distance of the point x,r,θ from the Mach wave emanating from the origin and, in particular, the foremost wave is located at $x_o = -L_o$. (See figure 5.)
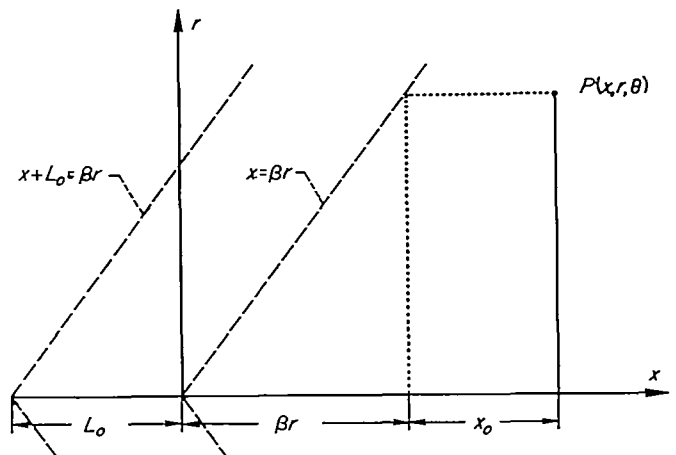
FIGURE 5.—Coordinates introduced in equations (4) and (5).

If equation (4) is placed into equation (3) and r is assumed to be large, the potential induced by a source is

$$\varphi)_{r \to \infty} = -\frac{1}{2\pi\sqrt{2\beta r}} \int_{-L_o}^{x_o} \frac{a_o(\xi) d\xi}{\sqrt{x_o - \xi}} \quad (5)$$

and the induced velocities are

$$\varphi_x)_{r \to \infty} = -\frac{1}{2\pi\sqrt{2\beta r}} \int_{-L_o}^{x_o} \frac{a_o'(\xi) d\xi}{\sqrt{x_o - \xi}} \quad (6a)$$

$$\varphi_r)_{r \to \infty} = -\beta\varphi_x \quad (6b)$$

MULTIPOLES

Lamb, in reference 2, page 527, has presented a general solution to equation (1) consisting of an infinite set of basic singular solutions. These basic singularities, referred to as multipoles, can be distributed along a line and weighted so as to reproduce certain body shapes enclosing the line. The expression for the perturbation velocity potential for a distribution of nth-order $(n=0,1,2,\dots)$ multipoles starting at $-L_o$ and continuing along the x axis can be written in terms of a cylindrical coordinate system (fig. 1) as

$$\varphi_n(x,r,\theta) = -\frac{r^n}{2\pi}\left(\frac{1}{r}\frac{\partial}{\partial r}\right)^n \int_{-L_o}^{x-\beta r} \frac{[a_n(\xi)\cos n\theta + b_n(\xi)\sin n\theta]d\xi}{\sqrt{(x-\xi)^2 - \beta^2 r^2}} \quad (7)$$

The operator $\left(\dfrac{1}{r}\dfrac{\partial}{\partial r}\right)^2$ is defined as

$$\left(\frac{1}{r}\frac{\partial}{\partial r}\right)^2 = \frac{1}{r}\frac{\partial}{\partial r}\left(\frac{1}{r}\frac{\partial}{\partial r}\right) = -\frac{1}{r^3}\frac{\partial}{\partial r} + \frac{1}{r^2}\frac{\partial^2}{\partial r^2}$$

and the definition of $\left(\dfrac{1}{r}\dfrac{\partial}{\partial r}\right)^n$ follows by induction. If the notation[4]

$$\left(\frac{\partial}{\partial x}\right)^n \int_a^x \frac{A(y)dy}{\sqrt{x-y}} = (-1)^n \frac{(1)(3)\dots(2n-1)}{2^n} \int_a^x \frac{A(y)dy}{(x-y)^{(2n+1)/2}}$$

is introduced, where the symbol $\displaystyle\int\!\!\!\!\!-$ is read "finite part of the integral," equation (7) becomes

$$\varphi_n(x,r,\theta) = -\frac{r^n \beta^{2n}(2n)!}{2^{n+1}\pi(n)!} \int_{-L_o}^{x-\beta r} \frac{[a_n(\xi)\cos n\theta + b_n(\xi)\sin n\theta]d\xi}{[(x-\xi)^2 - \beta^2 r^2]^{(2n+1)/2}} \quad (8)$$

and the general expressions for the induced velocities become—writing only the term involving the cosine, since the result for the sine is directly analogous

$$\varphi_x(x,r,\theta) = \sum_{n=0}^{\infty} \frac{r^n \beta^{2n}(2n+2)!}{2^{2n+2}\pi(n+1)!} \int_{-L_0}^{x+\beta r} \frac{(x-\xi)a_n(\xi)\cos n\theta \, d\theta}{[(x-\xi)^2 - \beta^2 r^2]^{(2n+3)/2}} \quad (9a)$$

$$\varphi_r(x,r,\theta) = -\sum_{n=0}^{\infty} \frac{\beta^{2n} r^{n-1}(2n)!}{2^{n+1}\pi(n)!} \int_{-L_0}^{x-\beta r}$$

$$\frac{[n(x-\xi)^2 + (n+1)\beta^2 r^2]a_n(\xi)\cos n\theta \, d\xi}{[(x-\xi)^2 - \beta^2 r^2]^{(2n+3)/2}} \quad (9b)$$

$$\frac{1}{r}\varphi_\theta(x,r,\theta) = \sum_{n=0}^{\infty} \frac{n r^{n-1}\beta^{2n}(2n)!}{2^{n+1}\pi(n)!} \int_{-L_0}^{x-\beta r} \frac{a_n(\xi)\sin n\theta \, d\xi}{[(x-\xi)^2 - \beta^2 r^2]^{(2n+1)/2}} \quad (9c)$$

Another very useful way of developing these multipole solutions evolves from an application of operational tech-

[4] For a detailed discussion of the finite-part concept as used in this report see reference 3.

niques. To begin with, rewrite equation (1) in terms of a polar coordinate system, thus

$$\beta^2 \frac{\partial^2 \varphi}{\partial x^2} - \frac{\partial^2 \varphi}{\partial r^2} - \frac{1}{r}\frac{\partial \varphi}{\partial r} - \frac{1}{r^2}\frac{\partial^2 \varphi}{\partial \theta^2} = 0 \quad (10)$$

Next, define the Laplace transform of $\varphi(x,r,\theta)$ by

$$\bar{\varphi}(s,r,\theta) = \int_0^{\infty} \varphi(x,r,\theta)e^{-xs}dx \quad (11)$$

and apply this transform to equation (10). There results (for a proof see Appendix A).

$$\beta^2 s^2 \bar{\varphi} - \frac{\partial^2 \bar{\varphi}}{\partial r^2} - \frac{1}{r}\frac{\partial \bar{\varphi}}{\partial r} - \frac{1}{r^2}\frac{\partial^2 \bar{\varphi}}{\partial \theta^2} = 0 \quad (12)$$

Now, if a general solution to equation (12) is expressed in the form

$$\bar{\varphi}(s,r,\theta) = f(r)\cos n\theta$$

then $f(r)$ must satisfy the equation

$$\frac{d^2 f}{dr^2} + \frac{1}{r}\frac{df}{dr} - \left(\frac{n^2}{r^2} + \beta^2 s^2\right)f = 0$$

Solutions to this are given by

$$f(r) = \overline{C}_n(s)I_n(\beta r s) + \overline{A}_n(s)K_n(\beta r s)$$

where I_n and K_n are modified Bessel functions as defined in reference 4, page 77. Hence, if $\bar{\varphi}$ is to vanish as r goes to infinity, a general solution to equation (10) can be written in the form

$$\bar{\varphi}(s,r,\theta) = \frac{-1}{2\pi}\sum_0^{\infty}[\overline{A}_n(s)\cos n\theta + \overline{B}_n(s)\sin n\theta]K_n(\beta r s) \quad (13)$$

The above result will be transformed back to the physical plane in two ways. First, apply the identity (ref. 4, p. 79)

$$K_n(z) = (-1)^n \left(\frac{1}{z}\frac{d}{dz}\right)^n K_0(z)$$

and re-express equation (13) as (only the coefficient of the $\cos n\theta$ term is written since the treatment of the sine term is identical)

$$\bar{\varphi}(s,r,\theta) = -\frac{1}{2\pi}\sum_0^{\infty}(-1)^n \cos n\theta \frac{\overline{A}_n(s)}{\beta^n s^n} r^n \left(\frac{1}{r}\frac{d}{dr}\right)^n K_0(\beta r s)$$

The inverse Laplace transform of $K_0(\beta r s)$—see reference 5—is

$$L^{-1}[K_0(\beta r s)] = \begin{cases} 0, & x < \beta r \\ \dfrac{1}{\sqrt{x^2 - \beta^2 r^2}}, & x > \beta r \end{cases}$$

So, since

$$\int_{-L_o}^{x} dx_1 \int_{-L_o}^{x_1} dx_2 \dots \int_{-L_0}^{x_{n-1}} dx_n A_n(x_n) =$$

$$\frac{1}{(n-1)!}\int_{-L_0}^{x}(x-x_1)^{n-1}A_n(x_1)dx_1 \quad (14)$$

an application of the convolution integral and other standard operational techniques yields

$$\varphi(x,r,\theta)=-\frac{1}{2\pi}\left\{\int_{-L_o}^{x-\beta r}\frac{A_o(\xi)d\xi}{\sqrt{(x-\xi)^2-\beta^2 r^2}}+\right.$$

$$\left.\sum_1^\infty r^n\left(\frac{1}{r}\frac{d}{dr}\right)^n\int_{-L_o}^{x-\beta r}\frac{\left[\frac{(-1)^n}{\beta^n(n-1)!}\int_{-L_o}^{\xi}(\xi-x_1)^{n-1}A_n(x_1)dx_1\right]}{\sqrt{(x-\xi)^2-\beta^2 r^2}}d\xi\right\}$$

$$\tag{15}$$

From comparison of equations (8) and (15), the relation between the strengths $a_n(x)$ and $A_n(x)$ for the two different forms of the solution is found to be

$$\left.\begin{array}{ll}a_o(x)=A_o(x) & , \quad n=0\\[2mm](-\beta)^n a_n(x)=\frac{1}{(n-1)!}\int_{-L_o}^{x}(x-x_1)^{n-1}A_n(x_1)dx_1, & n>0\end{array}\right\}\tag{16a}$$

or

$$(-\beta)^n a_n^{(n)}(x)=A_n(x)\tag{16b}$$

where $a_n^{(n)}(x)$ symbolizes the operation $\frac{d^n}{dx^n}a_n(x)$ and where use is made of the conditions

$$a_n^{(n)}(-L_o)=a_n^{(n-1)}(-L_o)=\ .\ .\ .\ =a_n(-L_o)=0\tag{17}$$

Another way to transform equation (13) back to the physical plane is to do so directly. In this way one finds (from ref. 5)

$$\varphi_r(x,r,\theta)=\frac{1}{\pi}\left(\int_{-L_o}^{x-\beta r}\frac{(x-\xi)A_o{}'(\xi)d\xi}{r\sqrt{(x-\xi)^2-\beta^2 r^2}}+\frac{\beta}{2}\sum_1^\infty\cos n\theta\int_{-L_o}^{x-\beta r}\frac{A_n{}'(\xi)\left\{\frac{x-\xi}{\beta r}\cosh\left[n\cosh^{-1}\left(\frac{x-\xi}{\beta r}\right)\right]\right\}d\xi}{\sqrt{(x-\xi)^2-\beta^2 r^2}}\right)$$

$$\tag{19c}$$

If the relation between the functions $a_n(x)$ and $A_n(x)$ is given by equation (16), the velocities represented by equations (9) and (19) are, of course, identical.

In order to obtain limiting values induced by multipoles distributed along the x axis starting at $-L_o$, one returns to either equation (8) or (18) and calculates the leading term in a $1/r$ expansion. As in the derivation of equation (5), it is necessary to observe that as r is increased, x should also be increased so φ is given in the vicinity of the foremost Mach cone created by the multipole distributions. Hence, using equation (4), one finds for equation (18)

$$\varphi=-\frac{1}{2\pi}\sum_0^\infty\cos n\theta\int_{-L_o}^{x_o}\frac{A_n(\xi)\cosh\left[n\cosh^{-1}\left(1+\frac{x_o-\xi}{\beta r}\right)\right]d\xi}{\sqrt{2\beta r(x_o-\xi)\left(1+\frac{x_o-\xi}{2\beta r}\right)}}$$

which has the leading term as r goes to infinity

$$\varphi)_{r\to\infty}=-\frac{1}{2\pi\sqrt{2\beta r}}\sum_0^\infty\cos n\theta\int_{-L_o}^{x_o}\frac{A_n(\xi)d\xi}{\sqrt{x_o-\xi}}\tag{20}$$

Similarly, the perturbation velocities reduce to

$$L^{-1}K_n(\beta r s)=\left\{\begin{array}{ll}0 & , \quad x<\beta r\\[4mm]\dfrac{\cosh\left[n\cosh^{-1}\left(\dfrac{x}{\beta r}\right)\right]}{\sqrt{x^2-\beta^2 r^2}}, & x>\beta r\end{array}\right.$$

from which equation (13) reduces immediately to

$$\varphi(x,r,\theta)=-\frac{1}{2\pi}\sum_{n=0}^\infty\cos n\theta\int_{-L_0}^{x-\beta r}\frac{A_n(\xi)\cosh\left[n\cosh^{-1}\left(\frac{x-\xi}{\beta r}\right)\right]}{\sqrt{(x-\xi)^2-\beta^2 r^2}}d\xi\tag{18}$$

The perturbation velocities in the field represented by this potential are readily calculated. Thus

$$\varphi_x(x,r,\theta)=-\frac{1}{2\pi}\sum_{n=0}^\infty\cos n\theta\int_{-L_0}^{x-\beta r}\frac{A_n{}'(\xi)\cosh\left[n\cosh^{-1}\left(\frac{x-\xi}{\beta r}\right)\right]}{\sqrt{(x-\xi)^2-\beta^2 r^2}}d\xi\tag{19a}$$

$$\frac{1}{r}\varphi_\theta(x,r,\theta)=\frac{1}{2\pi r}\sum_0^\infty n\sin n\theta\int_{-L_0}^{x-\beta r}\frac{A_n(\xi)\cosh\left[n\cosh^{-1}\left(\frac{x-\xi}{\beta r}\right)\right]}{\sqrt{(x-\xi)^2-\beta^2 r^2}}d\xi\tag{19b}$$

and by taking the derivative of equation (13) with respect to r, one finds

$$\overline{\varphi}_r=\frac{1}{2\pi}\left\{\beta s\overline{A}_o(s)K_1(\beta rs)+\frac{1}{2}\sum_1^\infty\beta s\overline{A}_n(s)[K_{n-1}(\beta rs)+K_{n+1}(\beta rs)]\right\}$$

which transforms to

$$\varphi_x)_{r\to\infty}=-\frac{1}{2\pi\sqrt{2\beta r}}\sum_0^\infty\cos n\theta\int_{-L_o}^{x_o}\frac{A_n{}'(\xi)d\xi}{\sqrt{x_o-\xi}}\tag{21a}$$

$$\varphi_r)_{r\to\infty}=-\beta\varphi_x\tag{21b}$$

$$\frac{1}{r}\varphi_\theta\Big)_{r\to\infty}=\frac{1}{2\pi\sqrt{2\beta r}}\sum_0^\infty n\sin n\theta\int_{-L_o}^{x_o}\frac{A_n(\xi)d\xi}{\sqrt{x_o-\xi}}\tag{21c}$$

In calculating the wave drag using equation (2) only the velocity components $\varphi_x)_{r\to\infty}$ and $\varphi_r)_{r\to\infty}$ are necessary. Hence, from comparison of equations (21a) and (21b) with (6a) and (6b), it follows that at a given θ a series of multipoles induce the same momentum flux on an infinite cylindrical control surface as a line of sources having a strength variation $a_o(x)$ equal to $\sum_0^\infty\cos n\theta A_n{}'(\xi)$. If one identifies a line of sources with a body of revolution, then it is apparent that, at a given θ, a dragwise equivalence has been established between a line of multipoles and a body of revolution.

HAYES' THEOREM AND ITS APPLICATION

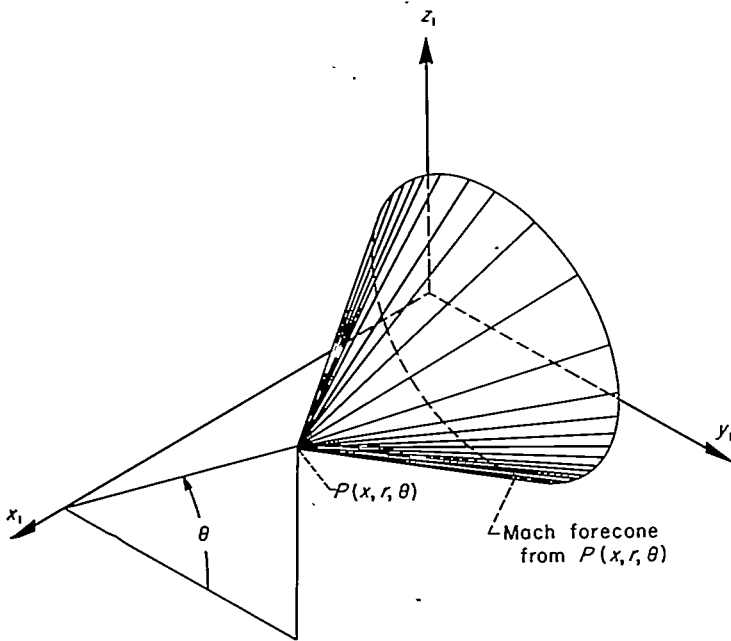In the previous section a relation was found between multipole and source strengths which produce, at a fixed θ,

FIGURE 6.—Mach forecone from x,r,θ in x_1,y_1,z_1 space.

equivalent momentum transport across a cylinder of infinite radius. By using a theorem attributable to Hayes (ref. 6) one can derive the strength relationship between any distribution of singularities throughout space and a line of sources which gives the same equivalence.

The essence of Hayes' theorem is that, for a fixed θ, the velocities induced on a cylinder of infinite radius by singular solutions to equation (1) (e. g., sources and doublets) are invariant to displacements of the singularities along certain oblique planes. In order to be specific, the equation of these oblique planes is next derived.

Consider the point x,r,θ in a flow field having a supersonic free stream moving parallel to the x axis. Figure 6 shows the Mach forecone (by definition the Mach forecone is the boundary of the region within which a disturbance in a supersonic stream can affect the flow at the cone apex) from x,r,θ in x_1,y_1,z_1 space. The equation of the forecone is

$$x_1=x-\beta\sqrt{(r\cos\theta-y_1)^2+(r\sin\theta-z_1)^2} \qquad (22)$$

One wishes to let r become very large and find the shape of the forecone as it passes through regions close to the origin of the x_1,y_1,z_1 coordinate system, regions in which the objects creating the wave drag are located. From equation (4) and the expansion of equation (22) for large r, it follows that

$$x_1=x_0+\beta r-\beta r\left[1-\frac{2}{r}(y_1\cos\theta+z_1\sin\theta)+\frac{y_1{}^2+z_1{}^2}{r^2}\right]^{1/2}$$

$$=x_0+\beta(y_1\cos\theta+z_1\sin\theta)-\frac{\beta}{2r}(y_1\sin\theta-z_1\cos\theta)^2+\ldots$$

and when r goes to infinity

$$x_1=x_0+\beta y_1\cos\theta+\beta z_1\sin\theta \qquad (23)$$

which is the equation of the oblique plane mentioned above. It should be noted that the envelope formed from these planes by fixing x_o and varying θ between 0 and 2π coincides

with the Mach forecone and aftercone from the point $x_o,0,0$. Hayes' result can now be stated [5]

To the lowest order in $1/r$, as r tends to infinity, the magnitude of the perturbation velocity potential and its gradients at a fixed angle θ is invariant to a finite translation of sources (or any other singular solution to the wave equation) on planes parallel to that given by equation (23).

Consider the application of Hayes' theorem to planar distributions of sources lying in the $z_1=0$ plane. As is well known, such a distribution simulates a wing symmetrically disposed about the horizontal ($z_1=0$) plane. In fact, if $\lambda_u(x_1,y_1)$ is the local slope of the wing upper surface, the local source strength per unit area (according to thin airfoil theory) required to simulate the wing is $-U_o\lambda_u/\pi$ and the velocity potential of the disturbed flow field is given by

$$\varphi(x,y,z)=-\frac{U_o}{\pi}\int\int_\tau\frac{\lambda_u(x_1,y_1)\,dx_1\,dy_1}{\sqrt{(x-x_1)^2-\beta^2(y-y_1)^2-\beta^2z^2}} \qquad (24)$$

where τ is the area of integration bounded by the wing edge and the trace in the $z_1=0$ plane of the Mach forecone from the point x, y, z. Next introduce the new coordinates ξ_1 and η_1 such that ξ_1 lies along the x_1 axis and η_1 lies along the intersection of the $z_1=0$ plane and the plane given by equation (23) (see fig. 7). Set

$$\tan\mu=\beta\cos\theta \qquad (25)$$

and

$$\left.\begin{array}{l}\xi_1=x_1-y_1\tan\mu\\[4pt]\eta_1=y_1\sec\mu\\[4pt]x_1=\xi_1+\eta_1\sin\mu\\[4pt]y_1=\eta_1\cos\mu\end{array}\right\} \qquad (26)$$

Then, in terms of the ξ_1,η_1 system, equation (24) becomes

$$\varphi(x,y,z)=-\frac{U_o}{\pi}\int\int_\tau\frac{\lambda_u(\xi_1+\eta_1\sin\mu,\eta_1\cos\mu)\cos\mu\,d\xi_1\,d\eta_1}{\sqrt{(x-\xi_1-\eta_1\sin\mu)^2-\beta^2(y-\eta_1\cos\mu)^2-\beta^2z^2}}$$
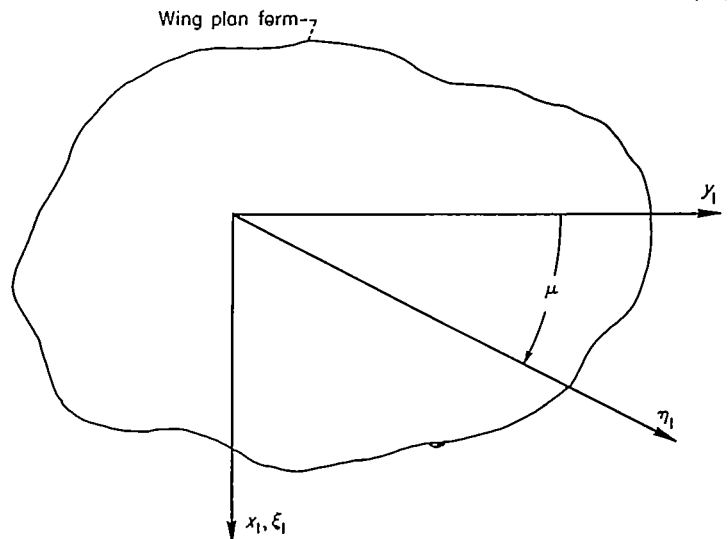
$$(27)$$

FIGURE 7.—Orientation of x_1,y_1 and ξ_1,η_1 coordinates.

[5] For proofs, see Hayes' original derivation (ref. 6) or, if more convenient, reference 1.

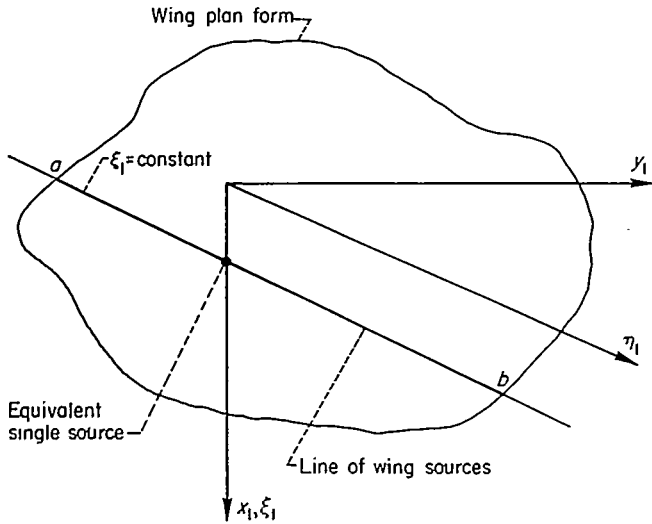FIGURE 8.—Position of wing sources and equivalent single source.

As before, the asymptotic value of φ as $r=\sqrt{y^2+z^2}\to\infty$ is to be calculated. Accordingly, one can apply Hayes' theorem and sum up all the sources along a line $\xi_1=$constant (e. g., between a and b in fig. 8) and place them as a single source on the axis. The strength of this equivalent single source is given by

$$U_oS_w'(\xi_1,\theta)=2U_o\cos\mu\int_{wing}\lambda_w(\xi_1+\eta_1\sin\mu,\eta_1\cos\mu)\,d\eta_1 \quad (28)$$

where the integration is taken across the complete wing along the line $\xi_1=$constant and $S_w'(\xi_1,\theta)=\dfrac{\partial}{\partial\xi_1}S_w(\xi_1,\theta)$.

The term $S_w(x,\theta)$ has a clear geometrical interpretation (see fig. 9), being simply the normal projection of the wing area intercepted by the oblique plane[6] $x_1=x+\beta y_1\cos\theta$.

The above defines the strength variation of a line of sources (and, therefore, a body of revolution) which induces, for large r and a fixed θ, a potential field identical to that

$S_W(x,\theta)$ =Normal projection of wing area along AA
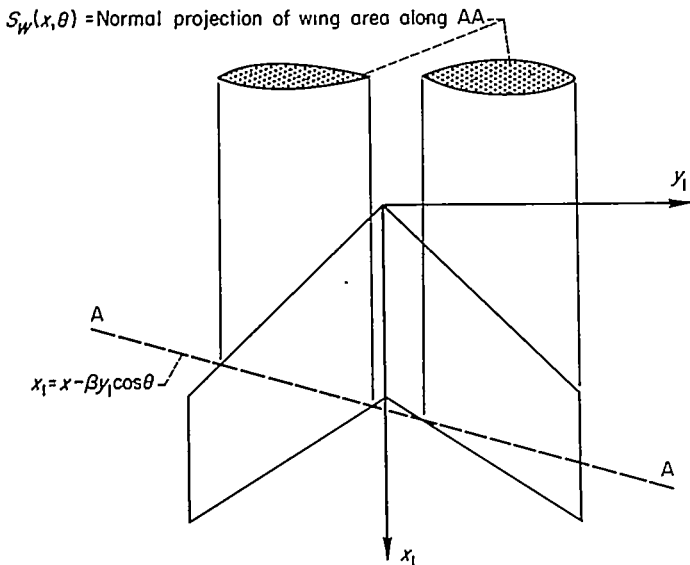
FIGURE 9.—Wing area intercepted by oblique plane.

[6] The true oblique plane is given by equation (23) but the wing is so close to the $z_1=0$ plane that the variation with z_1 can be neglected.

induced by a given wing. Hence, the results given in equation (6) yield

$$(\varphi_x)_{r\to\infty}=-\frac{U_o}{2\pi\sqrt{2\beta r}}\int_{-L(\theta)}^{x_o}\frac{S_w''(\xi_1,\theta)\,d\xi_1}{\sqrt{x_o-\xi_1}} \quad (29a)$$

$$(\varphi_r)_{r\to\infty}=-\beta\varphi_x \quad (29b)$$

A similar result exists for a planar doublet distribution (see ref. 1 or 6) but, in this report, only problems in which the wings have no loading (local lift) will be considered. Lifting effects have been treated in a similar fashion in reference 7.

CANCELLATION MULTIPOLES AND DRAG MINIMIZATION

Since the flow field is governed by a linear partial differential equation the velocities induced by different solutions to it are additive. Therefore, the drag of an object simulated by various multipoles distributed along the x_1 axis and a sheet of sources in the $z_1=0$ plane is given by

$$D=-\rho_o\int_0^{2\pi}d\theta\int_{-\infty}^{\infty}dx\left\{\lim_{r\to\infty}r\left[(\varphi_r)_m+(\varphi_r)_w\right]\left[(\varphi_x)_m+(\varphi_x)_w\right]\right\}$$

where the subscripts m and w refer to the multipoles and wing sources, respectively. But equations (21) and (29) identify, for a fixed θ, these velocities with those induced by equivalent line sources. Hence, for any given θ; one can immediately apply Kármán's drag formula (ref. 8) and then for the total drag, integrate θ from 0 to 2π. This leads to

$$D=-\frac{\rho_o}{8\pi^2}\int_0^{2\pi}d\theta\int_{-L'(\theta)}^{L(\theta)}dx_1\int_{-L'(\theta)}^{L(\theta)}dx_2$$

$$\left\{U_oS_w''(x_1,\theta)+\sum_0^{\infty}(-\beta)^n[a_n^{(n+1)}(x_1)\cos n\theta+b_n^{(n+1)}(x_1)\sin n\theta]\right\}$$

$$\left\{U_oS_w''(x_2,\theta)+\sum_0^{\infty}(-\beta)^n[a_n^{(n+1)}(x_2)\cos n\theta+\right.$$

$$\left.b_n^{(n+1)}(x_2)\sin n\theta]\right\}1n|x_1-x_2|$$

However, since both the wing and multipoles are in the same plane (interpreted physically, the wing is centrally mounted on the fuselage) and the wing is simulated by sources only (has no twist or camber), one can show the optimum value of each $b_n^{(n+1)}(x_1)$ is identically zero.[7] Hence, one can write

$$D=-\frac{\rho_o}{8\pi^2}\int_0^{2\pi}d\theta\int_{-L'(\theta)}^{L(\theta)}dx_1\int_{-L'(\theta)}^{L(\theta)}dx_2\left[U_oS_w''(x_1,\theta)+\right.$$

$$\sum_0^{\infty}(-\beta)^na_n^{(n+1)}(x_1)\cos n\theta\right]$$

$$\left[U_oS_w''(x_2,\theta)+\sum_0^{\infty}(-\beta)^na_n^{(n+1)}(x_2)\cos n\theta\right]1n|x_1-x_2| \quad (30)$$

[7] By symmetry

$$S_w''(x,\theta)=S_w''(x,2\pi-\theta)$$

Hence

$$\int_0^{2\pi}\sin n\theta S_w''(x,\theta)d\theta=0$$

and any positive or negative variation of $b_n^{(n+1)}(x_1)$ can only increase the drag.

Next expand the term $S_w''(x,\theta)$ in a Fourier series. One finds

$$U_o S_w''(x,\theta)=\sum_0^\infty (-\beta)^n \alpha_n^{(n+1)}(x) \cos n\theta \qquad (31)$$

where

$$\alpha_o(x)=\frac{U_o}{2\pi}\int_0^{2\pi} S_w'(x,\theta)d\theta \qquad (32)$$

$$\alpha_n^{(n)}(x)=\frac{U_o}{\pi(-\beta)^n}\int_0^{2\pi} S_w'(x,\theta)\cos n\theta\, d\theta \qquad (33)$$

Place these expressions in equation (30), integrate with respect to θ—using the orthogonal property of the trigonometric series—and one finds

$$D=2D_o+\sum_1^\infty D_n \qquad (34)$$

where

$$\frac{D_n}{q}=-\frac{\beta^{2n}}{4\pi U_o{}^2}\int_{-L_o}^{L_o} dx_1 \int_{-L_o}^{L_o} dx_2 \, [\alpha_n^{(n+1)}(x_1)+a_n^{(n+1)}(x_1)]$$

$$[\alpha_n^{(n+1)}(x_2)+a_n^{(n+1)}(x_2)]1n|x_1-x_2| \qquad (35).$$

Since one can show[8]

$$I=-\int_{-L_o}^{L_o} dx_1 \int_{-L_o}^{L_o} dx_2 f'(x_1)f'(x_2)1n|x_1-x_2| \geq 0$$

the minimum value of D as expressed by equation (34) is given when each D_n is itself a minimum. In other words, each D_n can be minimized separately. Further, it follows that the value of the minimum itself is zero and occurs when

$$a_n^{(n+1)}(x)=-\alpha_n^{(n+1)}(x)$$

$$=\begin{cases} -\dfrac{U_o}{2\pi}\displaystyle\int_0^{2\pi} S_w''(x,\theta)d\theta, & , \quad n=0 \\[2mm] -\dfrac{U_o}{\pi(-\beta)^n}\displaystyle\int_0^{2\pi} S_w''(x,\theta)\cos n\theta\, d\theta, & n>0 \end{cases} \qquad (36)$$

Equation (36) is the mathematical definition of the optimum cancellation multipoles; namely, those multipoles which are just equal in magnitude and opposite in sign to the wing equivalent multipoles—equivalent in the sense that they induce an identical momentum flux across a cylinder of infinite radius.

Obviously, if all the optimum cancellation multipoles were used, the wave drag of the combination would be zero. This result must, however, be properly interpreted with regard to the simulated shape. In order that the multipole lines can represent the distortion of a real fuselage, one must assume a cylindrical body exists upstream from the Mach cone $x+L_o=\beta r$ (the effects of the nose are being neglected). This body forms the initial boundary of the stream tube which represents the physical fuselage in the vicinity of the wing and multipole lines. Clearly, the area enclosed by this initial boundary can be small enough for the subsequent stream surface to cross itself and represent, therefore, a physically unreal body. Hence, the fact that the wave drag of the wing and multipole combination can

be reduced to zero is quite valid, but in the over-all picture not only have the inevitable nose and tail drags been neglected but also the shape simulated by the combination can be unrealistic.

SOME PROPERTIES OF THE CANCELLATION MULTIPOLES

Let us consider next some of the restrictions necessarily imposed on cancellation-multipole distributions and some of the particular properties of those given by equation (36). In the first place, if $a_n(x)$ is any multipole distribution that generates a potential field given by equation (8) or (15), it follows from equation (17) that the value of $a_n(x)$ and its first n derivatives should be everywhere continuous. Further, if $a_n(x)$ is a constant behind some point, say L_o (i. e., for $\infty>x>L_o$), the induced flow field would simulate expanding streamlines in the case $n=0$ or some form of vorticity in the case $n>0$; the former case is to be avoided since any simulated body is assumed to have a finite area at $x=\infty$, and the latter case is to be avoided if there are no resultant forces normal to the free stream.

One can show that all the above properties are satisfied by $\alpha_n(\xi)$, the optimum cancellation-multipole distribution as defined by equation (36). First, notice that $\alpha_n^{(n+1)}(\xi)$ must be zero everywhere outside the wing-enclosing Mach forecone and aftercone, that is, for $-\infty<\xi<-L_o'$ and $L_o<\xi<\infty$ (see fig. 10). (Any multipoles in these regions cannot combine with the wing equivalent multipoles and must, therefore, increase the drag.) Hence, one can set

$$\alpha_n^{(n)}(-L_o')=\alpha_n^{(n-1)}(-L_o')$$

$$=\ldots\ \alpha_n(-L_o')$$

$$=0$$
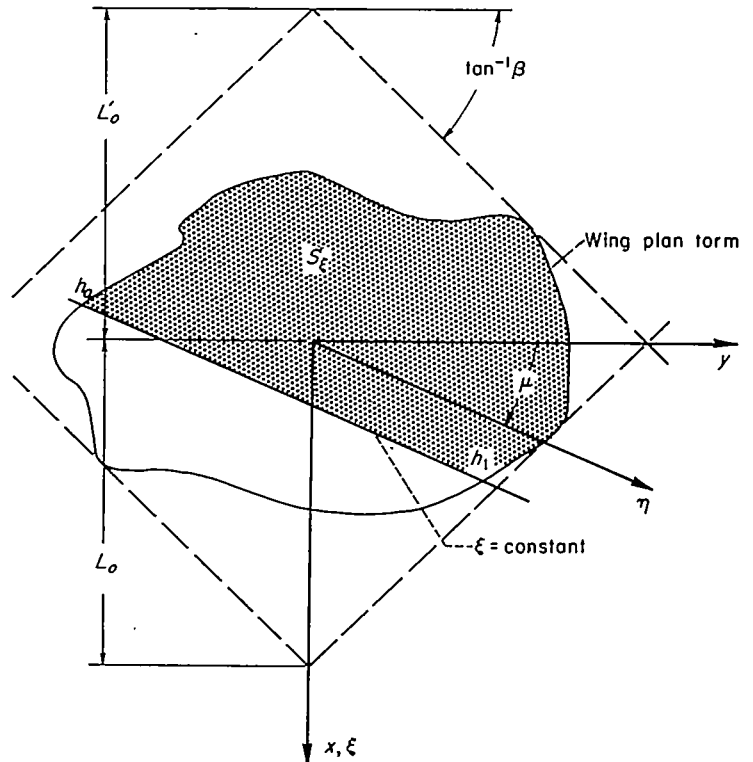
FIGURE 10.—Symbols used in study of multipole properties.

[8] Set $f(x)=\sum_1^\infty A_n \sin n\psi$, $x=-L_o \cos \psi$. Integration gives $I=\frac{\pi^2}{2}\sum_1^\infty nA_n{}^2$ which can never be negative.

Then the condition of continuity is automatically satisfied for $\alpha_n^{(m)}(\xi)$ in the entire interval $-\infty < x < \infty$ if $S_w'(\xi,\theta)$ is derived from a wing having finite wave drag (in particular, from a wing having no blunt edges along which the normal component of the free-stream Mach number is unity or greater). It follows immediately that $\alpha_n^{(m)}(\xi)$, $m < n$, is continuous since the latter is found by integrating (further smoothing) $\alpha_n^{(n)}(\xi)$.

The proof that $\alpha_n(L_o)$ as given by equation (36) is zero requires more consideration. One can show, however, that $\alpha_n^{(m)}(L_o) = 0$ where $0 \le m \le n$. First, the equality $\alpha_n^{(n)}(L_o) = 0$ follows from the fact that the wing closes and $S_w'(L_o,\theta)$ itself is zero. Next consider the definition of $\alpha_n^{(m)}(\xi)$. Thus

$$\alpha_n^{(m)}(\xi) = \frac{-U_o}{(-\beta)^n \pi} \int_0^{2\pi} S_w'(\xi,\theta) \cos n\theta \, d\theta$$

$$= \frac{-2U_o}{(-\beta)^n \pi} \int_0^{2\pi} \cos\mu \cos n\theta \, d\theta \int_{h_o(\theta,\xi)}^{h_1(\theta,\xi)} \lambda_u(\xi + \eta \sin\mu, \eta \cos\mu) \, d\eta$$

where use has been made of equation (28) for the definition of $S_w'(\xi,\theta)$ and h_o and h_1 are defined in figure 10. Since

$$\alpha_n^{(m)}(\xi) = \frac{1}{\Gamma(n-m)} \int_{-L_o'}^{\xi} (\xi-\xi_1)^{n-m-1} \alpha_n^{(n)}(\xi_1) \, d\xi_1 \quad (37)$$

one has

$$\alpha_n^{(m)}(\xi) = \frac{-2U_o}{(-\beta)^n \pi \Gamma(m-n)} \int_0^{2\pi} \cos n\theta \, d\theta$$

$$\int_{-L_o'}^{\xi} d\xi_1 \int_{h_o(\theta,\xi_1)}^{h_1(\theta,\xi_1)} d\eta (\xi-\xi_1)^{n-m-1} \lambda_u(\xi_1 + \eta \sin\mu, \eta \cos\mu) \cos\mu$$

Change the ξ_1, η coordinates back to the x,y system by means of equation (26) and this becomes

$$\alpha_n^{(m)}(\xi) = \frac{-2U_o}{(-\beta)^n \pi \Gamma(n-m)} \int_0^{2\pi} \cos n\theta \, d\theta \int_{S_\xi} \int (\xi - x + \beta y \cos\theta)^{n-m-1}$$

$$\lambda_u(x,y) \, dx \, dy$$

The area S_ξ, shown in figure 10, becomes independent of θ when $\xi = L_o$ (being then just the area of the wing itself), therefore

$$\alpha_n^{(m)}(L_o) = \frac{-2U_o}{(-\beta)^n \pi \Gamma(m-n)} \int \int_S \lambda_u(x,y) dx \, dy$$

$$\int_0^{2\pi} (L_o - x + \beta y \cos\theta)^{n-m-1} \cos n\theta \, d\theta = 0$$

since, for $m < n$

$$\int_0^{2\pi} \cos m\theta \cos n\theta \, d\theta = 0$$

Hence, for the $\alpha_n(\xi)$ defined by equation (36)

$$\alpha_n^{(n)}(L_o) = \alpha_n^{(n-1)}(L_o) = \alpha_n^{(n-2)}(L_o) = \ldots = \alpha_n(L_o) = 0 \quad (38)$$

AIRPLANE SHAPE

In the previous section a connection was established between multipole distributions and their resulting wave drag.

Further, this connection was direct and relatively simple if the strengths and positions of the distributions were given. Unfortunately the connection between the multipoles and the shape of the simulated surface is generally not so simple. Such a relation does certainly exist, however, and if the strengths of the multipoles are known, the relationship is again direct. That is, a given distribution of multipoles yields directly, by the formulas given in the previous section, the induced velocities everywhere in the flow field, these, in turn, fix the stream surfaces along any one of which (since, of course, the theory neglects viscosity) a physical surface can be imagined.

In general, if

$$\left. \begin{array}{c} F_c(x,y,z) = 0 \\ F_p(x,r,\theta) = 0 \end{array} \right\} \quad (39)$$

are the equations of a stream surface in cartesian and polar coordinates, respectively, then the equations

$$\left. \begin{array}{c} (U_o + \varphi_x)\dfrac{\partial F_c}{\partial x} + \varphi_y \dfrac{\partial F_c}{\partial y} + \varphi_z \dfrac{\partial F_c}{\partial z} = 0 \\ (U_o + \varphi_x)\dfrac{\partial F_p}{\partial x} + \varphi_r \dfrac{\partial F_p}{\partial r} + \dfrac{1}{r^2} \varphi_\theta \dfrac{\partial F_p}{\partial \theta} = 0 \end{array} \right\} \quad (40)$$

must hold.

For example, in studies of thin wings lying in a plane, the particular form of equation (39)

$$z - h(x,y) = 0$$

is assumed and equation (40) becomes

$$-(U_o + \varphi_x)\frac{\partial h}{\partial x} - \varphi_y \frac{\partial h}{\partial y} + \varphi_z = 0$$

or, neglecting second-order effects,

$$\frac{\partial h}{\partial x} = \frac{1}{U_o} \varphi_z$$

which is the familiar boundary condition used in thin-airfoil theory. On the other hand, if the equation of the body shape is written in the form

$$r - R(x,\theta) = 0$$

then equation (40) becomes, for linearized theory,

$$U_o \frac{\partial R}{\partial x} = \varphi_r - \frac{\varphi_\theta}{R^2} \frac{\partial R}{\partial \theta} \quad (41)$$

If the flow field is radially symmetrical or if the body surface is quasi-cylindrical, equation (41) reduces to

$$\frac{\partial R}{\partial x} = \frac{1}{U_o} \varphi_r \quad (42)$$

which is the familiar boundary condition used in the study of quasi-cylindrical bodies or bodies of revolution.

In general, a nonlinear partial differential equation of the first order such as equation (41) can be reduced to two simul-

taneous, ordinary, nonlinear differential equations of the first degree (see, e. g., ref. 9). Thus equation (41) becomes

$$\left.\begin{array}{l} \dfrac{d\theta}{dx}=\dfrac{1}{U_oR^2}\,\varphi_\theta(x,R,\theta) \\[2mm] \dfrac{dR}{dx}=\dfrac{1}{U_o}\,\varphi_r(x,R,\theta) \end{array}\right\} \qquad (43)$$

and if φ_θ and φ_r are known functions of x, R, and θ, these can be solved numerically.

If the strengths of all rectilinear multipoles and source sheets are given, equation (19) or (24) can be used to find φ_r and φ_θ at arbitrary field points. Hence, the first step in finding the body shapes reduces to that of integrating such equations. However, these integrations are difficult and tedious even when entirely numerical procedures are employed and the results still have to be interpreted in terms of the body shape according to equations (43). Therefore, from a practical viewpoint, it is necessary to study certain approximate methods for obtaining the velocity field.

Let attention be concentrated on the disturbances created by a line of multipoles. In particular, consider the fields
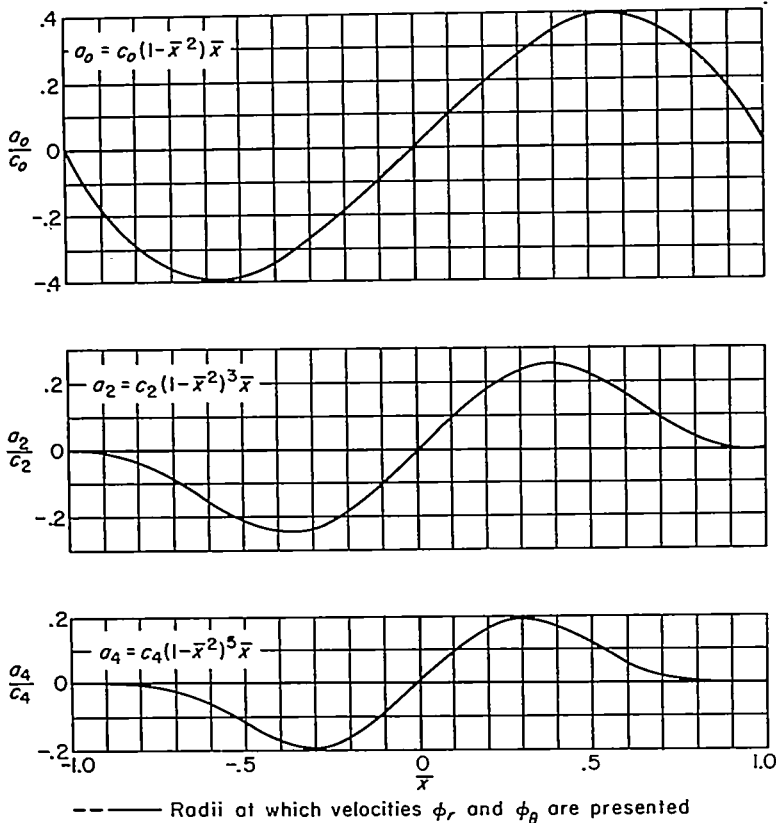

(a) Multipole distributions.

FIGURE 11.—Radial and tangential velocities induced by three different multipole distributions at four radii.
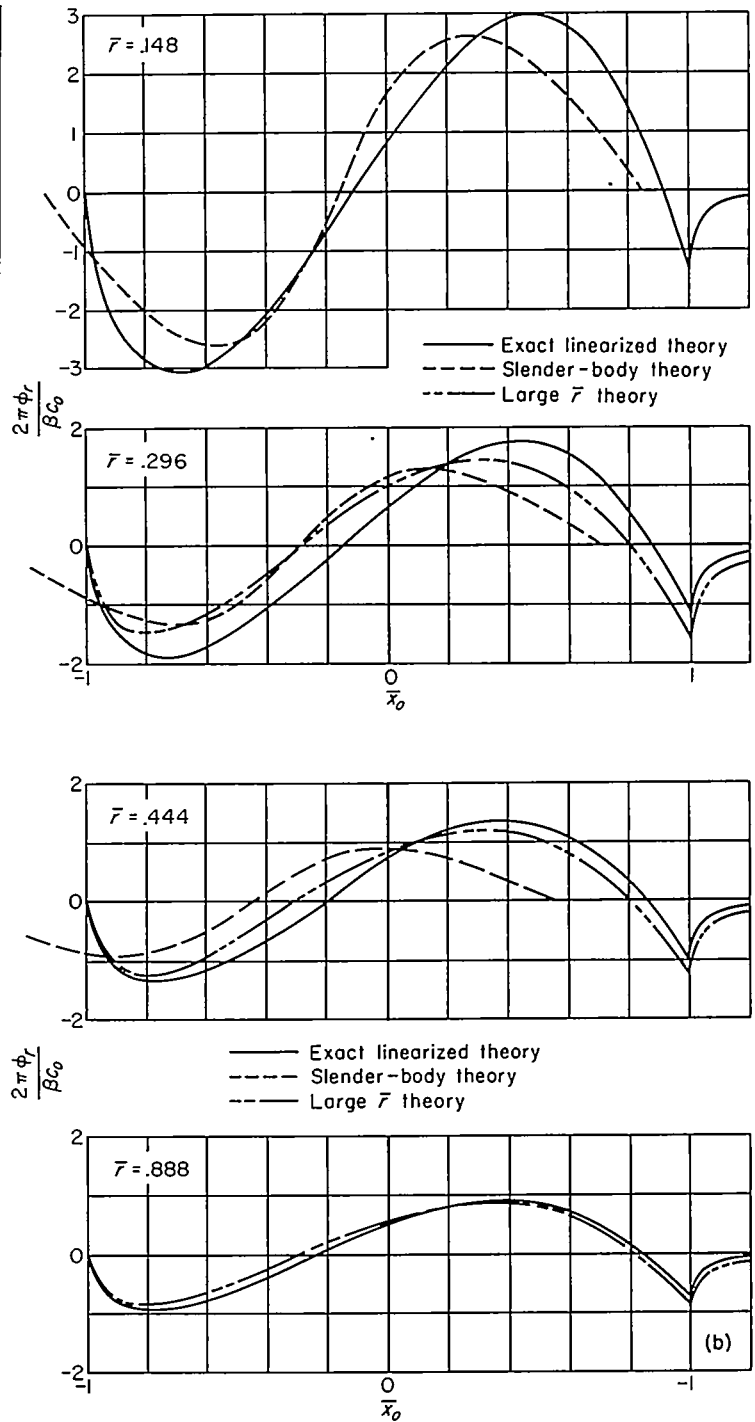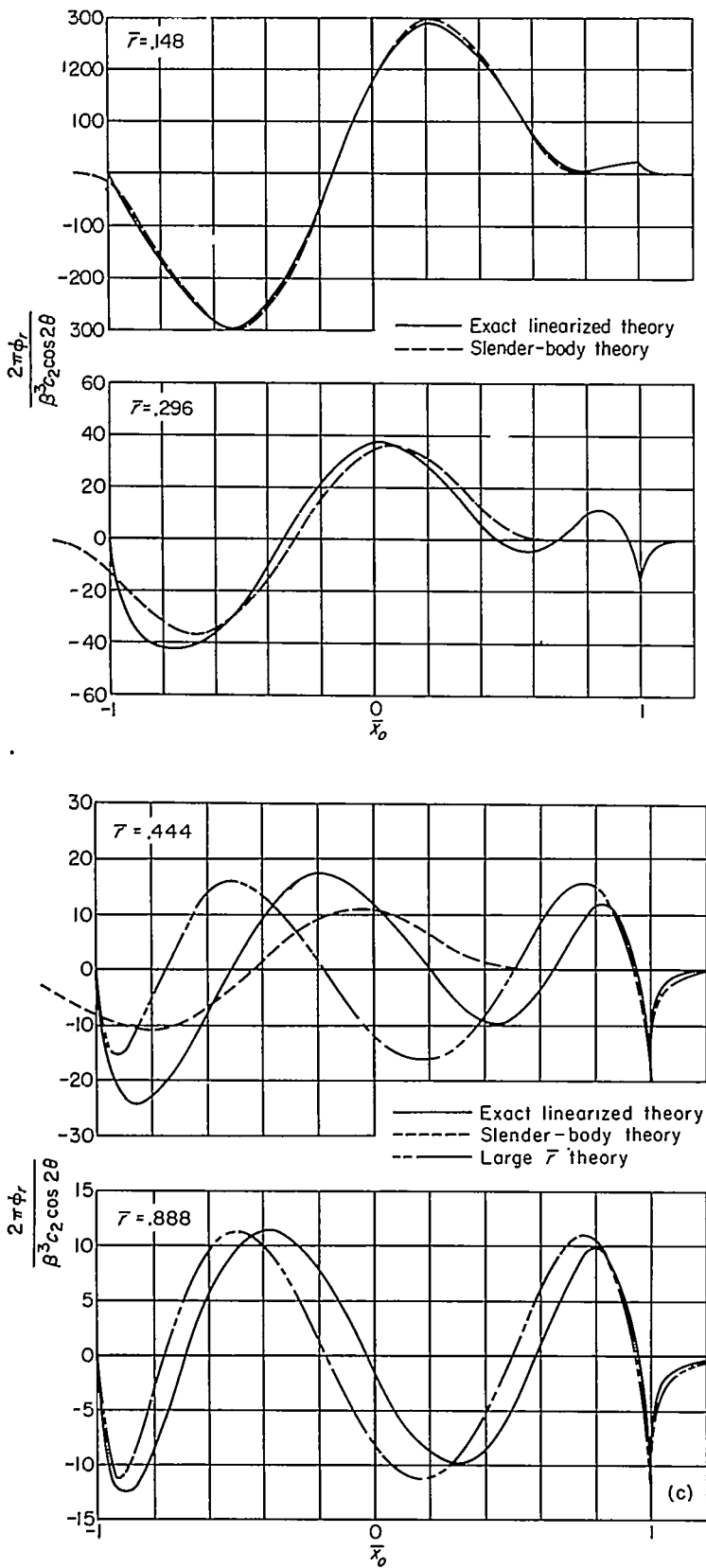

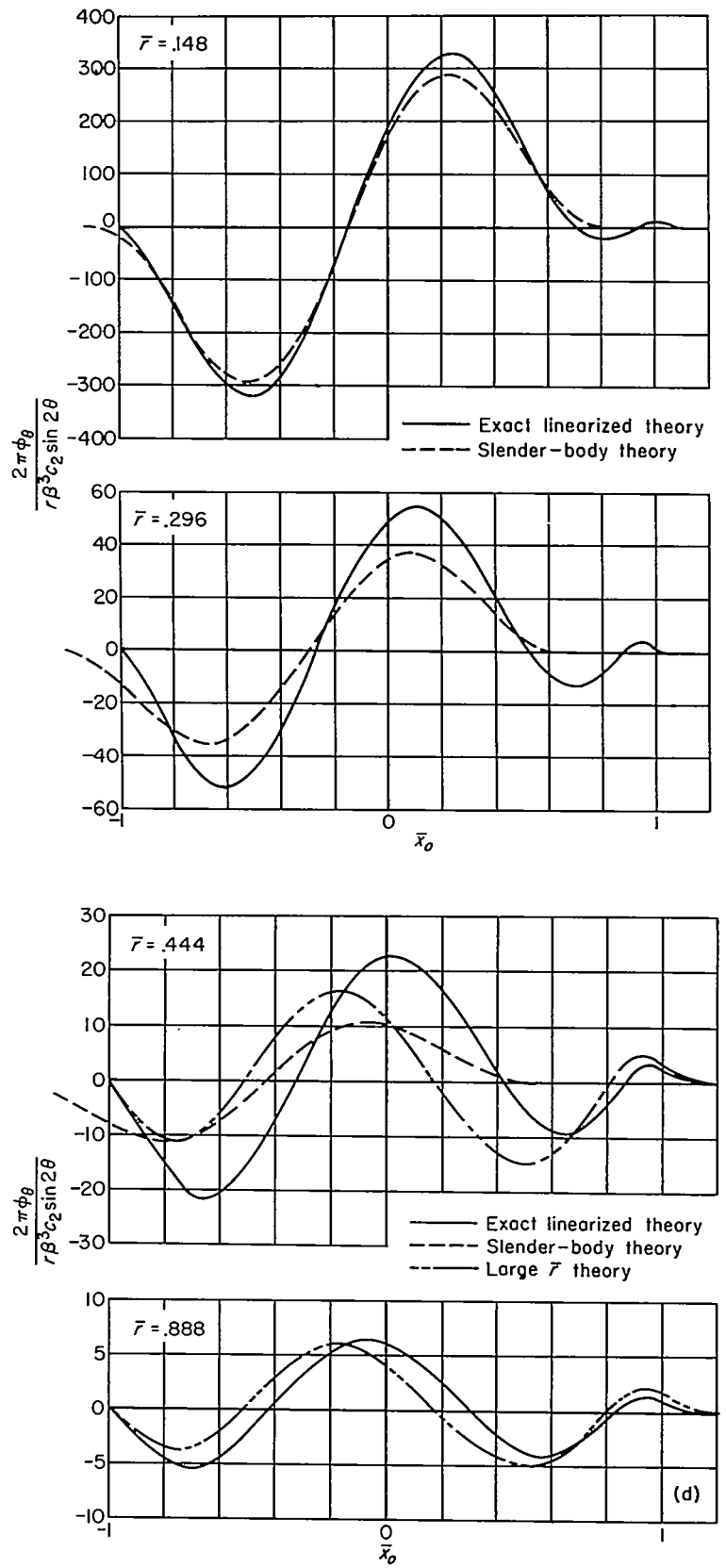(b) Velocities, φ_{o_r}.

FIGURE 11.—Continued.

induced by simple polynomial distributions satisfying, in each case, the end conditions given by equation (17). For particular variations set

$$\left.\begin{array}{l} a_o(\bar{x})=c_o(1-\bar{x}^2)\bar{x} \\[1mm] a_2(\bar{x})=c_2(1-\bar{x}^2)^3\bar{x} \\[1mm] a_4(\bar{x})=c_4(1-\bar{x}^2)^5\bar{x} \end{array}\right\} \qquad (44)$$
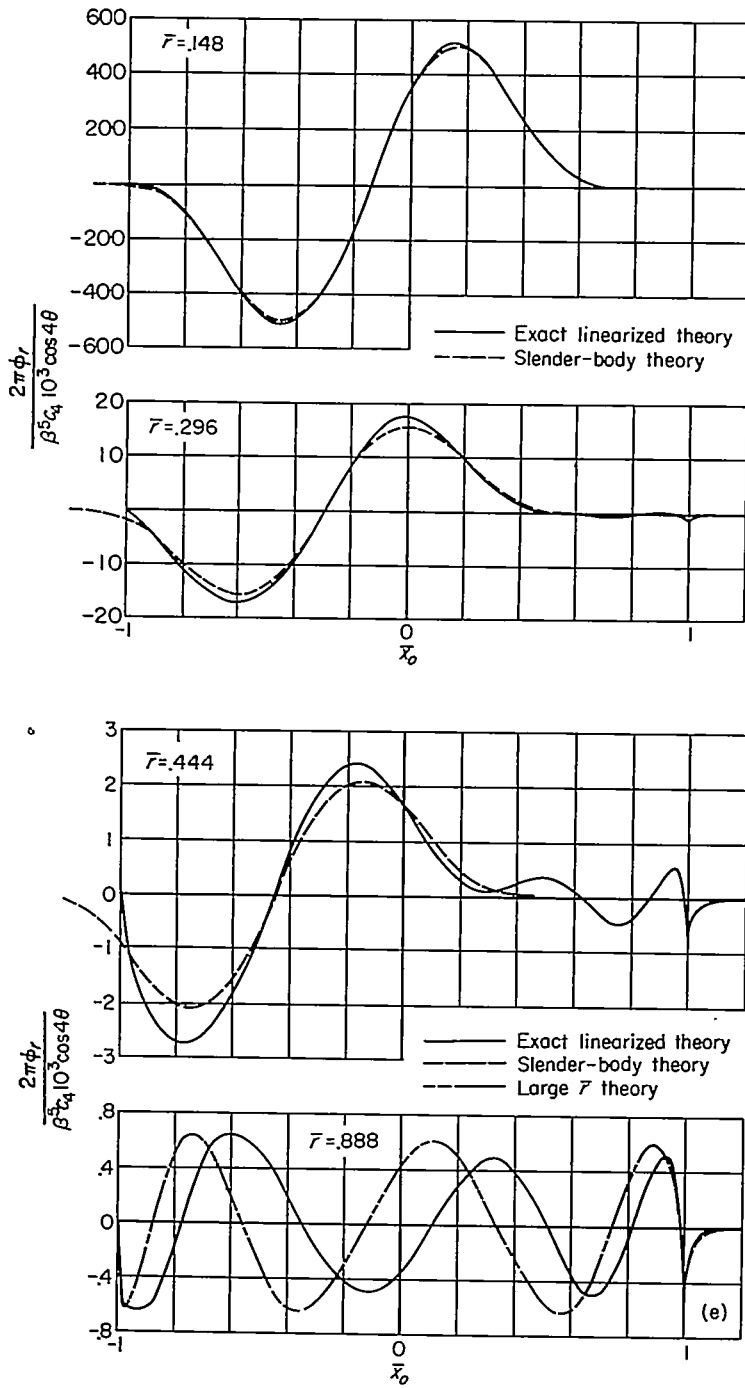
where c_o, c_2, and c_4 are constants determining the amplitudes and $\bar{x}=x/L_o$. Figure 11 (a) shows the variations of these coefficients with $\bar{x}$, and figures 11(b) through 11(f) show

(c) Velocities, φ_{2_r}.

FIGURE 11.—Continued.

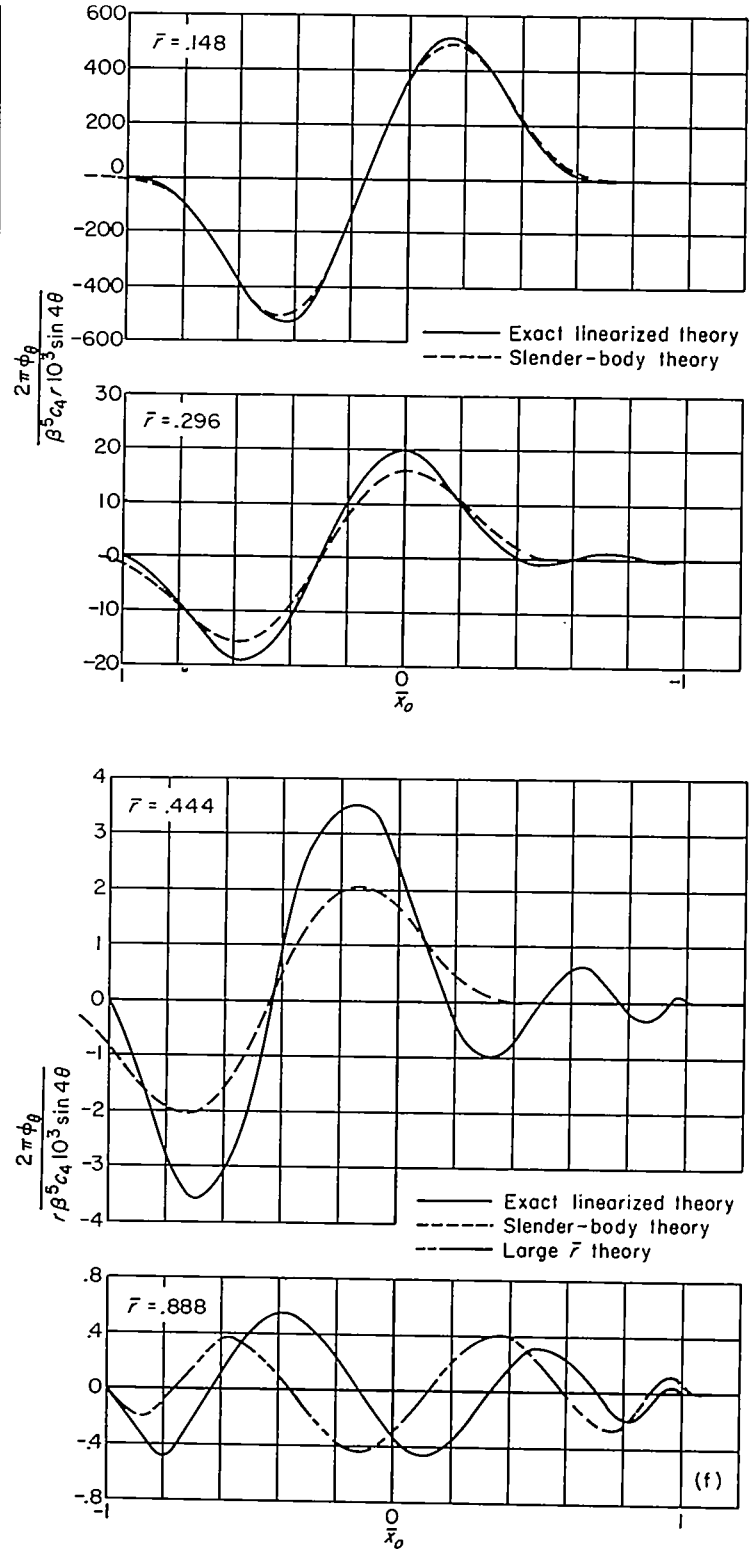(d) Velocities, φ_{2_θ}.

FIGURE 11.—Continued.

(e) Velocities, φ_{4_r}.

FIGURE 11.—Continued.

(f) Velocities, φ_{4_θ}.

FIGURE 11.—Concluded.

how velocities induced by these distributions vary with $\bar{x}_o$ ($\bar{x}_o=\bar{x}-\beta\bar{r}$) and $\bar{r}$ ($\bar{r}=\beta r/L_o$). The results have been compared with those for large $\bar{r}$ given by equation (21) and with those for small $\bar{r}$ given by slender-body theory. Values for the latter theory are determined from equations (9) or (19) by expanding the expressions in powers of r and neglecting all but the first terms. Thus it can be shown

$$(\varphi_{n_r})_{r\to o}=\begin{cases}\dfrac{a_o(x)}{2\pi r}, & n=0\\[2ex]\dfrac{(-2)^n n!\,a_n(x)\cos n\theta}{4\pi r^{n+1}}, & n>0\end{cases} \qquad (45a)$$

$$\frac{1}{r}\,\varphi_{n_\theta})_{r\to o}=\frac{(-2)^n n!\,a_n(x)\sin n\theta}{4\pi r^{n+1}}, \qquad n\geq 0 \qquad (45b)$$

The significance of figure 11 with regard to practical applications is more or less obvious. The first step in its use is to find the effective length of the cancellation-multipole distributions. Since the wing is given, the streamwise variation of the cancellation multipoles can be calculated. Actually

this variation will extend between the apexes of the enclosing Mach forecone and aftercone, a distance of $L_o + L_o'$ (see fig. 10). However, depending on the wing plan form and section, the effective lengths of the distributions (the interval of principal variation) can be considerably less as illustrated in figure 12. Designate this effective length as $2L_e$ and the
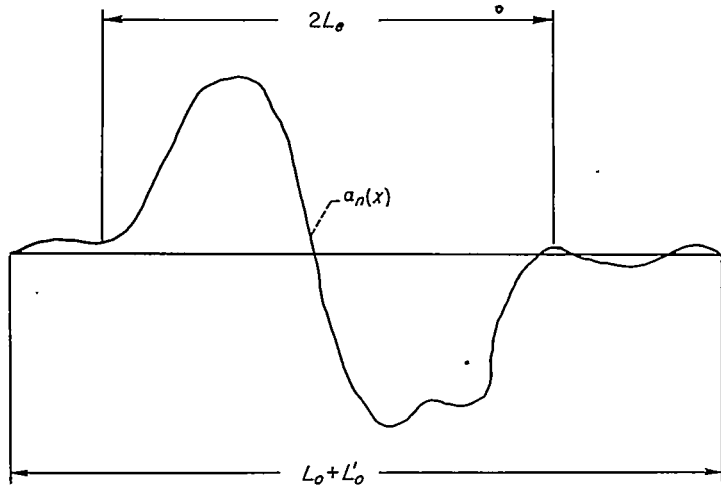

FIGURE 12.—Effective length of multipole distribution.

distance to the vicinity of the body surface as r_e, and one can define the parameter $\bar{r}_e$ thus

$$\bar{r}_e = \frac{\beta r_e}{L_e} \tag{46}$$

Using figure 11 and the parameter $\bar{r}_e$, one can now estimate the error incurred by the use of various approximate methods for calculating the body shape. A convenient way to carry out these estimations is to study the magnitude of the first crest of the waves shown in figures 11 (b) through 11 (f), and the distance this crest lies from the foremost Mach cone. Graphs showing the variations of these quantities with $\bar{r}$ are given in figures 13, 14, and 15.

By means of the above concepts, let us study briefly four different approximate methods that can be used to calculate a body shape.

SLENDER-BODY THEORY

Slender-body theory is represented in figure 14 by the straight lines having the slopes, on the log-log scale, equal to $-(n+1)$ where n is the order of the multipole. Since this theory amounts to an expansion of the equations for the velocities in powers of $\bar{r}$, it obviously represents a good approximation when $\bar{r}_e$ is sufficiently small. Notice that for a given percentage error the limiting value of $\bar{r}_e$ for which the method applies increases as the order of the multipoles in-
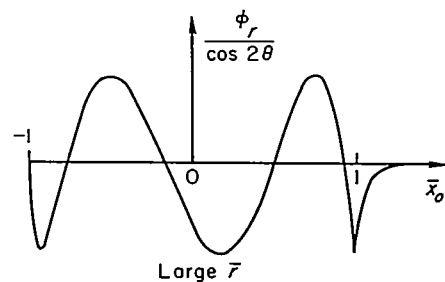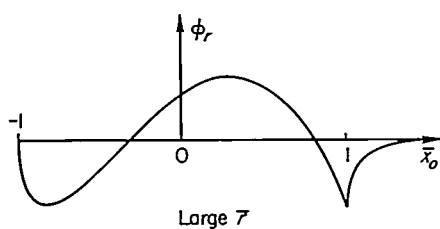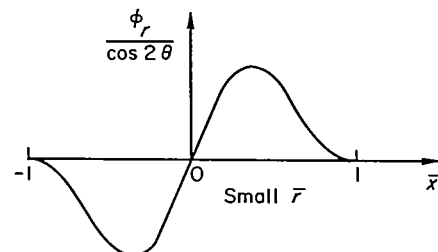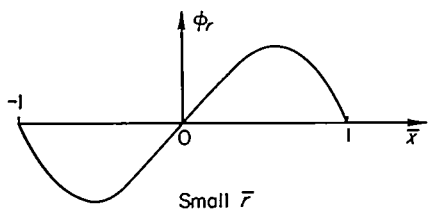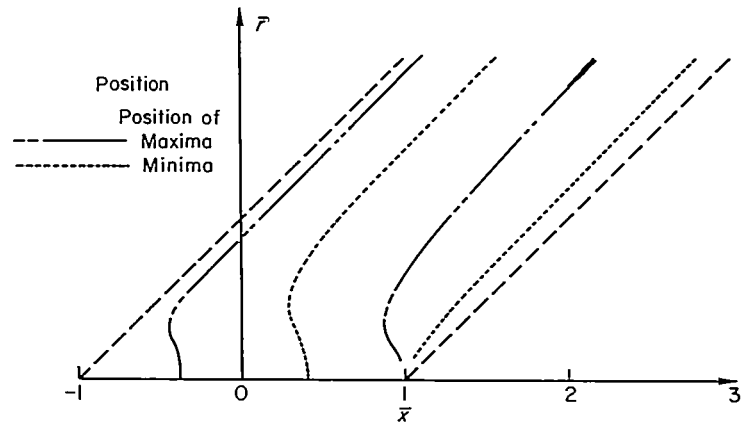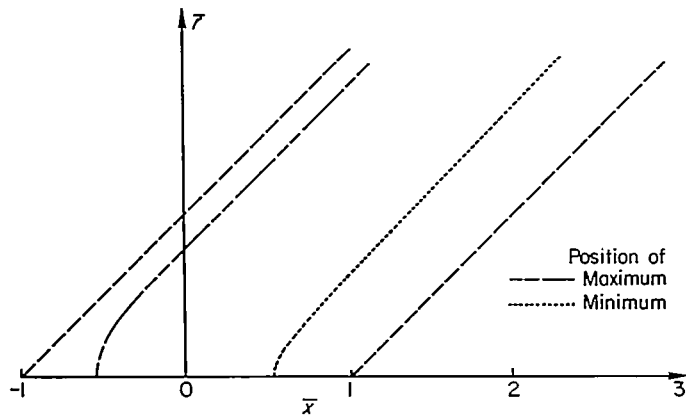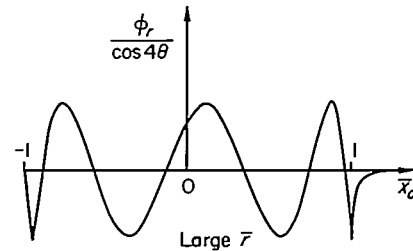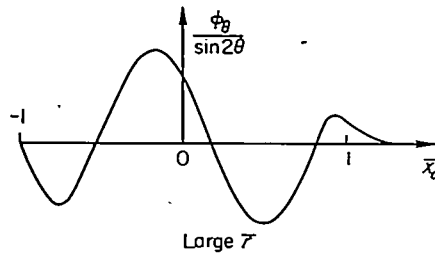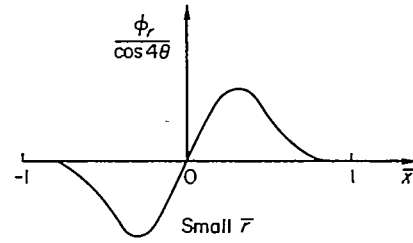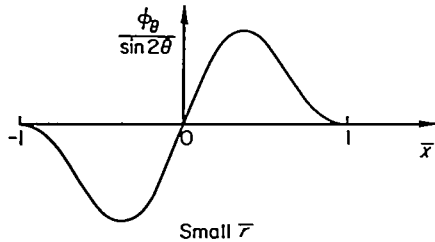

(a) Radial velocities induced by sources.

FIGURE 13.—Positions of crests of waves created by multipole distributions shown in figure 11.

(b) Radial velocities induced by second-order multipoles.

FIGURE 13.—Continued.
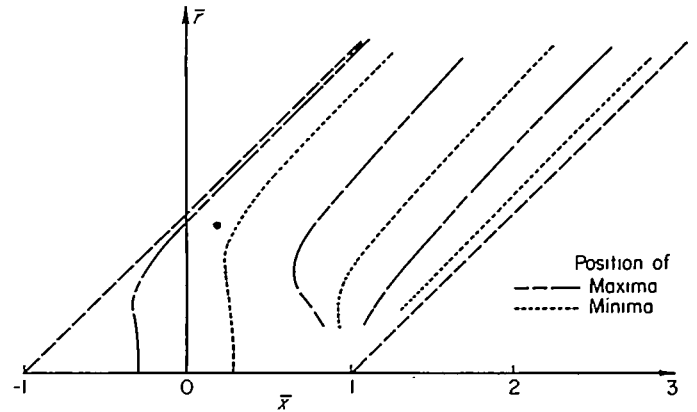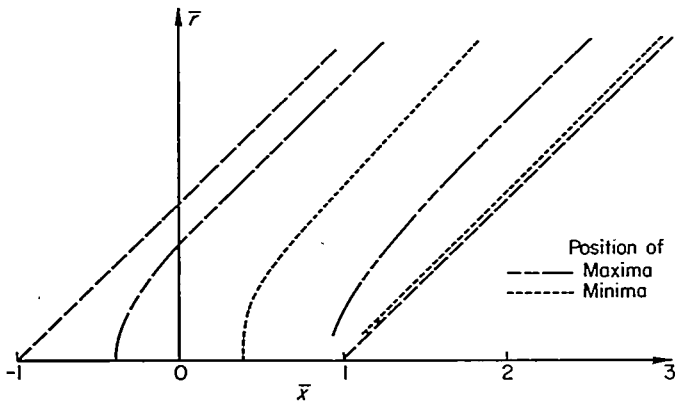
(c) Tangential velocities induced by second-order multipoles.

FIGURE 13.—Continued.

(d) Radial velocities induced by fourth-order multipoles.

FIGURE 13.—Continued.

creases. For example, when $\bar{r}_e=0.2$, φ_{θ_r} as given by slender-body theory is 19 percent less than that given by exact linearized theory for the case shown, whereas φ_{2_r} is only 3 percent less. Correspondingly, the positions of the wave crests follow the path predicted by slender-body theory to larger values of $\bar{r}$ as the order of the multipoles increases. The latter trend is illustrated by figure 15.

If for a particular problem r_e is small enough for slender-body theory to be considered a good approximation, the equation for the body shape, $r=R(x,\theta)$, corresponding to the combined wing and optimum cancellation multipoles defined in equation (36) is determined by the expressions (using equations (45), (36), and (14) together with equation (42))

$$\frac{d\theta}{dx}=\left[\frac{\varphi_\theta(x,R,\theta)}{U_oR^2}\right]_{wing}+\sum_0^\infty \frac{\left(\frac{2}{\beta}\right)^n \sin n\theta}{4\pi^2R^{n+2}}\int_0^{2\pi} d\psi \int_{-L_o'}^x dx_1(x-x_1)^n \cos n\psi S_w''(x_1,\psi) \tag{47a}$$

$$\frac{dR}{dx}=\left[\frac{\varphi_r(x,R,\theta)}{U_o}\right]_{wing}+\sum_0^\infty \frac{\left(\frac{2}{\beta}\right)^n \cos n\theta}{4\pi^2R^{n+1}}\int_0^{2\pi} d\psi \int_{-L_o'}^x dx_1(x-x_1)^n \cos n\psi S_w''(x_1,\psi) \tag{47b}$$

(e)
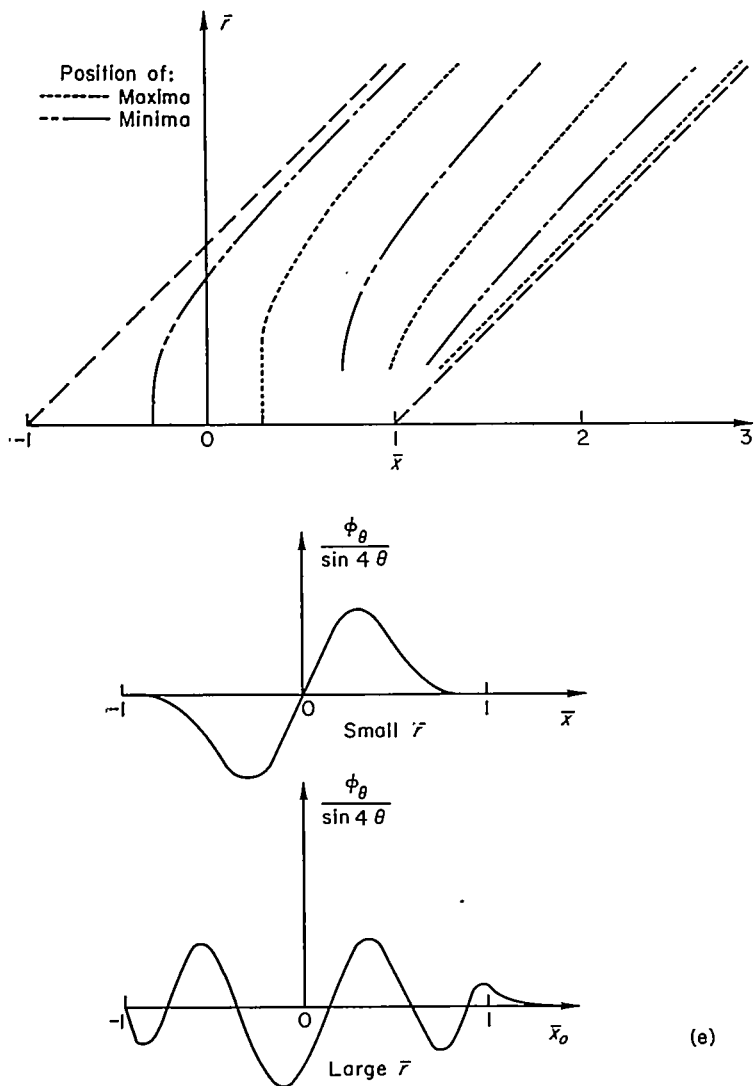
(c) Tangential velocities induced by fourth-order multipoles.
FIGURE 13.—Concluded.
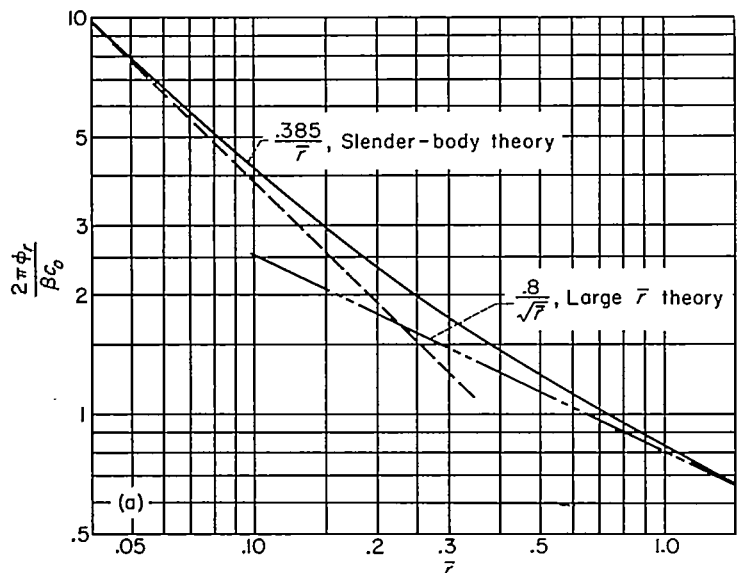
(a) φ_{0_r}

FIGURE 14.—Attenuation of first crest of waves created by multipole
distributions shown in figure 11.
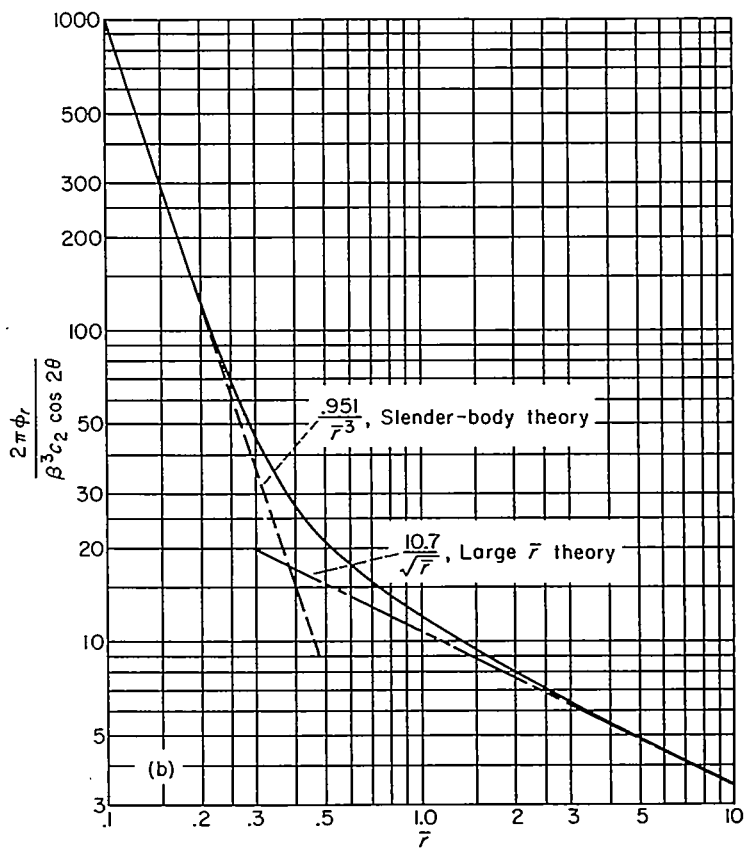
(b) φ_{2_r}

FIGURE 14.—Continued.
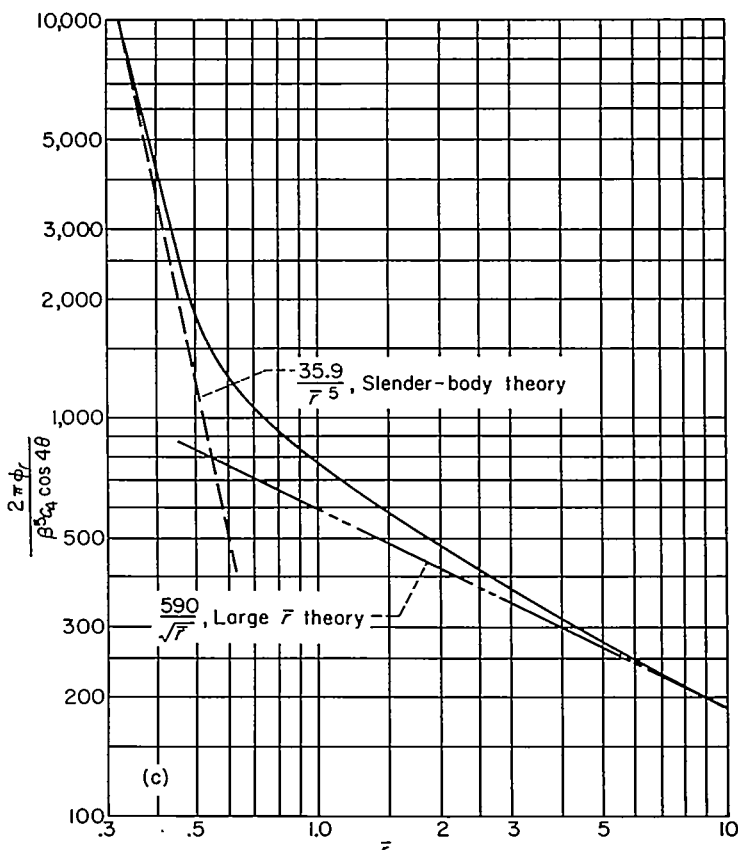
(c) φ_{4_r}

FIGURE 14.—Continued.
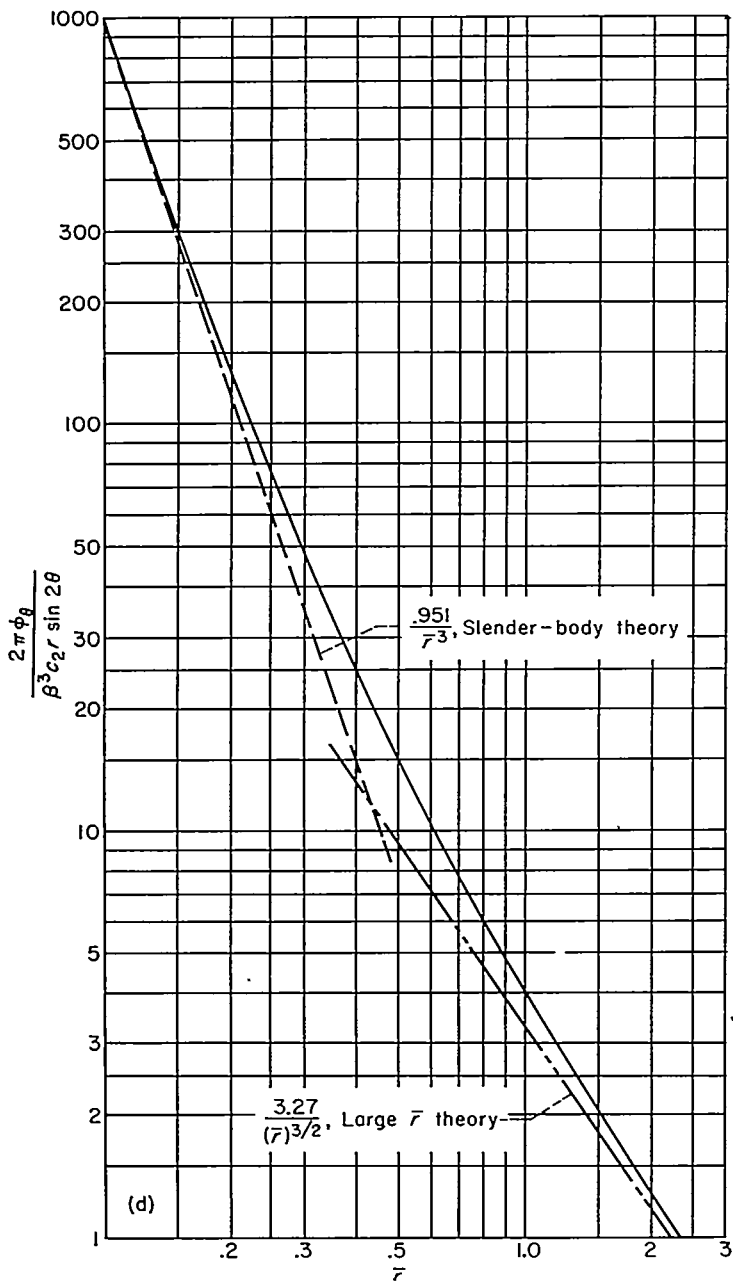
(d) $\varphi_{2\theta}$

FIGURE 14.—Continued.

(e) $\varphi_{4\theta}$

FIGURE 14.—Concluded.

Approximate methods for finding $(\varphi_\theta/U_oR)_{wing}$ and $(\varphi_r/U_o)_{wing}$, the velocities induced by the wing, can often be used also; but these apply to individual cases and cannot be discussed here.

THEORY FOR LARGE $\bar{r}_e$

The asymptotic values for magnitude and position of the first wave crest obtained by placing equations (44) into
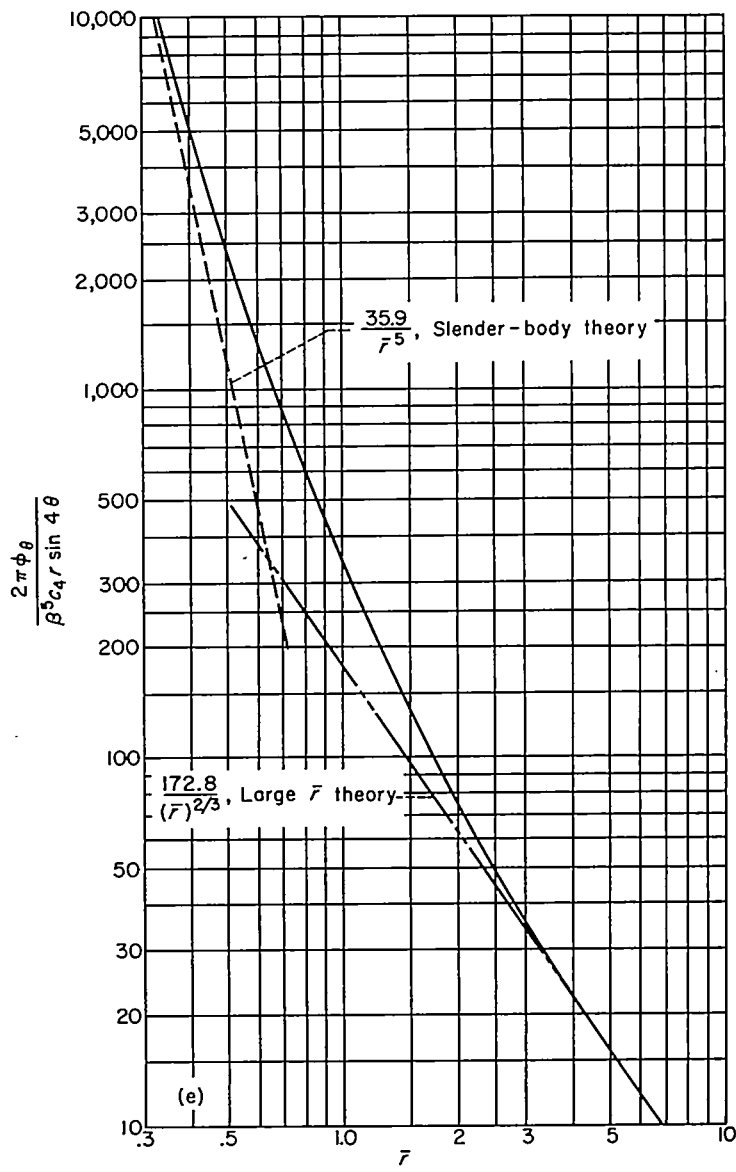
equations (21) are also shown in figures 13, 14, and 15. For $n \leq 4$ it is clear that this theory can be used when $\bar{r}_e$ is greater than about 2.

CONTROL-SURFACE THEORY

The approximations inherent in ordinary control-surface theory can also be estimated by inspecting figures 14 and 15, where by control-surface theory one means that the
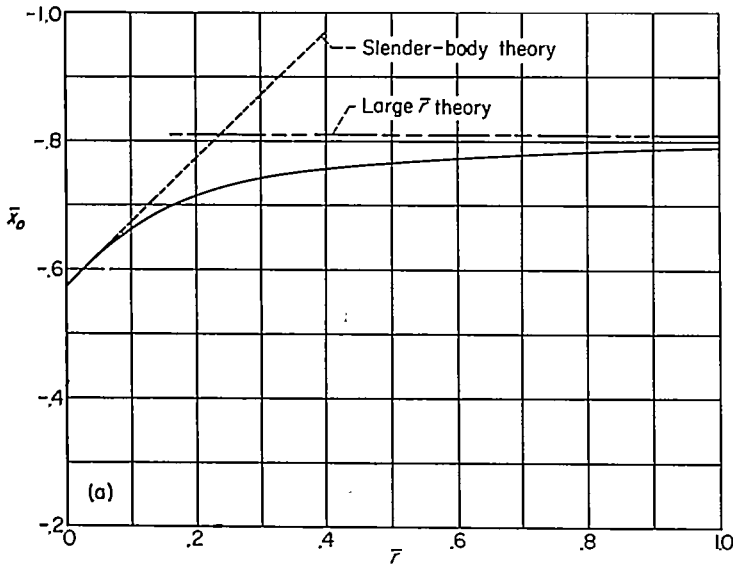
(a) Radial velocities induced by sources.

FIGURE 15.—Position of first crest of waves created by multipole distributions shown in figure 11.
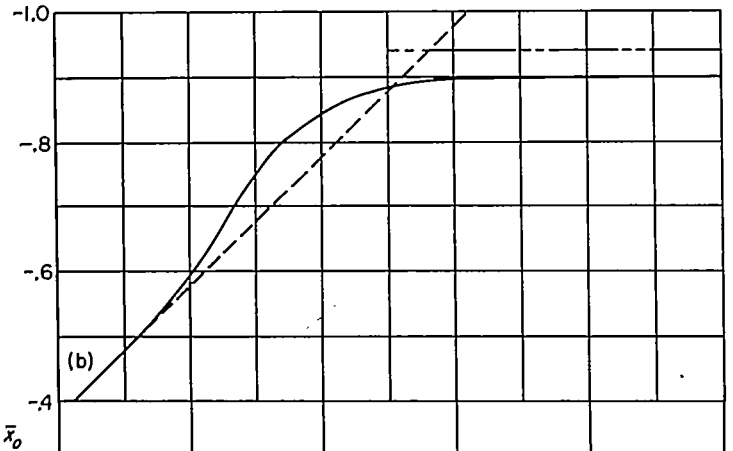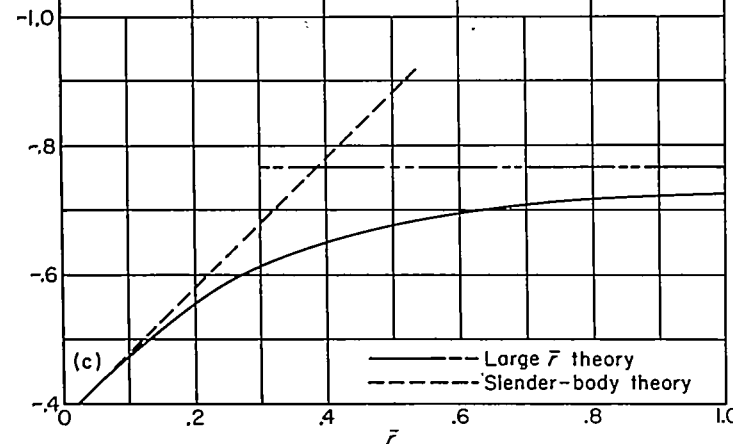
(b) Radial velocities induced by second-order multipoles.
(c) Tangential velocities induced by second-order multipoles.
FIGURE 15.—Continued.
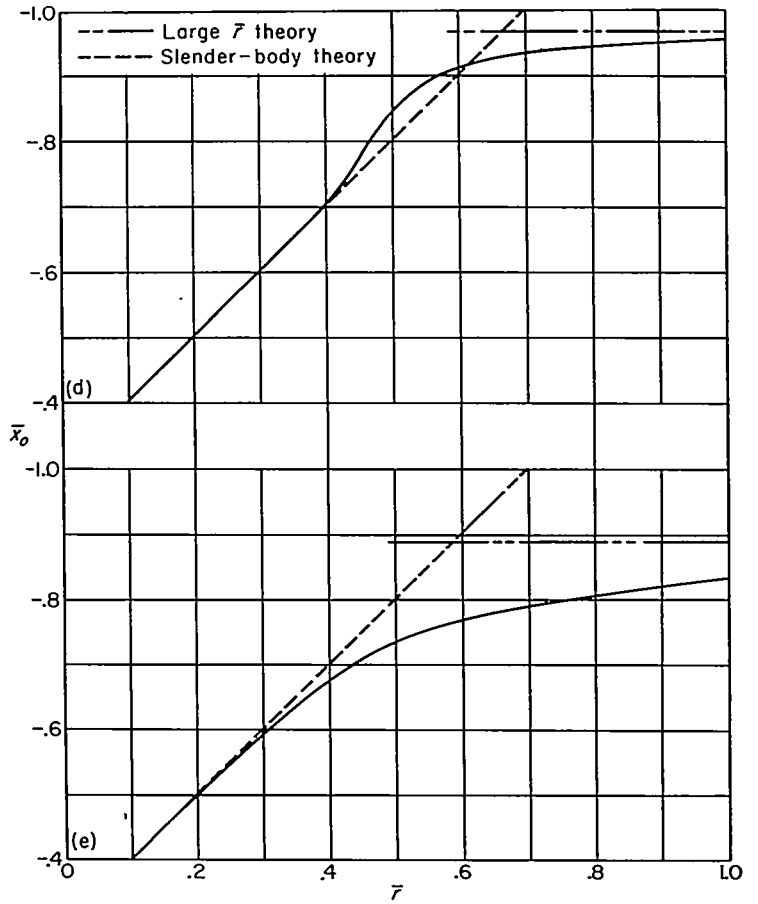
(d) Radial velocities induced by fourth-order multipoles.
(e) Tangential velocities induced by fourth-order multipoles.
FIGURE 15.—Concluded.

exact linearized theory is used to evaluate induced velocities along a given surface and these values are assumed constant for all $\bar{r}$ in the vicinity of the surface. As shown in figure 16, this amounts to assuming φ_r and φ_θ are given by a straight horizontal line in figure 14 and by straight lines with a unit negative slope in figure 15. Obviously, the error in the body shape calculated by this theory increases as the amplitudes of the disturbing multipoles increase and as the radius of the control surface diminishes.

One of the simplest applications of control-surface theory arises in the study of quasi-cylindrical bodies. In such cases the expression for the body surface can be derived immediately from equation (42). Thus, if the amplitudes of the cancellation multipoles are small enough and R_c, the radius of the control surface, is large enough for control-surface theory to be considered a good approximation, the body shape, $r=R(x,\theta)$, corresponding to the combined wing and optimum cancellation multipoles is determined by using equations (19c), (16b), and (36) together with equation (42)

$$\frac{dR}{dx}=\left[\frac{\varphi_r(x,R_c,\theta)}{U_o}\right]_{wing}+\sum_0^\infty \frac{\sigma_n \cos n\theta}{4\pi^2 R_c}\int_{-L_0'}^{x-\beta R_c}\frac{(x-\xi)\cosh\left(n\cosh^{-1}\frac{x-\xi}{\beta R_c}\right)d\xi}{\sqrt{(x-\xi)^2-\beta^2 R_c^2}}\int_0^{2\pi}S_w''(\xi,\psi)\cos n\psi\,d\psi \qquad (48)$$

where $\sigma_n=1$ for $n=0$ and $\sigma_n=2$ for $n>0$.

$$\int_{-L_o'}^{x-\beta R_c} \frac{(x-\xi)\cosh\left(n\cosh^{-1}\frac{x-\xi}{\beta R_c}\right)d\xi}{\sqrt{(x-\xi)^2-\beta^2 R_c^2}}$$

$$\int_0^{2\pi} S_w''(\xi,\psi)\cos n\psi\, d\psi \qquad (49)$$

which can be solved using numerical techniques.

A further refinement of equation (49) can be obtained if the position of the induced velocities is also varied according to the slope (again at $\bar{r}=\bar{r}_e$) of the curves in figure 15. Defining this slope as δ_n, see figure 17, and x_δ as

$$x_\delta = x - \beta(1+\delta_n)(R-R_c)$$

one can see this refinement simply amounts to replacing the value of x in the right-hand term of equation (49) by x_δ.

ILLUSTRATIVE EXAMPLE—ELLIPTIC WING

In order that one may be able to assess the practical significance of the preceding sections, the concepts presented therein will now be applied to the solution of a particular problem. For the basic wing plan form in this particular

FIGURE 16.—Comparison of velocity fields given by exact-linearized and control-surface theory.

A study of optimum fuselage shapes using control-surface theory has been carried out by Nielsen (ref. 10) for a constant-chord sweptback wing having a biconvex section and a sonic leading edge. The set of interfering singularities used in reference 10 are equivalent (the singularities are limited to the x axis) to the multipoles used herein. The fuselage shapes calculated by Nielsen are thus the same—within the accuracy of control-surface theory—as those given by equation (48).

MODIFIED CONTROL-SURFACE THEORY

A method of modifying control-surface theory to increase its accuracy is illustrated in figure 17. Induced velocities computed by this method are based on those calculated along a given control surface but are extended away from this surface by varying their magnitude as $(\bar{r})^{\gamma_n}$ where the value of γ_n is fixed by the slope of the curves in figure 14 at $\bar{r}=\bar{r}_e$, $\bar{r}_e$ being defined by equation (46) (fig. 17). With this modification equation (48) becomes

$$\frac{dR}{dx}=\left[\frac{\varphi_r(x,R_c,\theta)}{U_o}\right]_{wing}+\sum_0^\infty \left(\frac{R_c}{R}\right)^{\gamma_n}\frac{\sigma_n\cos n\theta}{4\pi^3 R_c}$$
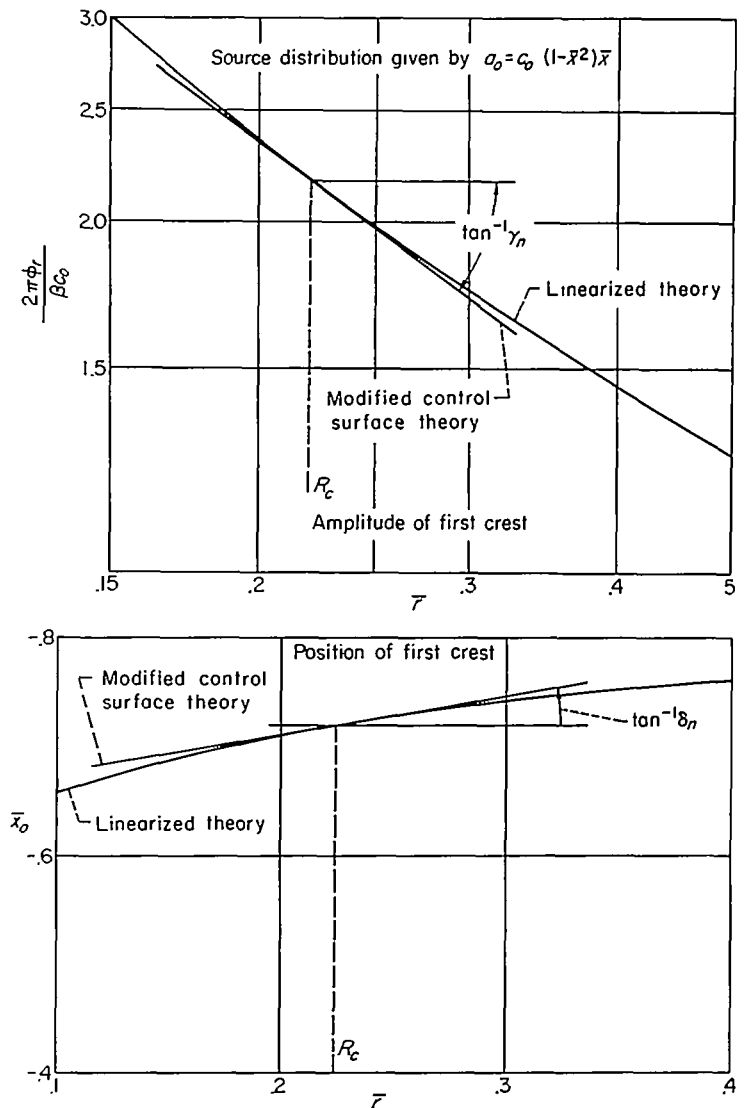

FIGURE 17.—Comparison of velocity fields given by exact-linearized and modified control-surface theory.

example an ellipse will be chosen. There are two good reasons for this choice; first, the ellipse is effectively unswept and places a severe test on the role of body interference in reducing the wave drag at a supersonic speed, and, second, for a given volume, the optimum section (i. e., the one yielding minimum wave drag) for these wings when considered separately has been discovered (see ref. 11) so the reduction in wave drag brought about by the body will reduce the minimum value possible for such wings when flying alone. The drag reductions for the first few cancellation-multipole distributions will be calculated and compared with the total drag of the wing alone, the wing mounted on an infinite cylinder, and the wing mounted on a basic body of revolution. Finally the details of calculating a body shape simulated by the wing source sheet, a source line representing a basic body of revolution, and the first two optimum cancellation-multipole distributions will be carried out.

THE ELLIPTIC WING

Consider the elliptic lens specified by the equation

$$z=\pm\frac{t}{2}\left(1-\frac{x^2}{a^2}-\frac{y^2}{b^2}\right) \tag{50}$$

where the thickness, span, and chord are shown in figure 18. The streamwise slope of the upper surface is seen to be

$$\frac{\partial z}{\partial x}\bigg|_u=\lambda_u(x,y)=-\frac{tx}{a^2} \tag{51}$$

and the total wing plan-form area S and volume V are, respectively,

$$\left.\begin{array}{c} S=\pi ab \\ V=\frac{\pi}{2}\,tab \end{array}\right\} \tag{52}$$

Wing plan form

Root section
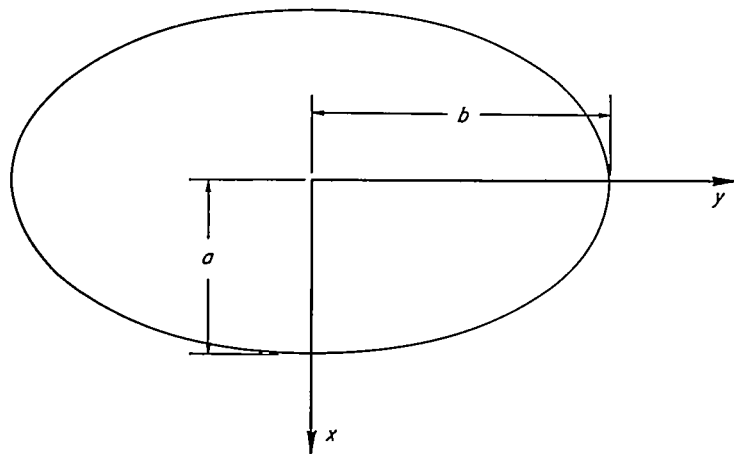
FIGURE 18.—Definition of parameters used to study elliptic wing.

435875—57——47
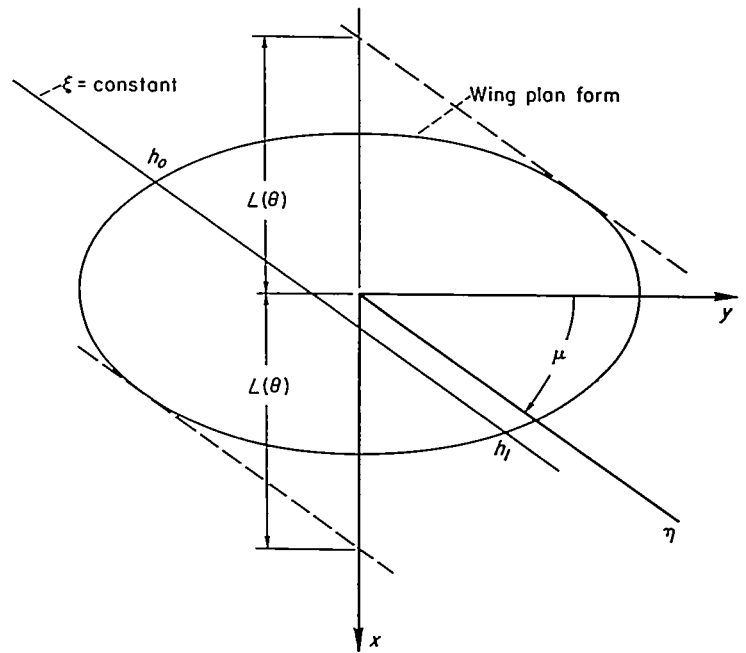
FIGURE 19.—Elliptic wing in ξ,η coordinates.

Wave drag.—The wave drag of the elliptic wing represented by equation (50) can be calculated by means of equation (30) in which, since one wishes now to find the wave drag of the wing alone, the a_n's are set equal to zero. The value of $S_w'(x,\theta)$ follows by placing equation (51) into equation (28) and integrating. Thus

$$U_oS_w'(x,\theta)=2U_o\cos\mu\int_{h_o}^{h_1}\left(-\frac{t}{a^2}\right)(\xi+\eta\sin\mu)d\eta=$$

$$-\frac{2tU_o\cos\mu}{a^2}\left(\xi\eta+\frac{\eta^2\sin\mu}{2}\right)_{h_o}^{h_1}$$

where, by referring the equation of the plan form to the ξ,η coordinates (see eq. (26)) and solving for the points where the straight line $\xi=$constant intersects the wing edges, one finds—see figure 19

$$\left.\begin{array}{c} h_1 \\ h_o \end{array}\right\}=\frac{-b^2\xi\sin\mu\pm ab\sqrt{a^2\cos^2\mu+b^2\sin^2\mu-\xi^2\cos^2\mu}}{a^2\cos^2\mu+b^2\sin^2\mu}$$

Hence,

$$S_w'(x,\theta)=-\frac{4xtab}{(a^2+b^2\beta^2\cos^2\theta)^2}\sqrt{a^2+b^2\beta^2\cos^2\theta-x^2} \tag{53}$$

From the relation

$$L^2(\theta)=a^2+b^2\beta^2\cos^2\theta \tag{54}$$

the wave drag can be expressed in the form (integrating once by parts)

$$\frac{D}{q}=-\frac{1}{4\pi^2}\int_0^{2\pi}d\theta\int_{-L(\theta)}^{L(\theta)}d\xi_1\int_{-L(\theta)}^{L(\theta)}d\xi_2\left[\frac{4\,tab}{L^4(\theta)}\right]^2$$

$$\left[\frac{L^2(\theta)-2\xi_1^2}{\sqrt{L^2(\theta)-\xi_1^2}}\right]\frac{\xi_2\sqrt{L^2(\theta)-\xi_2^2}}{\xi_1-\xi_2}$$

Further integration yields

$$\frac{D}{q}=t^2a^2b^2\int_0^{2\pi}\frac{d\theta}{(a^2+b^2\beta^2\cos^2\theta)^2}$$

Values of ϕ_r/U_0

Point number	Exact linearized theory	Ackeret wave— $f(x-r)/a^2$
1	.044	.050
2	-.053	-.050
3	-.102	-.100
4	-.104	-.100

Region to be occupied by body streamline
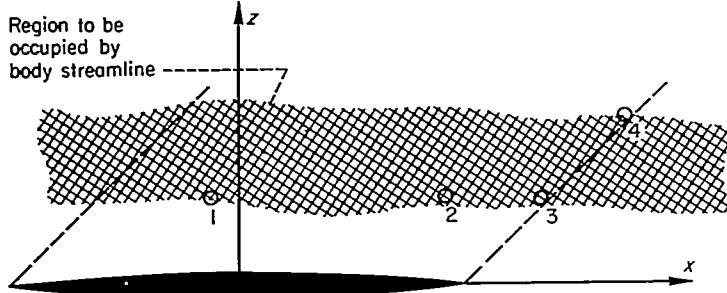
FIGURE 20.—Points at which exact-linearized theory was compared with an Ackeret wave in plane of symmetry for elliptic wing.

Finally, the wave drag can be expressed in coefficient form, based on the total wing area πab, as

$$C_D = \frac{4}{\beta}\left(\frac{t}{2a}\right)^2 \frac{1+2\left(\frac{a}{b\beta}\right)^2}{\left[1+\left(\frac{a}{b\beta}\right)^2\right]^{3/2}} \qquad (55)$$

Equation (55) represents the lowest value of wave drag possible for a wing having an elliptic plan form and fixed volume. This equation was first derived by Jones in reference 11.

The velocities induced by the wing source sheet in the vicinity of the fuselage.—Later, when one wishes to calculate a stream surface in the presence of the source sheet that simulates the wing given by equation (50), it is necessary to know the velocities induced by these sources at the body surface. Hence, the value of φ_r induced by the source sheet was calculated at the four points indicated in figure 20. As it turns out, these values are so close (see the figure for a numerical comparison) to those obtained by assuming the source sheet to be two-dimensional with a chordwise intensity identical to that along the root section of the elliptical sheet (i. e., using the Ackeret wave generated by the root section) that the effect of the wing can be assumed to be given everywhere in the vicinity of the body by the latter velocity field if (as will be the case in subsequent application) the surface of the body passes through the region shaded in the figure. That is, the effect of the wing in the equations for the fuselage shape (such as eqs. (47), (48), or (49)) is assumed to be

$$\frac{1}{U_o}\varphi_r = \mp\frac{t}{a^2}(x\mp\beta r\sin\theta)\sin\theta, \quad \begin{matrix} -\text{for } 0\leq\theta\leq\pi \\ +\text{for }\pi\leq\theta\leq2\pi \end{matrix}$$

$$\frac{1}{rU_o}\varphi_\theta = \mp\frac{t}{a^2}(x\mp\beta r\sin\theta)\cos\theta, \quad \begin{matrix} -\text{for } 0<\theta<\pi \\ +\text{for }\pi<\theta<2\pi \end{matrix} \Biggr\} \quad (56)$$

THE OPTIMUM CANCELLATION MULTIPOLES

One can now find the strengths of the multipoles along the x axis which induce around a cylinder of infinite radius a momentum field identical to that created there by the elliptic wing. The negatives of these variations are, according to

equation (36), the optimum cancellation multipoles. Hence, combining equations (53) and (36)

$$\alpha_n^{(n)}(x) = -\sigma_n\frac{2tabU_ox}{\pi(-\beta)^n}\int_0^{2\pi}\frac{\sqrt{a^2+b^2\beta^2\cos^2\theta-x^2}}{(a^2+b^2\beta^2\cos^2\theta)^2}\cos n\theta\, d\theta \qquad (57)$$

where $\sigma_n=1$ for $n=0$ and $\sigma_n=2$ for $n>0$. Particular variations of $\alpha_n^{(n)}(x)$ are shown in figure 21. These results are

(a) $n=0$

(b) $n=2$

(c) $n=4$

FIGURE 21.—Variation of nth derivative of nth-order cancellation multipoles for elliptic wing.

for $n=0$, 2, and 4, since $\alpha_n^{(n)}(x)$ for any odd n is zero by symmetry, and apply when the wing plan for and free-stream Mach number are related by

$$\frac{a}{b\beta}=\frac{4}{3\pi}\qquad(58)$$

which contains the particular case for which the Mach number is $\sqrt{2}$ and the aspect ratio is 3. It is apparent that there are at least $n+1$ roots to $\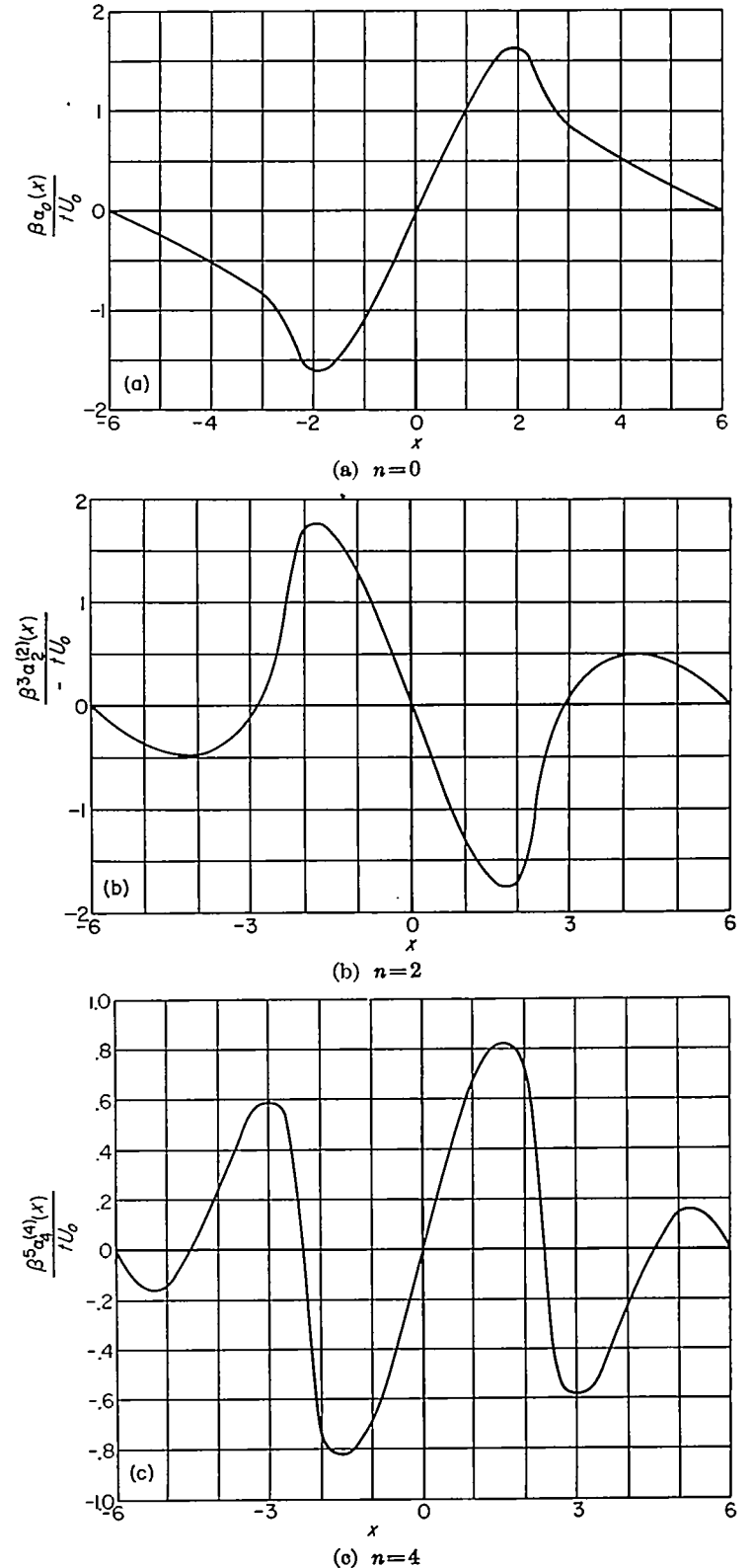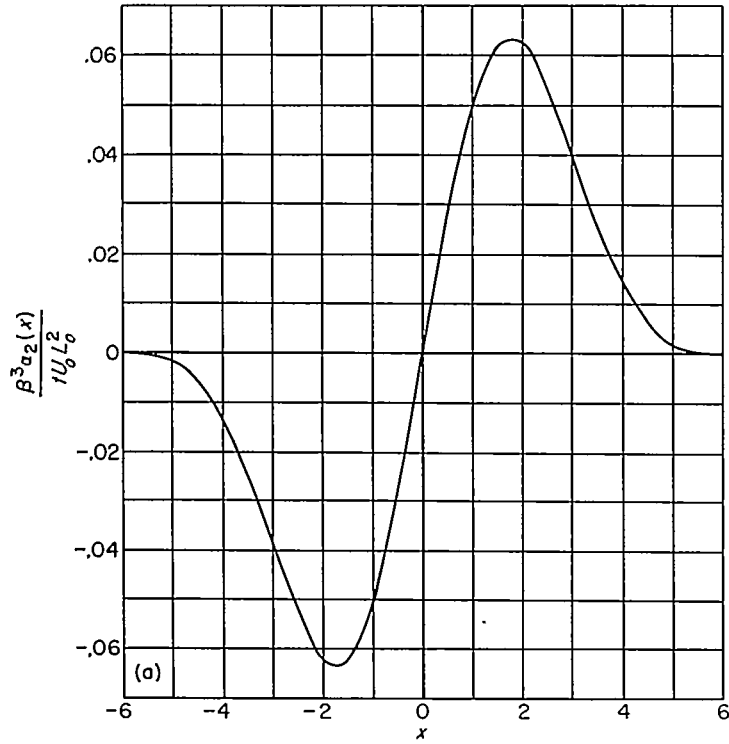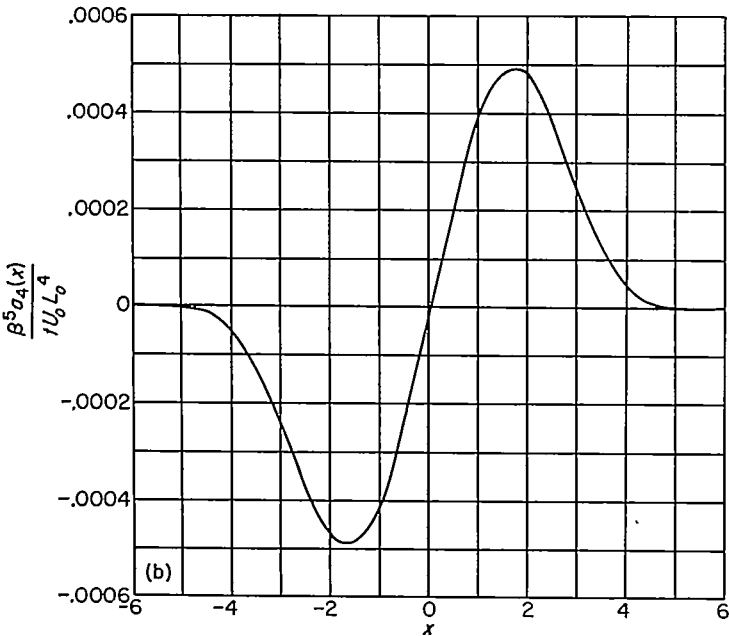alpha_n^{(n)}(x)$ for $-L_o<x<L_o$. This follows immediately from equation (38) and is true in general. As a result the curves for the higher values of n

(a) $n=2$

(b) $n=4$

FIGURE 22.—Variation of nth-order cancellation multipoles for elliptic wing.

become increasingly wavy and, correspondingly, increasingly difficult to evaluate numerically.

Figure 22 presents the values of $\alpha_n(x)$ for the same elliptic-wing Mach number relation given by equation (58). Notice that each of these curves has only one root (they necessarily have at least one) in the interval $-L_o<x<L_o$ and is increasingly smooth with increasing n. The latter follows from equation (37) and the fact that the first n derivatives of these curves must, in general, be continuous. For example at $x=\pm L_o$ the first four derivatives of $\alpha_4(x)$ must vanish.

Wave drag.—One can now calculate how much the wing-alone drag is reduced when combined with each successive optimum cancellation-multipole distribution. If $\overline{D}_n$ denotes the drag saved by the nth-order cancellation multipoles, then by equation (35)

$$\frac{\overline{D}_n}{q}=-\frac{\beta^{2n}}{4\pi U_o{}^2}\int_{-L_o}^{L_o}dx_1\int_{-L_o}^{L_o}dx_2\alpha_n^{(n+1)}(x_1)\alpha_n^{(n+1)}(x_2)\ln|x_1-x_2|\qquad(59)$$

where L_o is the maximum value of $L(\theta)$ as given by equation (54)

$$L_o{}^2=a^2+b^2\beta^2\qquad(60)$$

The total drag saved by means of the first m multipole distributions, would, by equation (34), be

$$\overline{D}=2\overline{D}_o+\sum_1^m\overline{D}_n\qquad(61)$$

Using equations (53) and (36) to define the $\alpha_n^{(n+1)}(x)$ in equation (59), reversing the order of integration, and integrating once by parts, one finds

$$\frac{\overline{D}_n}{q}=\frac{-4}{\pi^3}\int_0^{\pi/2}\cos n\theta_1 d\theta_1\int_0^{\pi/2}\cos n\theta_2 d\theta_2\int_{-L(\theta_1)}^{L(\theta_1)}d\xi_1\int_{-L(\theta_2)}^{L(\theta_2)}d\xi_2$$

$$\frac{(4\,tab)^2}{L^4(\theta_1)L^4(\theta_2)}\frac{L^2(\theta_1)-2\xi_1{}^2}{\sqrt{L^2(\theta_1)-\xi_1{}^2}}\frac{\xi_2\sqrt{L^2(\theta_2)-\xi_2{}^2}}{\xi_1-\xi_2}$$

$$=-\frac{64\,(tab)^2}{\pi^3}\int_0^{\pi/2}\cos n\theta_1 d\theta_1\int_0^{\pi/2}\cos n\theta_2 d\theta_2$$

$$\begin{cases}-\pi^2/4L^4(\theta_2), & L^2(\theta_1)\leq L^2(\theta_2)\\ -\pi^2/4L^4(\theta_1), & L^2(\theta_1)\geq L^2(\theta_2)\end{cases}$$

It is apparent from figure 23 that this can be written

$$\frac{\overline{D}_n}{q}=\frac{16(tab)^2}{\pi}\left[\int_0^{\pi/2}\frac{\cos n\theta_1 d\theta_1}{L^4(\theta_1)}\int_{\theta_1}^{\pi/2}\cos n\theta_2 d\theta_2+\right.$$

$$\left.\int_0^{\pi/2}\cos n\theta_1 d\theta_1\int_0^{\theta_1}\frac{\cos n\theta_2}{L^4(\theta_2)}d\theta_2\right]$$

or

$$\frac{\overline{D}_n}{q}=\frac{32(tab)^2}{\pi}\int_0^{\pi/2}\frac{\cos n\theta_1 d\theta_1}{(a^2+b^2\beta^2\cos^2\theta_1)^2}\int_{\theta_1}^{\pi/2}\cos n\theta_2 d\theta_2\qquad(62)$$

The total drag saved by using all the cancellation multipoles is, by definition,

$$\frac{\overline{D}}{q}=\frac{16\,(tab)^2}{\pi}\int_0^{\pi/2}\frac{d\theta_1}{(a^2+b^2\beta^2\cos^2\theta_1)^2}\left(\frac{\pi}{2}-\theta_1\sum_{n=1}^{\infty}\frac{1}{n}\sin 2n\theta_1\cos 2n\theta_1\right)$$
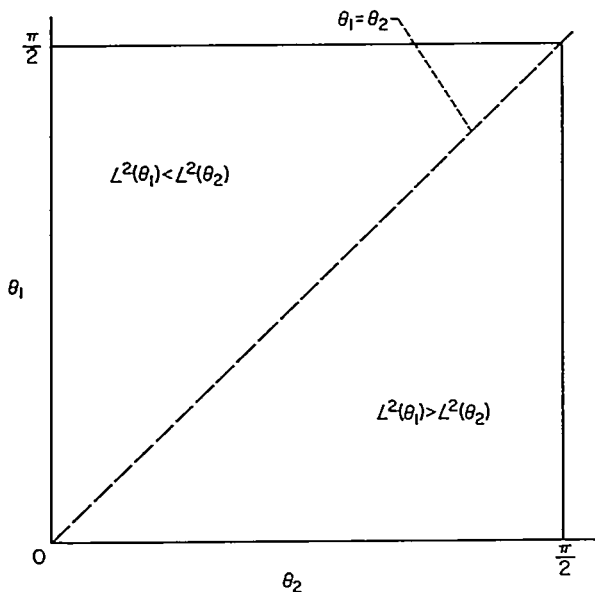
FIGURE 23.—Regions used in developing equation (62).

and since

$$x=\frac{\pi}{4}-\sum_{n=1}^{\infty}\frac{1}{n}\sin 2nx \cos 2nx$$

this is equal to the drag of the wing alone, as it, of course, should be.

The reduction in wave drag as the wing is combined with the first three optimum cancellation multipoles is presented in figure 24. In studying figure 24, one sees, as the Mach number approaches 1 (i. e., $\beta \rightarrow 0$), more and more of the original wing wave drag is destroyed by a line of simple sources alone. Further, the value of $\bar{r}_e$ which can be written—see equations (46), (54), and figures 21 and 22—

$$\bar{r}_e=\frac{\beta r_e}{\sqrt{a^2+b^2\beta^2}} \tag{63}$$

tends (for a fixed average distance to the body surface r_e) to zero as the Mach number approaches 1; and this, in turn, means that as β goes to zero the effect of the multipole strengths on the body shape can be calculated using slender-body theory.
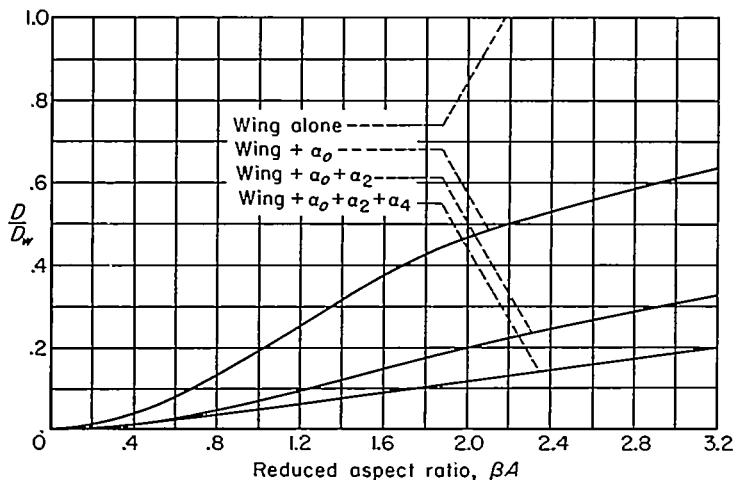
FIGURE 24.—Portions of elliptic-wing wave drag created by various equivalent multipole distributions.
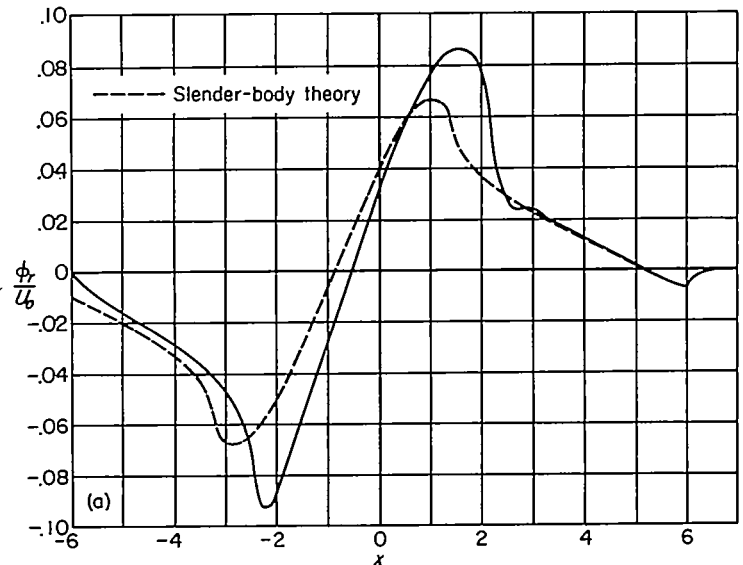
(a) Radial velocities induced by sources.
FIGURE 25.—Velocities induced by the elliptic-wing cancellation multipoles at the control surface where $\beta R/L_e=0.148$.

When various orders of multipoles are distributed along a line, one can show the cross-sectional area normal to the free stream of the simulated body as given by slender-body theory is a function of the source distribution only (see Appendix B). Coupled with the discussion in the preceding paragraph, this can be used to demonstrate that, for Mach numbers close to 1, the "supersonic area rule" proposed by Jones (ref. 12) and Whitcomb and discussed in reference 13 gives a good approximation for the wave drag of an elliptic wing and body combination which is symmetrical with respect to the plane of the wing.

The induced velocity field.—A method for calculating the velocity field induced by the multipoles when $\alpha_n(x)$ is given numerically is presented in Appendix C. By means of this method, velocities induced by the α_0 and α_2 multipole distributions shown in figure 22 have been calculated for $\bar{r}$ equal to 0.148 and the results are shown in figure 25. Since the distributions in figure 22 were for the particular case $a/b\beta=4/3\pi$, it is evident from equation (63) that the values in figure 25 apply to the case r_e/b equal to 0.161; that is, when the body radius is about 16 percent of the wing semispan.

For comparative purposes, the values given by slender-body theory are also shown in figure 25. The degree of agreement between the two curves is consistent with the results shown in figures 14 and 15.

INTERPRETATION OF DRAG REDUCTIONS

Comparison with wing mounted on a circular cylinder.—With regard to figure 24 one should be careful to notice that the drag of the wing alone has been used for the reference drag. The drag reductions shown, therefore, represent gains brought about by interfering with the velocity field induced by a planar source sheet, or, in terms of a combination with an upstream cylindrical stream surface, gains made by modifying a body, shown in figure 26, which bulges behind the wing leading-edge Mach wave in accordance with the velocities induced there by the source sheet.
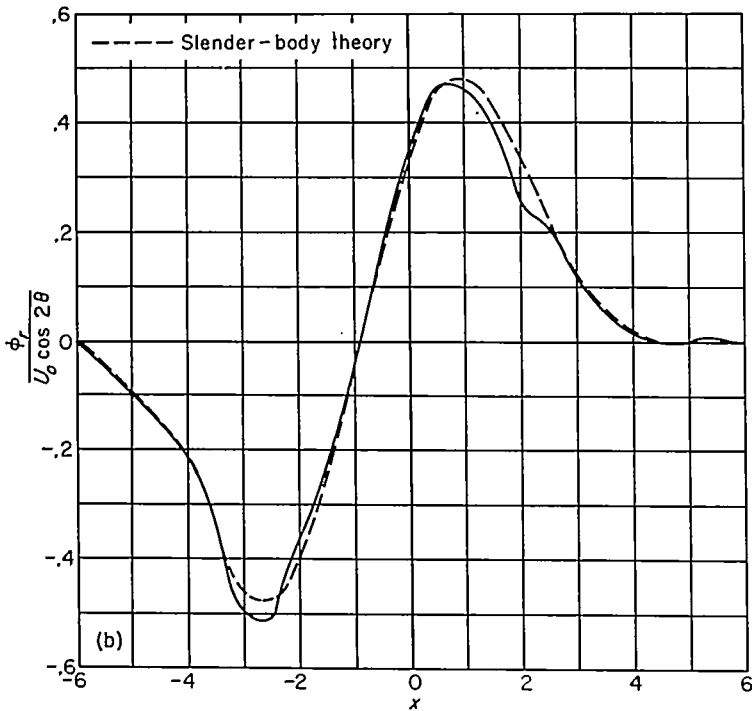
(b) Radial velocities induced by second-order multipoles.

FIGURE 25.—Continued.
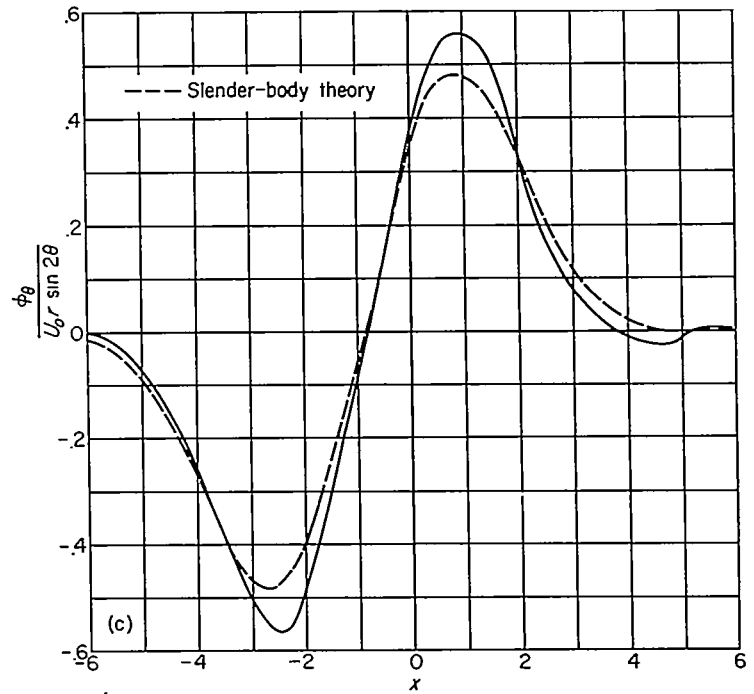
(c) Tangential velocities induced by second-order multipoles.

FIGURE 25.—Concluded.

Obviously, from this viewpoint, a considerable reduction in drag can be brought about merely by eliminating the bulge, thereby making the body a circular cylinder throughout. Mathematically, such a procedure amounts to using a certain set [9] of cancellation multipoles along the x axis behind the point $-L_o$, and, if the drag of this resulting combination were used as a reference, the gains shown in figure 24 would be diminished.

An approximate way to estimate the drag of a wing mounted on a circular cylinder is illustrated in figure 27 and consists merely of subtracting from the wing source sheet those sources blanketed by the body. Using the subscripts 1, 2, and 3 to designate the wave drags of the individual wings as indicated in figure 27, Jones (ref. 15) has shown that if wing 1 is an elliptic wing with a biconvex section and wing 2 lies entirely within the plan form of wing 1, then

$$D_3 = D_1\left(1 + \frac{2V_2}{V_1}\right) + D_2 \qquad (64)$$

where V_2 and V_1 are the volumes of wings 1 and 2, respectively.

For a supersonic Mach number, D_2 is closely approximated by the wave drag of a rectangular wing having the same section and aspect ratio. If A_2, $4Ra$, and τ_2 are, respectively, the aspect ratio, plan-form area, and thickness ratio of the rectangular wing, its drag can be expressed in the form

$$\frac{\beta D_2}{q\tau_2^2} = 4RaN_2 \qquad (65)$$

where

$$N_2 = \begin{cases} \dfrac{16}{\pi}\beta A_2\left[\dfrac{2}{3}\dfrac{\sin^{-1}\beta A_2}{\beta A_2} - \dfrac{\sqrt{1-\beta^2 A_2^2}}{6} + \right. \\ \qquad \left.\left(1 - \dfrac{\beta^2 A_2^2}{6}\right)\cosh^{-1}\dfrac{1}{\beta A_2}\right], \quad \beta A_2 \leq 1 \\[2em] \dfrac{16}{3} \qquad\qquad\qquad\qquad , \quad \beta A_2 \geq 1 \end{cases} \qquad (66)$$

FIGURE 26.—Wing and stream tube simulated by planar sheet of sources.

[9] The exact evaluation of multipole distributions necessary to simulate a circular cylinder for the entire body length has been studied in reference 14.

Wings

Equivalent wing-body combinations
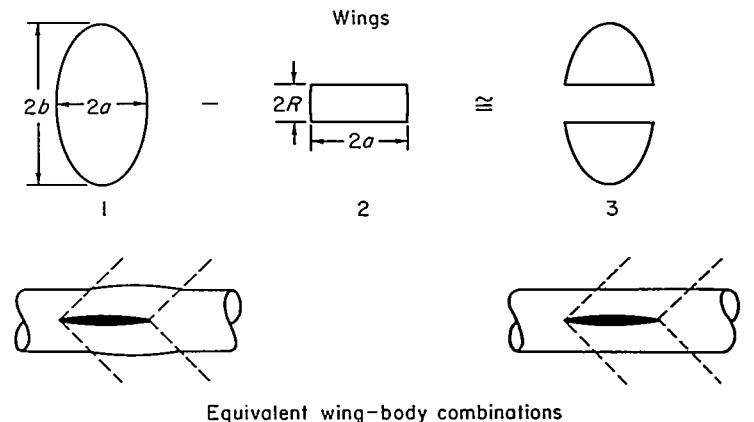
FIGURE 27.—Method of approximating wing mounted on a cylinder

Further, if A_1 is the aspect ratio of the elliptic wing, one can show—see figure 27 and equation (52)—

$$\beta A_2 = \frac{\pi}{4}\left(\frac{R}{b}\right)\beta A_1 \tag{67}$$

The drag of the elliptic wing follows from equation (55) and can be written

$$\frac{\beta D_1}{q\tau_2^2} = 4abN_1 \tag{68}$$

where

$$N_1 = \pi \frac{1 + 2\left(\frac{4}{\pi\beta A_1}\right)^2}{\left[1 + \left(\frac{4}{\pi\beta A_1}\right)^2\right]^{3/2}} \tag{69}$$

Finally, therefore, equation (64) can be put in the form

$$\frac{D_3}{D_1} = \left[1 - \frac{32}{3\pi}\left(\frac{R}{b}\right)\right] + \frac{R}{b}\frac{N_2}{N_1} \tag{70}$$

and the ratio N_2/N_1 is a function of the parameters R/b and βA_1 only.

By means of equation (70), the dashed curves shown in figure 28—
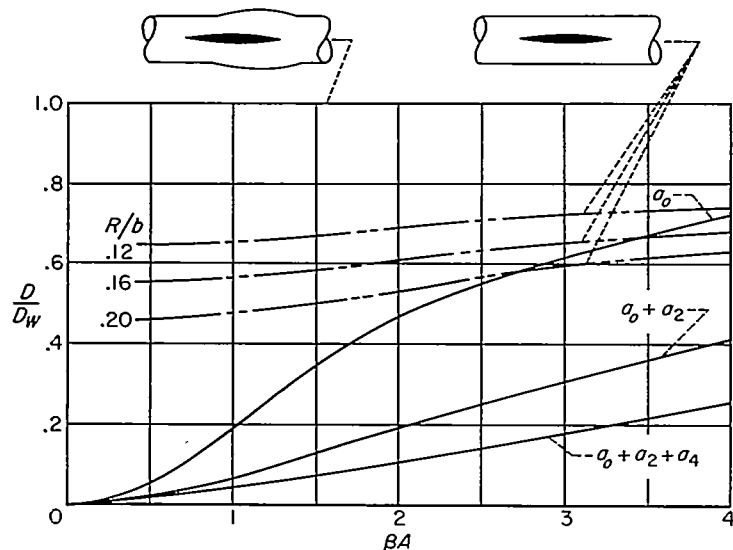
FIGURE 28.—Drag of various multipole distributions compared with drag of wing mounted on circular cylinder.

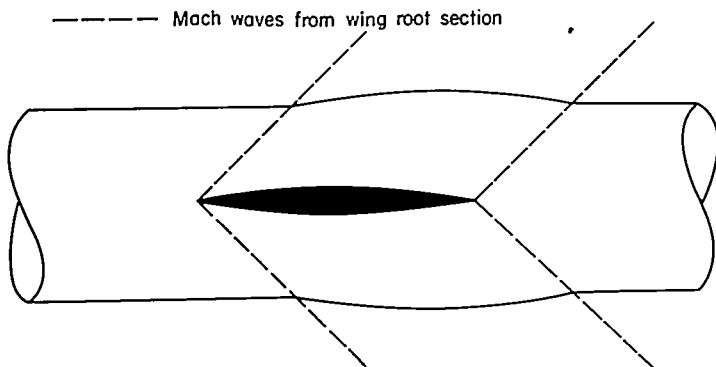representing approximately the wave drag of a wing mounted centrally on a circular cylinder—were calculated. Though considerable drag reduction is indicated by adding just those multipoles necessary to make the body cylindrical, it is apparent the total wave drag can be reduced further, for the range of parameters shown, by using only the first two optimum cancellation-multipole distributions, $\alpha_o(x)$ and $\alpha_2(x)$, given by equation (36).

Comparison with wing mounted on a basic body of revolution.—Figure 28 shows the effect on the wave drag of adding the optimum cancellation multipoles either to the wing alone or to the combination of an infinite circular cylinder and a centrally mounted wing. Estimates of their effect when added to a wing mounted on a basic body of revolution can also be carried out. In order to present these

estimates, however, the results of the following two theorems due to R. T. Jones (ref. 15) are needed.

1. Designate the closed body of revolution which, by slender-body theory, has a minimum drag for a fixed volume and length as a Sears-Haack body. Then the total wave drag of a Sears-Haack body and any other body of revolution or any centrally mounted thin wing which lie entirely within the Sears-Haack body's enclosing Mach forecone and aftercone is given by the equation

$$D = D_{SH}\left(1 + \frac{2V_2}{V_{SH}}\right) + D_2 \tag{71}$$

where:

D_{SH} wave drag of Sears-Haack body alone
D_2 wave drag of other body or (exposed) wing alone
V_{SH} volume of Sears-Haack body
V_2 volume of other body or (exposed) wing

2. Designate the body of revolution which, by slender-body theory, has a minimum drag for a fixed base diameter and length as a Kármán ogive. Then the total wave drag of a Kármán ogive and any other slender body of revolution or any centrally mounted thin wing which lie entirely within the ogive's enclosing Mach forecone and aftercone is given by the equation

$$D = D_K + D_2 \tag{72}$$

where:

D_K wave drag of Kármán ogive alone
D_2 wave drag of other body or (exposed) wing alone

In order that the theoretical results could be tested by wind-tunnel experiments, a basic body of revolution having a finite base area was chosen. Such a body can be simulated by a combination of the source distributions which produce,[10] separately, the Sears-Haack body and the Kármán ogive. Thus, if $2l$ is to be the body length, the line of sources

$$\frac{a_o(x)}{U_o} = \frac{2}{\pi l^3}\left(V_K - 4V_{SH}\frac{x}{l}\right)\sqrt{l^2 - x^2} \tag{73}$$

simulates (by slender-body theory) a body of revolution having a total volume V equal to $V_{SH} + V_K$, a cross-sectional area given by

$$S(x) = \frac{V_K}{\pi l^3}\left[x\sqrt{l^2 - x^2} + l^2\left(\frac{\pi}{2} + \sin^{-1}\frac{x}{l}\right)\right] +$$
$$\frac{8V_{SH}}{3\pi l^4}(l^2 - x^2)^{3/2}, \qquad -l \leq x \leq l \tag{74}$$

and a base area $S(l)$ equal to V_K/l.

The wave drag of a wing mounted on this basic, unmodified body will now be calculated. Just as was the case in studying the wing attached to an infinite cylinder, the assumption is made that the wave drag of this combination is the same as the wave drag on the configuration simulated by superimposing the singularity distributions which create sepa-

---

[10] The source distributions simulate the Sears-Haack body and the Kármán ogive only when slender-body theory is used to calculate the body shapes. If linearized theory is used instead, the body shape will, of course, be somewhat different. However, the subsequent results and conclusions are by no means limited by the assumptions pertaining to slender-body theory. The latter theory is used only to obtain an estimate of the body volumes or to study cases for which it gives results that are not significantly different from those given by linearized theory.

rately the exposed wing panels and the body of revolution. With this assumption, the wave drag can be written explicitly in terms of the wing and body geometry by applying equations (71) and (72). Hence,

$$D=D_K+D_{SH}\left(1+\frac{2V_3}{V_{SH}}\right)+D_3 \tag{75}$$

where D_3 is the drag of the exposed wing panels alone, given by equation (70) and shown for various values of R/b in figure 28, and V_3 is their volume (see fig. 27)

$$V_3=tab\left(\frac{\pi}{2}-\frac{8}{3}\frac{R}{b}\right) \tag{76}$$

Since D_K and D_{SH}, the wave drags of a Kármán ogive and a Sears-Haack body flying alone, are well known to be

$$\left.\begin{aligned}D_K&=\frac{q}{\pi}\frac{V_K^2}{l^4}\\[2mm]D_{SH}&=\frac{8q}{\pi}\frac{V_{SH}}{l^4}\end{aligned}\right\} \tag{77}$$

the wave drag coefficient of the unmodified combination, based on the complete wing area πab, can be expressed as

$$\frac{D}{q\pi ab}=C_D=\frac{V_K^2+8V_{SH}^2}{\pi^2l^4ab}+\frac{16tV_{SH}}{\pi^2l^4}\left(\frac{\pi}{2}-\frac{8}{3}\frac{R}{b}\right)+$$

$$\frac{t^2N_1}{\pi a^2\beta}\left[\left(1-\frac{32}{3\pi}\frac{R}{b}\right)+\frac{R}{b}\frac{N_2}{N_1}\right] \tag{78}$$

where N_1 and N_2 are defined in terms of Mach number and wing-body geometry in equations (66) and (69). An example of the variation of C_D with Mach number for the particular combination shown in figure 29 (R/b was set equal to 0.181) is given by the dashed line in figure 30.

It is now possible to find how much the drag of this unmodified combination can be reduced by means of the optimum cancellation-multipole distributions used to derive the results shown in figure 24. Again applying equations (71) and (72), one can show

$$D=D_K+D_{SH}\left(1+\frac{2V_4}{V_{SH}}\right)+D_4 \tag{79}$$
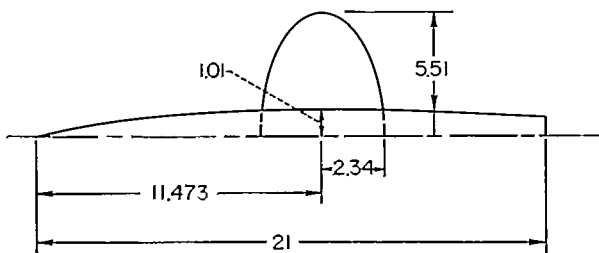
Maximum thickness of wing along center line, t =0.234

Total volume of body = 44.60
V_{SH} = 31.72
V_K = 12.88

FIGURE 29.—Dimensions of wing-body combination analyzed.
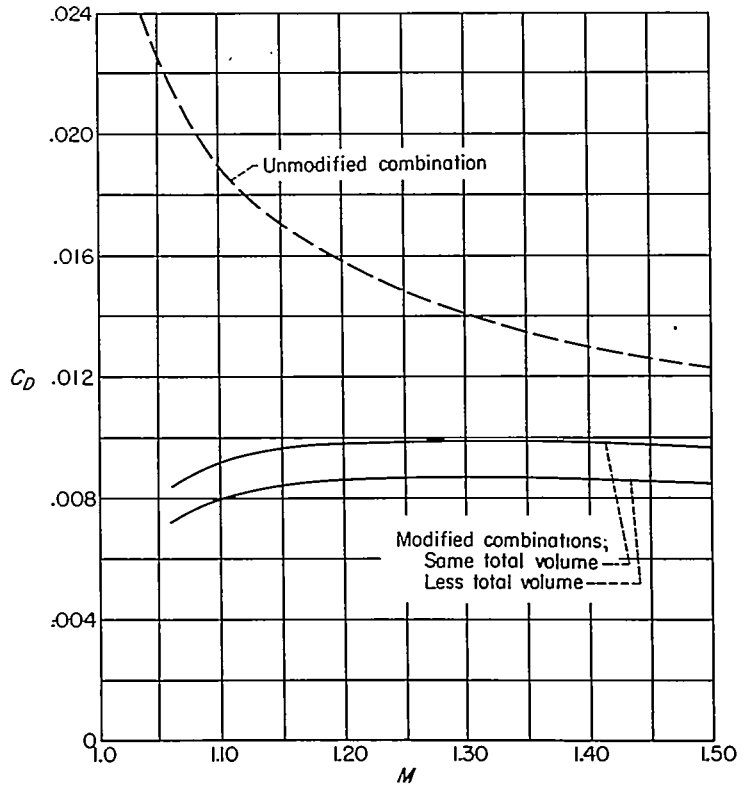
FIGURE 30.—Drag variation for modified and unmodified wing-body combinations.

where V_4 is the total volume and D_4 the total wave drag pertaining to the wing (now the complete wing including the portion blanketed by the body) and the multipoles. However, within the accuracy of the approximation—being, in fact, exact within slender-body theory, see Appendix B—the volume added by the wing is subtracted from the basic body by the optimum cancellation-source distribution so that V_4 is zero. Further, if N_4 is the value of D/D_w read from figure 24 for a specific value of βA_1 and a specific number of multipole types, one can readily show

$$D_4=\frac{t^2bq}{\beta a}N_1N_4 \tag{80}$$

where N_1 is defined in equation (69). Hence, the drag of the unmodified combination can be reduced to either

$$\frac{D}{q\pi ab}=C_D=\frac{1}{\pi^2abl^4}\left\{V_K^2+8\left[V_{SH}+tab\left(\frac{\pi}{2}-\frac{8}{3}\frac{R}{b}\right)\right]^2\right\}+$$

$$\frac{t^2}{\pi a^2\beta}N_1N_4 \tag{81}$$

if the same total volume is maintained (maintained, as is obvious from an inspection of the equation, by increasing the value of the Sears-Haack portion of the basic body an amount equal to the volume of the exposed wing) or to

$$C_D=\frac{1}{\pi^2abl^4}(V_K^2+8V_{SH}^2)+\frac{t^2}{\pi a^2\beta}N_1N_4 \tag{82}$$

if the volume of the fuselage is reduced by an amount equal to the wing volume.
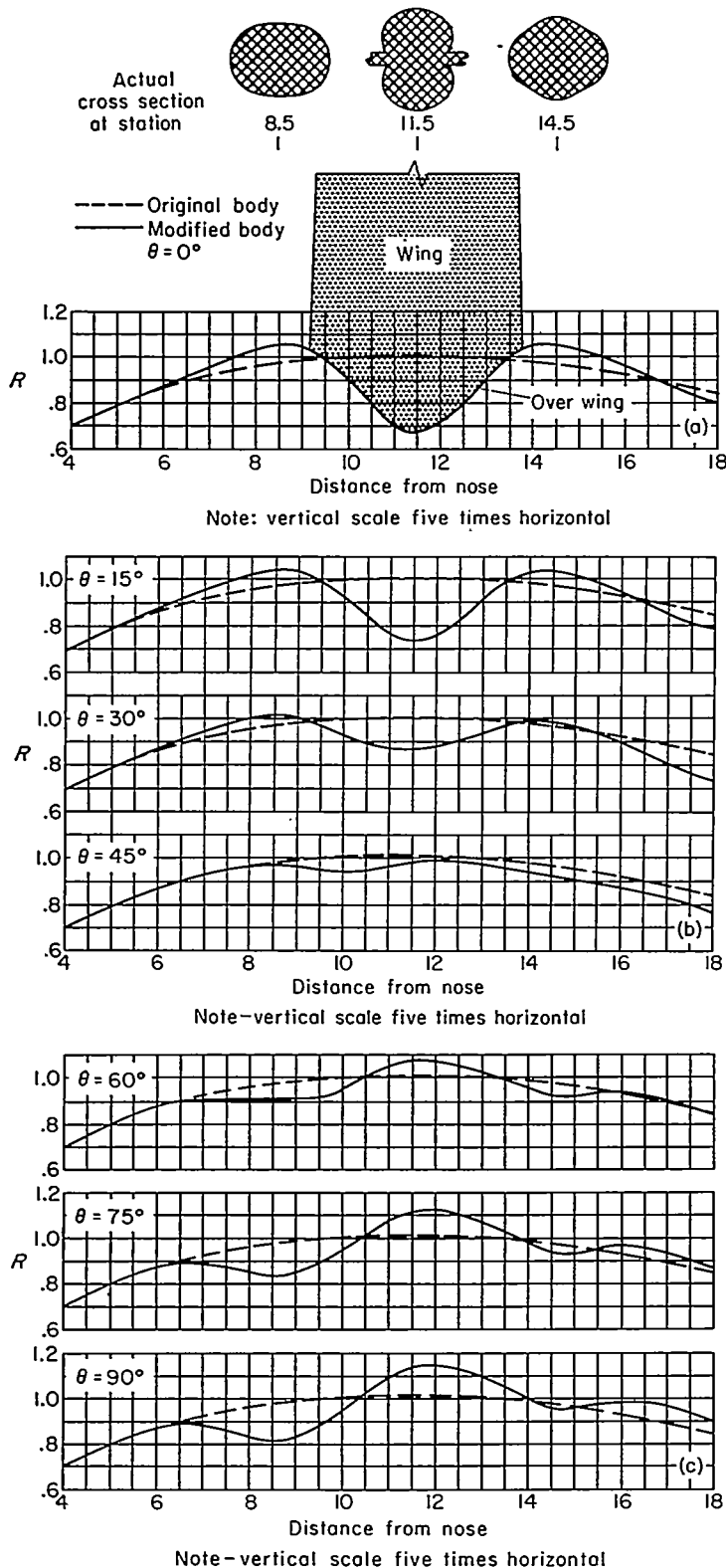
FIGURE 31.—Body shape having favorable interference wave drag at $M=1.41$ when combined with elliptic wing.

The results expressed by equations (80) and (81), when applied to the first two optimum cancellation-multipole distributions, are shown for the geometrical parameters presented in figure 29 by the solid curves in figure 30. The value of R/b used for the solid curves was 0.161 instead of the 0.181 value used to calculate the dashed curve. The smaller value was used since the modified body is drawn in along the

sides by the cancellation multipoles (see fig. 31), decreasing the average body radius in the wing region from about 1.00 to about 0.89. One must be careful to notice that the solid curves represent minimum (relative to the special method being discussed) values which can be obtained by a specific design at a specific Mach number and do not represent the variation of wave drag with Mach number for any given combination.

THE BODY SHAPE—FIRST CALCULATION

The final step in studying the effect of the optimum cancellation multipoles, defined in equation (36), is to find the distorted body shape which they produce in combination with the wing and a basic body. The decision was made to calculate a body shape which would be optimum at a Mach number equal to $\sqrt{2}$. The details of the wing and body geometry are given in figure 29 and the basic body parameters V_K and V_S were interpreted in terms of source strength by equation (73).

It was apparent from the results of figure 25 that, for the values of r_e and b given by figure 29, the velocity field induced by the first two optimum multipole distributions can be calculated with good accuracy using slender-body theory. Combining the values of φ_r and φ_θ so calculated with those induced by the wing, given by equation (56), and those induced by the basic body, using also slender-body theory to interpret equation (73), one can find the body shape by solving the two simultaneous nonlinear differential equations presented as equations (43). These were solved numerically by the method outlined in Appendix D and the results were, unfortunately, unrealistic. Figure 32 shows an example of a streamline close to the $\theta=0$ plane and the crossing of such streamlines obviously invalidates the solution.

BODY SHAPE—SECOND CALCULATION

The failure observed in the first calculation has a simple enough interpretation. For the chosen wing the basic body was too small in diameter at the wing-body juncture to permit the use of the first two cancellation multipoles in their entirety.

Several avenues of approach are yet available. One could, for example, maintain the same wing and basic body but reduce the Mach number, one could start with a larger basic body, or one could lower the thickness ratio or aspect ratio of the wing, thus diminishing the strength of the cancellation multipoles. All of these, however, are modifications of the basic conditions or basic restraints and as soon as such
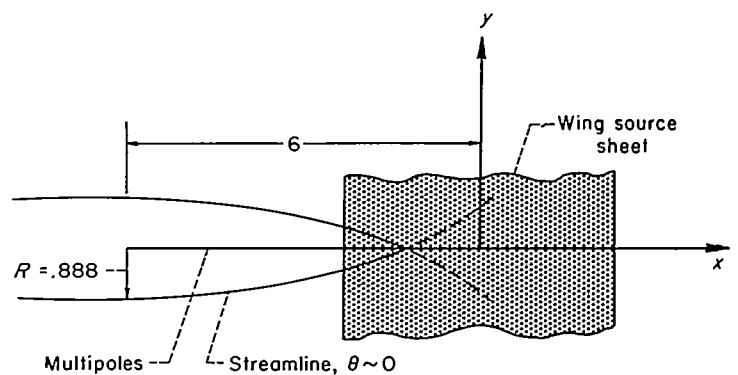
FIGURE 32.—Streamline when starting body radius is too small.

restrictions are abandoned it must be remarked that no matter how low the wave drag of a set of nonlifting, volume-enclosing surfaces has been made, another arrangement of the same volume within a finite space will give a lower value, unless, of course, the wave drag of the first arrangement is already zero. Therefore, instead of modifying any of the initial restraints, consider the following alternative:

How much can the drag be reduced by using only a portion of the first two cancellation multipoles so that a real body would still be simulated?

In order to answer the above question, examine briefly the first calculation. Notice, from figure 25, that the cause of the body collapse is attributable to the large values of φ_r and φ_θ induced by the second-order cancellation multipoles, $\alpha_2(x)$. Hence, let $\alpha_o(x)$ be maintained at its full value and reductions permitted only in the magnitude of $\alpha_2(x)$. To carry out such a procedure efficiently, one must be able to determine the effect of a given variation of $\alpha_2(x)$ on the body shape. Fortunately, Graham, in reference 16, has developed a method by means of which the relation between $\alpha_2(x)$ and body shape can be quickly estimated. Graham has shown if

1. a rectilinear distribution of second-order multipoles of strength $\alpha_2(x)$ is placed along the x axis (see fig. 33) in a supersonic stream $(M=\sqrt{2})$

2. slender-body theory is used to evaluate φ_r and φ_θ,

3. $R=R_c$ is the radius of a circularly cylindrical tube for $-L_o>x>-\infty$,

4. $F^*(x)=\dfrac{4}{\pi U_o R_c{}^4}\displaystyle\int_{-L_o}^x \alpha_2(x_2)dx_2$

then

$$R=R_c\left\{\frac{1+2F^*(x)\cos 2\theta+\sqrt{1+4F^*(x)\cos 2\theta+4[F^*(x)]^2}}{2}\right\}^{1/4}$$

(83)

is the continuation of the stream tube for $x>-L_o$.

Since the initial strengths of the cancellation multipoles are negative, $F^*(x)$ is negative and the critical value of R
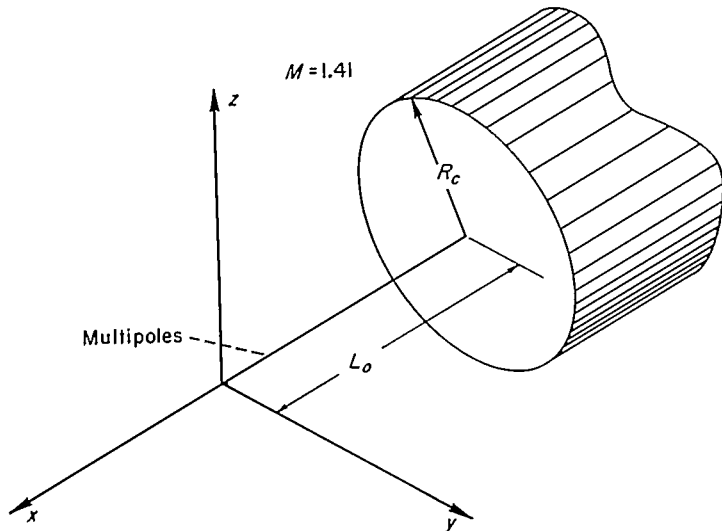
FIGURE 33.—Definition of parameters used to study effect of second-order multipoles on fuselage shape.

435875—57——48
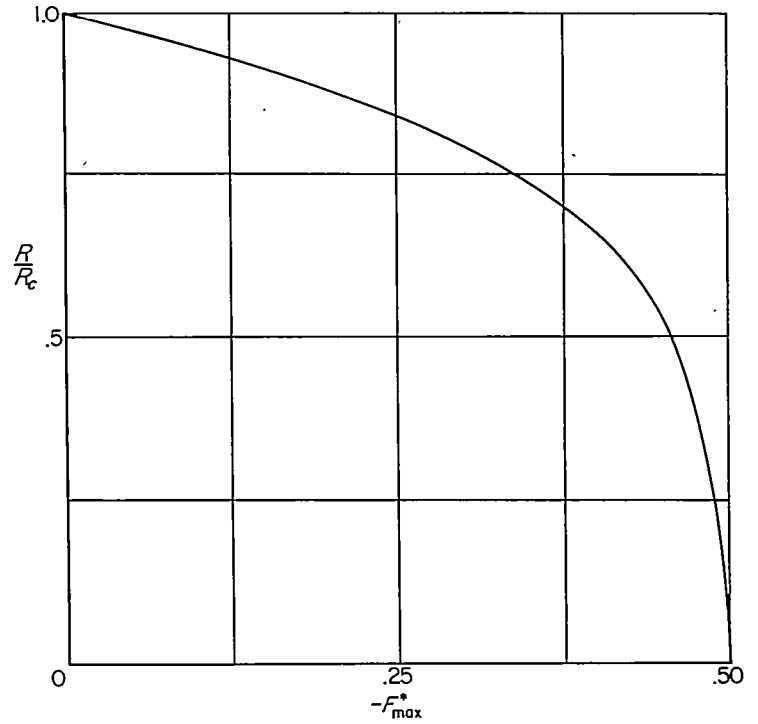
FIGURE 34.—Variation of R/R_c with $-F^*_{max}$.

occurs along the plane $\theta=0$ or π. The variation of R/R_c with F^*_{max} is given in figure 34 from which one can see that the maximum value of $|F^*|$ must be less than 0.5 if the simulated stream tube behind the plane $x=-L_o$ is to be real.

The problem can now be continued, using Graham's result as a guide, by assuming the critical body radius in the more complicated source and multipole arrangement is principally determined by $F^*(0)$—the parameter governing the body indentation at the center of the cutout and at the wing-body juncture. In the first place, since there is no interference between different orders of multipoles, it is necessary to consider only the drag produced by the second-order multipole. Appendix E presents a method for finding the optimum distribution of the second-order cancellation multipoles for a given wing and a fixed value of $F^*(0)$. The resulting wave drag is given in equation (E11). At a Mach number equal to $\sqrt{2}$ and for the basic wing and body parameters presented in figure 29, $F_w^*(0)$ (defined by eq. (E8)) equals -2.90 and the reduction in $\overline{D}_2/qS$, the amount of drag caused by the wing second-order multipoles alone—see equation (62) and figure 24—is shown in figure 35 for a range of $F^*(0)$. Variations on the strength of various combinations of second-order multipoles are shown in figure 36. It is important to notice that for a given percentage reduction in the maximum strength of the multipoles the resulting percentage reduction in $\overline{D}_2$ is much larger.

The strengths of $\alpha_2(x)$ shown in figure 36 must now be combined with the zero-order multipoles and wing source sheet, and the combined velocity field used to calculate the shape of the new body. Using again slender-body theory to evaluate the velocity field induced by the multipoles and the numerical methods given in Appendix D to compute the streamlines, one finds, by restricting the distribution and strength of the second-order cancellation multipoles to their

FIGURE 35.—Reduction in drag caused by second-order multipoles.

FIGURE 36.—Variation of second-order multipoles for several values of $F^*(0)$.

FIGURE 37.—Drag of unmodified and modified combinations with real body shapes.

resent an estimate of the amount the wave drag of an elliptic wing mounted on a basic body of revolution can be reduced by realistic body distortions—are shown in figure 37.

DISCUSSION OF RESULTS

It is possible to gain some insight into the reasons for the various body distortions shown in figure 31 by inspecting, in another light, the body shape first calculated. Consider first the elliptic wing at the top of figure 38. The air over the forward part of this wing, when it is alone in a supersonic stream, is compressed (mathematically, the sign of φ_x is negative), the compression being greatest near the leading edge. On the other hand, the air over the after portion of the wing is undergoing an expansion, the magnitude of which is greatest near the trailing edge. Consider now, in combination with this wing, a body which is to have a shape providing favorable interference. It is apparent that the body should cast expansion waves over the forward portion of the wing, destroying the compression there, and absorb the expansion waves coming from the wing afterportion. Or in another light, the positive pressure on the forward region of the wing (one can use the equation $C_p = (p - p_o)/q = -2\varphi_x/U_o$ for the pressure coefficient) should be reduced as far as possible by a wave shed from the body and having large negative pressures where it comes in contact with the wing forward region.

Since waves in a supersonic flow field are fundamentally associated with the slope of the disturbing surface, the aforementioned favorable interference fields would be created by a body having, longitudinally along its surface, slopes such as those shown in the lower part of figure 38. This is exactly what the solution obtained from the calculation of the

optimum values corresponding to the restraint [11] $F^*(0) = -0.6$, that a real as well as reasonable body shape results. The details of this shape are presented in figure 31 and their general interpretation is discussed in the next section. Finally, using the value $F^*(0) = -0.6$, the drag curves shown in figure 30 were reinterpreted, and the results—which rep-

[11] Figure 34 gives 0.5 as the maximum permissible value of $-F^*(x)$. However, that value is based on a distribution of $\alpha_2(x)$ alone, and in our more general case the added velocity field caused by the presence of the other singularities permits the larger value.

FIGURE 38.—Regions of expansion and compression on wing with unmodified and modified fuselage.

first body shape tried to establish since the fuselage near the plane of the wing (the portion most strongly affecting and being affected by the pressures on the wing) and ahead of the wing chordwise center line was distorted in a manner that caused an expansion across the wing entire forward portion. The difficulty arose because the fuselage was not wide enough

to provide the longitudinal extent of favorable slopes necessary to create the positive pressure called for by the wing forward compression region, and the body streamline near the wing root, following a path such as that shown by the line in figure 38, crossed the body center line before it reached the wing chordwise center.

Consider now the second body calculated in the previous section. In this case an additional restraint was imposed which, effectively, fixed the maximum body indentation. Subject to such a condition, an optimum interference field was discovered. If the resulting fuselage shape is inspected near the plane of the wing, surface slopes are found similar to those shown in figure 39. The following discussion is intended to show that, from a physical viewpoint, this arrangement is reasonable.

Most of the wing pressure drag occurs on the wing inboard portions. Hence, for a fixed maximum fuselage indentation, it is beneficial, from an over-all point of view, to create initially a compression wave, which increases the pressure drag on the forward portion of the wing tip but provides a
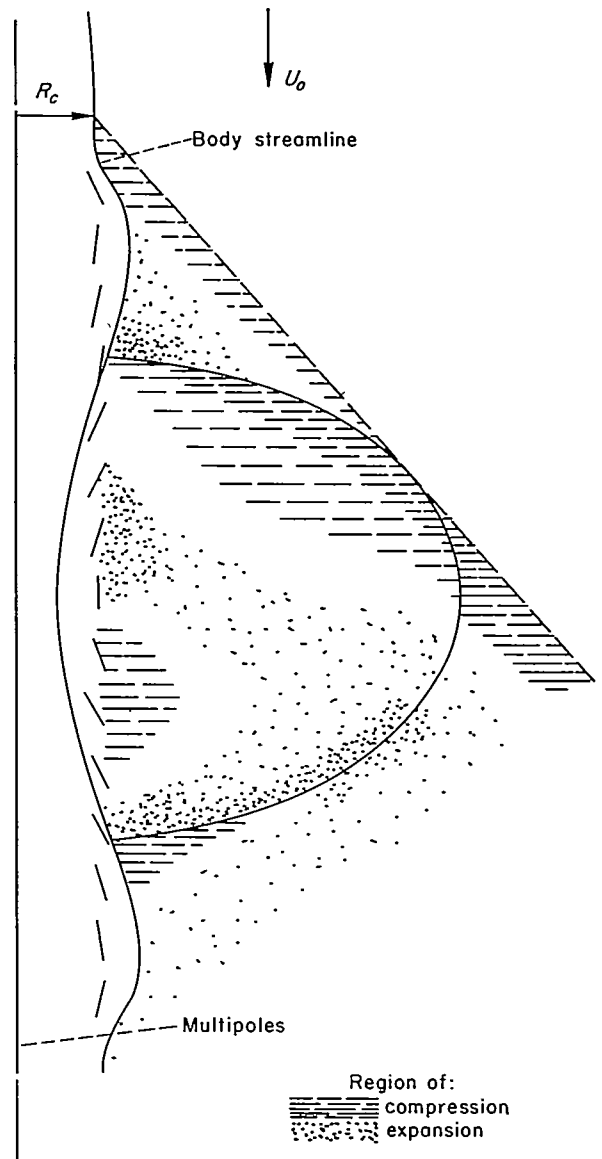
FIGURE 39.—Regions of expansion and compression on wing with fuselage distortion shown.

succeeding extent of fuselage having slopes that generate a strong expansion wave over the forward portion of the wing inboard section. Similarly, the final portion of the body is forced to have a region of unfavorable interferences where the expansion waves from the wing tips combine with body expansion waves to increase the local drag (i. e., increase the local suction pressure) in order that the over-all interference effects are as beneficial, under the given restraints, as possible. This arrangement (i. e., unfavorable interference near the wing tip and favorable interference near the wing root) is given further support by the attenuation property inherent in three-dimensional waves. Thus the pressures induced by the body on the wing tips are not as strong, for a given generating surface slope, as those induced on the inner portion of the wing, simply because the tips are farther from the disturbing surface.

Although these considerations are somewhat oversimplified (the shape of the upper part of the body has been completely ignored in estimating the effect of the waves), the longitudinal variation of surface slopes near the plane of the wing and the resulting body streamlines there are, from a physical point of view, reasonable.

In order to support the above conclusions, the source and multipole distributions simulating the final modified body shown in figure 31 were used to calculate (see Appendix C) u/U_o in the plane of the wing near the root section. The values of u/U_o induced by the wing sources along these sections were assumed to be the same as those induced by a two-dimensional biconvex section having the same local chord; that is, tip effects were neglected. These values for body and wing were added and the resulting pressure distribution, shown in figure 40 ($C_p = -2\ u/U_o$), were obtained.
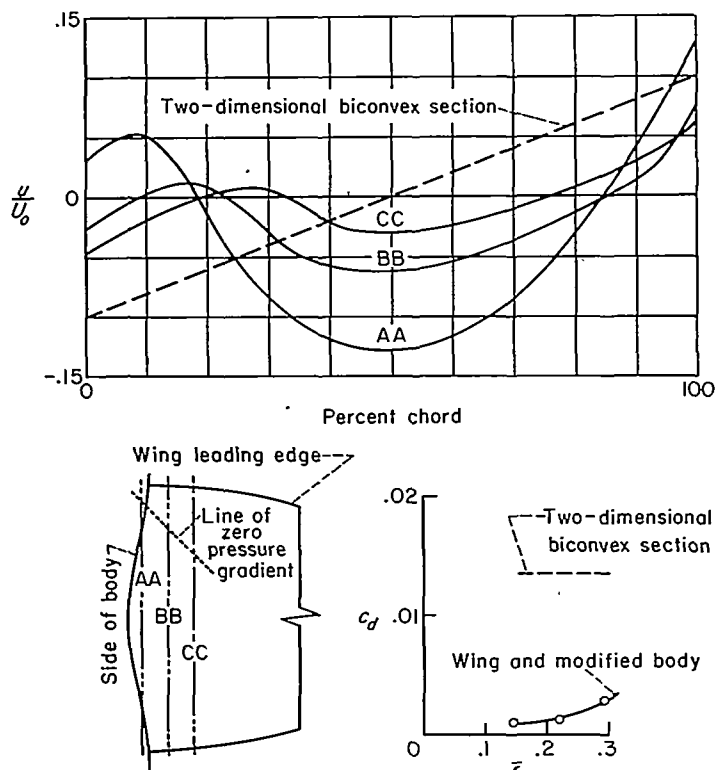
FIGURE 40.—Variation of pressure and section-drag coefficient on sections indicated.

The results are similar to the estimates presented in figure 39. The large drag saving near the root section is illustrated in figure 40 by the graph showing the low values of section drag coefficient along the inner portion of the wing.

Another important characteristic of wing-body combinations designed to have low wave drag is also illustrated in figure 40. As shown in the graph of u/U_o, over the surface of a two-dimensional biconvex section the air is everywhere accelerating in the streamwise direction. In studies concerning the effects of viscosity on the fluid flow and, in particular, studies concerning the boundary layer, this positive fluid acceleration is referred to as a favorable pressure gradient. If the flow is laminar in the vicinity of the leading edge of a smooth wing and the pressure gradient is everywhere favorable, the flow tends to remain laminar and unseparated over most of the wing chord. Notice that the modified wing-body combination has a line of zero pressure gradient extending along a Mach line downstream from a point near the body and wing leading-edge juncture. Immediately behind this line the pressure gradient is unfavorable which gives rise to the possibility of flow separation or, at least, transition from laminar to turbulent flow there.

COMPARISON WITH EXPERIMENT

The modified wing-body combination shown in figure 31 was tested in the Ames 2- by 2-foot transonic wind tunnel. The Reynolds number of the test, based on the mean aerodynamic chord, was approximately 1.5×10^6. This combination had an exposed wing volume of 3.44 cubic inches and a body volume equal to 44.60 cubic inches, for a total volume of 48.04 cubic inches. As a control, an unmodified combination composed of the same elliptic wing mounted on a body of revolution (the area distribution of which was determined from equation (74) with $l = 10.5$, $V_K = 12.88$, and $V_{SH} = 29.02$ cubic inches) was tested. The exposed wing area in the unmodified combination was 3.32 cubic inches and the body volume was 41.90 cubic inches, for a total volume of 45.22 cubic inches. Thus, the unmodified combination had the same body length as the modified one but less volume.

The wave drag at $M = 1.41$ of the combination shown in figure 31 has already been calculated and presented in figure 37 by the curve pertaining to real body shapes. By use, in equation (78), of the values of V_K and V_{SH} mentioned above and a value of 0.176 for R/b, the wave drag for the unmodified body was calculated throughout a supersonic Mach number range. The theoretical results obtained for body configurations are shown by the dashed curves in figure 41.

The wind-tunnel results for the total drag on both configurations are shown in figure 42 for $0.6 \le M \le 1.4$. Notice that three groups of data are shown. The lower one represents the unmodified body alone, the middle one represents the modified and unmodified combinations with no fixed transition, and the upper one represents both combinations with transition fixed along the leading edge. The models tested with natural transition did not show the predicted drag reduction. As was pointed out in the discussion of figure 40, however, the adverse pressure gradients on the modified model could be inducing transition in the vicinity of
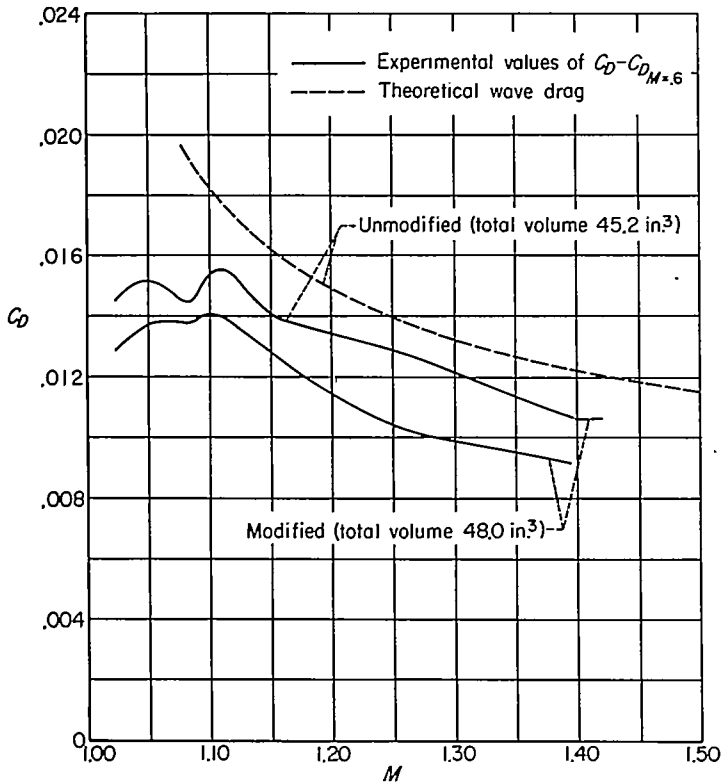
FIGURE 41.—Variation with Mach number of theoretically and experimentally determined drag coefficient.

FIGURE 42.—Experimental values for drag coefficient.

the 45° line behind the juncture of the wing leading edge with the fuselage. This, in turn, would cause the wing of the modified model to have a larger area covered with a turbulent boundary layer and, hence, cause the drag of the model to increase. In order to separate the potential and viscous effects, the transition-fixed tests were made. If the experimental wave drag is taken to be the difference between the drag at a supersonic Mach number and the drag. at

$M=0.6$, the resulting values of experimental wave drag are as shown in figure 41.

Figure 41 shows that the experimental reduction in wave drag brought about by the modification agrees with that predicted by theory. Both theory and experiment show a reduction of about 0.0015 in the drag coefficient at the design Mach number (1.41), and the experiment further shows an average reduction of 0.0020 over the Mach number range $1.2<M<1.4$. A further study of figure 42 shows that the difference between the experimental and theoretical wave drags shown in figure 41 for the wing-body combinations is nearly the same as the difference between experiment and theory for the body alone.

AMES AERONAUTICAL LABORATORY
  NATIONAL ADVISORY COMMITTEE FOR AERONAUTICS
    MOFFETT FIELD, CALIF., *May 16, 1956*

APPENDIX A

DERIVATION OF THE OPERATIONAL FORM OF THE WAVE EQUATION

For convenience, take the normalized form of the wave equation in Cartesian coordinates, thus

$$\frac{\partial^2 \varphi}{dx^2} - \frac{\partial^2 \varphi}{dy^2} - \frac{\partial^2 \varphi}{\partial z^2} = 0 \tag{A1}$$

and define the Laplace transform of $\varphi(x,y,z)$ by

$$\bar{\varphi}(s,y,z) = \int_0^\infty e^{-sx} \varphi(x,y,z)\, dx \tag{A2}$$

Now if $x = f(y,z)$ is the equation of the foremost Mach cone or Mach cone envelope and $f(y,z) \geq 0$, it is apparent

$$\frac{\partial^2 \bar{\varphi}}{\partial y^2} = \frac{\partial^2}{\partial y^2} \int_f^\infty \varphi(x,y,z) e^{-sx} dx = \int_f^\infty e^{-sx} \frac{\partial^2 \varphi}{\partial y^2} dx - \frac{\partial f}{\partial y} e^{-sf} \left(\frac{\partial \varphi}{\partial y}\right)_{x=f} \tag{A3}$$

since $(\varphi)_{x=f}$ is, but $\left(\dfrac{\partial \varphi}{\partial y}\right)_{x=f}$ is not, necessarily zero. From equation (A3) we see

$$\int_0^\infty e^{-sx} \frac{\partial^2 \varphi}{\partial y^2} dx = \frac{\partial^2 \bar{\varphi}}{\partial y^2} + \frac{\partial f}{\partial y} e^{-sf}\left(\frac{\partial \varphi}{\partial y}\right)_{x=f} \tag{A4}$$

$$\int_0^\infty e^{-sx} \frac{\partial^2 \varphi}{\partial z^2} dx = \frac{\partial^2 \bar{\varphi}}{\partial z^2} + \frac{\partial f}{\partial z} e^{-sf}\left(\frac{\partial \varphi}{\partial z}\right)_{x=f} \tag{A5}$$

Further, integrating by parts gives

$$\int_0^\infty e^{-sx} \frac{\partial^2 \varphi}{\partial x^2} dx = s^2 \bar{\varphi} - e^{-sf}\left(\frac{\partial \varphi}{\partial x}\right)_{x=f} \tag{A6}$$

Hence,

$$\int_0^\infty e^{-sx}\left(\frac{\partial^2 \varphi}{\partial x^2} - \frac{\partial^2 \varphi}{\partial y^2} - \frac{\partial^2 \varphi}{\partial z^2}\right) dx = s^2 \bar{\varphi} - \frac{\partial^2 \bar{\varphi}}{\partial y^2} - \frac{\partial^2 \bar{\varphi}}{\partial z^2} - e^{-sf}\left(\frac{\partial \varphi}{\partial x} + \frac{\partial \varphi}{\partial y}\frac{\partial f}{\partial y} + \frac{\partial \varphi}{\partial z}\frac{\partial f}{\partial z}\right)_{x=f} \tag{A7}$$

The last term on the right is the directional derivative of the perturbation potential along the surface $x = f(y,z)$. This is, of course, along the so-called conormal. Since φ is a constant on the forward envelope, its gradient along the envelope is zero and

$$\int_0^\infty e^{-sx}\left(\frac{\partial^2 \varphi}{\partial x^2} - \frac{\partial^2 \varphi}{\partial y^2} - \frac{\partial^2 \varphi}{\partial z^2}\right) dx = s^2 \bar{\varphi} - \frac{\partial^2 \bar{\varphi}}{\partial y^2} - \frac{\partial^2 \bar{\varphi}}{\partial z^2} = 0 \tag{A8}$$

APPENDIX B

ON THE VOLUME OF BODIES CALCULATED USING SLENDER-BODY THEORY

The following proof shows that in a rectilinear distribution of singularities, only the sources contribute to the total cross-sectional area of the simulated body and, hence, to its volume.

According to slender-body theory, the velocities induced in the field by distributions of multipoles along the x axis can be written

$$\varphi_{n_r} = \begin{cases} \dfrac{a_o(x)}{2\pi r}, & n=0 \\[2ex] \dfrac{(-2)^n n!\, a_n(x) \cos n\theta}{4\pi r^{n+1}}, & n>0 \end{cases} \tag{B1a}$$

$$\frac{1}{r}\varphi_{n_\theta} = \frac{(-2)^n n!\, a_n(x) \sin n\theta}{4\pi r^{n+1}} \tag{B1b}$$

Further, we have derived—see equation (41)—neglecting only second-order effects, the equation representing the boundary condition for the body, thus

$$U_o \frac{\partial R}{\partial x} = \left(\varphi_r - \frac{\varphi_\theta}{r^2}\frac{\partial R}{\partial \theta}\right)_{r=R(x,\theta)} \tag{B2}$$

Combine equations (B1) and (B2)

$$2\pi U_o R \frac{\partial R}{\partial x} = a_o(x) + \sum_1^\infty (-2)^n n!\, a_n(x)\left(\frac{\cos n\theta}{R^n} - \frac{\sin n\theta}{R^{n+1}}\frac{\partial R}{\partial \theta}\right)$$

multiply by $d\theta$, and integrate

$$2\pi U_o \frac{\partial}{\partial x}\int_0^{2\pi} \frac{R^2}{2} d\theta = 2\pi a_o(x) + \sum_1^\infty (-2)^n n!\, a_n(x) \int_0^{2\pi}\left(\frac{R \cos n\theta - \sin n\theta\, \frac{\partial R}{\partial \theta}}{R^{n+1}}\right) d\theta$$

or

$$2\pi U_o \frac{\partial}{\partial x} S(x) = 2\pi a_o(x) + \sum_1^\infty (-2)^n (n-1)!\, a_n(x) \int_0^{2\pi} \frac{d}{d\theta}\left(\frac{\sin n\theta}{R^n}\right) d\theta \tag{B3}$$

Since the integrand in equation (B3) is a periodic function in θ, we have

$$\frac{\partial S}{\partial x} = \frac{a_o(x)}{U_o} \tag{B4}$$

which shows the simulated-body normal cross-sectional area to be dependent only on the source strength. Further, the total volume is given by

$$V = \int_{-l}^{l'} S(x)\, dx = \int_{-l}^{l'} (l'-x) S'(x)\, dx + (l'+l)S(-l)$$

and when $S(l') = S(-l) = 0$, there results

$$V = -\frac{1}{U_o}\int_{-l}^{l'} x a_o(x)\, dx \tag{B5}$$

APPENDIX C

ON THE CALCULATION OF VELOCITIES INDUCED BY ARBITRARY SOURCE DISTRIBUTIONS

The potential and velocity fields represented by equations (18) and (19) are difficult to evaluate analytically even if $A_n(\xi)$ is a simple function. However, the calculations can be reduced to a relatively simple process. First, let equation (18) be expressed in terms of the dimensionless variables $\bar{x}, \bar{\xi}$, and $\bar{r}$ where

$$\left.\begin{aligned} \bar{x}&=x/L_o \\ \bar{\xi}&=\xi/L_o \\ \bar{r}&=\beta r/L_o \end{aligned}\right\} \tag{C1}$$

Then

$$\varphi_0(\bar{x},\bar{r},\theta)=-\frac{1}{2\pi}\int_{-1}^{\bar{x}-\bar{r}}\frac{A_o(\bar{\xi})d\bar{\xi}}{\sqrt{(\bar{x}-\bar{\xi})^2-\bar{r}^2}} \tag{C2a}$$

$$\varphi_2(\bar{x},\bar{r},\theta)=-\frac{\cos 2\theta}{2\pi}\int_{-1}^{\bar{x}-\bar{r}}\frac{A_2(\bar{\xi})[2(\bar{x}-\bar{\xi})^2-\bar{r}^2]d\bar{\xi}}{\bar{r}^2\sqrt{(\bar{x}-\bar{\xi})^2-\bar{r}^2}} \tag{C2b}$$

and so forth. Consider next the variation of $A_n(\bar{\xi})$ shown in figure 43 and represented by the equation

$$A_n(\bar{\xi})=\begin{cases}(190n-360m)+(390n-760m)\bar{\xi}+(200n-400m)\bar{\xi}^2, & -1\leq\bar{\xi}\leq-0.9 \\ n, & -0.9\leq\bar{\xi}\end{cases} \tag{C3}$$

As seen in the figure, A_n vanishes at $\bar{\xi}=-1$, is a parabola between -1 and -0.9 (assuming the values m at $\bar{\xi}=-0.95$ and n at $\bar{\xi}=-0.9$), and the straight line, $A_n(\bar{\xi})=n$, for $\bar{\xi}$ greater than -0.9. The velocities induced by a multipole distribution given by equation (C3) can be calculated in a straightforward manner in the two regions $-1+\bar{r}\leq\bar{x}\leq-0.9+\bar{r}$ and $-0.9+\bar{r}\leq\bar{x}$. For example, if

$$\frac{\pi\bar{r}M_{\sigma_r}(\bar{x})}{200}=\begin{cases}-(\bar{x}+0.9)\sqrt{(\bar{x}+1.0)^2-\bar{r}^2}+\bar{r}^2 1n\dfrac{\bar{x}+1.0+\sqrt{(\bar{x}+1.0)^2-\bar{r}^2}}{\bar{r}}, & -1+\bar{r}<\bar{x}<-0.9+\bar{r} \\[2ex] -(\bar{x}+0.9)\sqrt{(\bar{x}+1.0)^2-\bar{r}^2}+(\bar{x}+1.0)\sqrt{(\bar{x}+0.9)^2-\bar{r}^2}+\bar{r}^2 1n\dfrac{\bar{x}+1.0+\sqrt{(\bar{x}+1.0)^2-\bar{r}^2}}{\bar{x}+0.9+\sqrt{(\bar{x}+0.9)^2-\bar{r}^2}}, & -0.9+\bar{r}<\bar{x}\end{cases} \tag{C4}$$

$$\frac{\pi\bar{r}N_{\sigma_r}(x)}{100}=\begin{cases}(\bar{x}+0.95)\sqrt{(\bar{x}+1.0)^2-\bar{r}^2}-\bar{r}^2 1n\dfrac{\bar{x}+1.0+\sqrt{(\bar{x}+1.0)^2-\bar{r}^2}}{\bar{r}}, & -1+\bar{r}<\bar{x}<-0.9+\bar{r} \\[2ex] (\bar{x}+0.95)\sqrt{(\bar{x}+1.0)^2-\bar{r}^2}-(\bar{x}+1.05)\sqrt{(\bar{x}+0.9)^2-\bar{r}^2}-\bar{r}^2 1n\dfrac{\bar{x}+1.0+\sqrt{(\bar{x}+1.0)^2-\bar{r}^2}}{\bar{x}+0.9+\sqrt{(\bar{x}+0.9)^2-\bar{r}^2}}, & -0.9+\bar{r}<\bar{x}\end{cases} \tag{C5}$$

then φ_{σ_r} can be written

$$\varphi_{\sigma_r}=mM_{\sigma_r}(\bar{x})+nN_{\sigma_r}(\bar{x}) \tag{C6}$$

Now, if one is given a distribution of sources that is composed of, or is adequately approximated by, a series of 20 equally spaced parabolic arcs, equation (C6) can be used for each individual arc and the results superimposed for the complete solution. To this effect, define m_i and n_i in terms of $A_o(x)$ by

$$\left.\begin{aligned}m_i&=A_o\left(\frac{i-0.5}{10}-1\right)-A_o\left(\frac{i-1}{10}-1\right) \\ n_i&=A_o\left(\frac{i}{10}-1\right)-A_o\left(\frac{i-1}{10}-1\right)\end{aligned}\right\} \tag{C7}$$

so they represent the magnitudes shown in figure 44. Then, if $[\bar{x}]$ denotes the greatest interger contained in $\bar{x}$(e. g., $[6.34]$ equals 6), the equation for the radial velocity becomes

$$\varphi_{\sigma_r}=\sum_{i=1}^{[10(\bar{x}-r)+11]}\left[m_iM_{\sigma_r}\left(\bar{x}-\frac{i-1}{10}\right)+n_iN_{\sigma_r}\left(\bar{x}-\frac{i-1}{10}\right)\right] \tag{C8}$$

Values of M_{σ_r} and N_{σ_r} are tabulated in table I for $\bar{r}$ equal to 0.074, 0.148, 0.222, and 0.296. The asymptotic magnitudes of these functions are given by slender-body theory. Hence, one can easily show for large $\bar{x}$

$$\left.\begin{aligned}M_{\sigma_r}&\approx 0 \\ N_{\sigma_r}&\approx\frac{1}{2\pi\bar{r}}\end{aligned}\right\} \tag{C9}$$
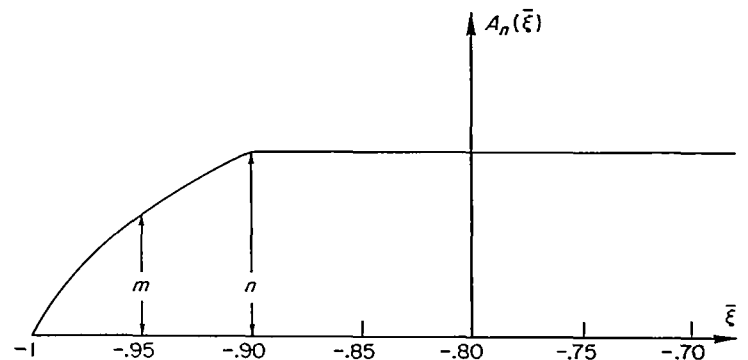
FIGURE 43.—Definition of symbols used in equations (C3) and (C6.)
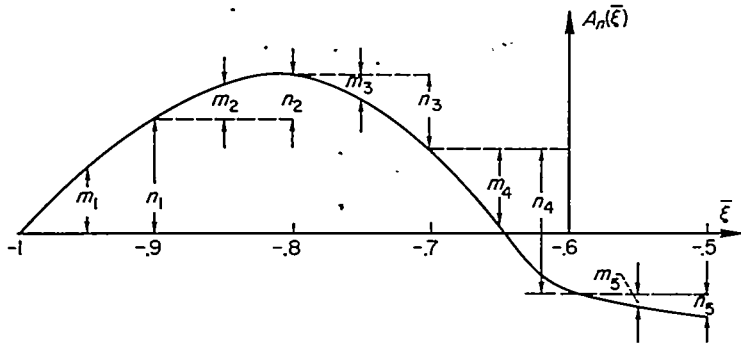
FIGURE 44.—Definition of symbols used in equation (C7).

Notice that both functions have essentially reached their asymptotic values for large x by the time $\bar{x}=-1+\bar{r}+0.5$. By applying simple tabulative procedures to equation (C8)—for example, listing m_i and n_i in reverse order and accumulating multiplications of adjacent terms—the value of $\varphi_{\sigma_{\bar{r}}}$ for any $A_o(\bar{x})$ representable by equation (C7) is readily calculated.

The velocities induced by higher order multipoles can be calculated in a similar fashion. Because of the asymptotic behavior of the M's and N's, however, one is led into the numerically inefficient process of obtaining small numbers from differences of large numbers. For the velocities φ_r and φ_θ, the following is a method for circumventing this difficulty.

It follows from equations (9) or (19), that for small $\bar{r}$, $\varphi_{n_{\bar{r}}}$ and φ_{n_θ} can be expressed in terms of the multipole strengths $a_n(\bar{x})$—as defined by equation (7)— by the equations

$$r^{n+1}\left(\frac{\varphi_{n_r}}{\cos n\theta}\right)=C_o+C_1r+\ldots+C_\nu r^\nu+\ldots \qquad (C10a)$$

$$r^{n+1}\left(\frac{\varphi_{n_\theta}}{r\sin n\theta}\right)=D_o+D_1r+\ldots+D_\nu r^\nu+\ldots \qquad (C10b)$$

where for $\nu\leq n$, $n\geq1$

$$C_\nu=\begin{cases}\dfrac{(-1)^{n+\frac{\nu}{2}}\beta^\nu 2^{n-\nu}}{4\pi}\dfrac{(n-\nu)\Gamma\left(n-\dfrac{\nu}{2}\right)}{\Gamma\left(1+\dfrac{\nu}{2}\right)}a_n^{(\nu)}(x), & \nu \text{ even} \quad (C11a)\\[2ex] 0 & , \nu \text{ odd}\end{cases}$$

$$D_\nu=\begin{cases}\dfrac{(-1)^{n+\frac{\nu}{2}}\beta^\nu 2^{n-\nu}}{4\pi}\dfrac{n\Gamma\left(n-\dfrac{\nu}{2}\right)}{\Gamma\left(1+\dfrac{\nu}{2}\right)}a_n^{(\nu)}(x), & \nu \text{ even} \quad (C11b)\\[2ex] 0 & , \nu \text{ odd}\end{cases}$$

Consider now the velocities $\varphi_{2_{\bar{r}}}$ and φ_{2_θ} induced by the multipole strength defined by equation (C3); thus

$$\frac{\varphi_{2_{\bar{r}}}}{\cos 2\theta}=mM_{2_{\bar{r}}}(\bar{x})+nN_{2_{\bar{r}}}(\bar{x}) \qquad (C12a)$$

$$\frac{\varphi_{2_\theta}}{\bar{r}\sin 2\theta}=mM_{2_\theta}(\bar{x})+nN_{2_\theta}(\bar{x}) \qquad (C12b)$$

where values of the M's and N's are listed in tables II and III. Their asymptotic values, as given by equations (C10) and (C11), are

$$\left.\begin{array}{l}M_{2_{\bar{r}}}=\dfrac{19+20\bar{x}}{150\pi\bar{r}^3}\\[2ex]N_{2_{\bar{r}}}=\dfrac{150\bar{x}^2+275\bar{x}+126}{150\pi\bar{r}^3}\\[2ex]M_{2_\theta}=\dfrac{19+20\bar{x}}{150\pi\bar{r}^3}\\[2ex]N_{2_\theta}=\dfrac{150\bar{x}^2+275\bar{x}+126}{150\pi\bar{r}^3}-\dfrac{1}{2\pi\bar{r}}\end{array}\right\} \qquad (C13)$$

and these are also given in the tables.

As the tables show, equations (C13) are sufficiently accurate approximations to M and N for practical calculating purposes when $\bar{x}>-1+\bar{r}+0.5$. Hence, the velocities at the point $\bar{x},\bar{r}$ induced by the multipoles in the interval $-1<\xi<\bar{x}-\bar{r}-0.5$ can be calculated using equations (C13). In terms of the distribution for $A_2(\xi)$—which is equal to $a_2^{(2)}(\bar{\xi})$, see equation (16)—this means the multipole distribution shown in the upper part of figure 45 can be calculated by means of the asymptotic formulas and the result added to that obtained for the distribution shown in the lower part of figure 45 by use of equations (C12b) and tables II and III in a manner identical to the one represented by equations (C6), (C7), and (C8).

The value of $\varphi_{2_\theta}(\bar{x},\bar{r})$ induced by a multipole distribution such as that shown in the upper part of figure 45 is, on the basis of equations (C10) and (C11),

$$\frac{\varphi_{2_\theta}}{\bar{r}\sin 2\theta}=H(\bar{x},\bar{r})=\frac{2}{\pi\bar{r}^3}\int_{-1}^{\bar{x}}(\bar{x}-\xi)A_2(\xi)d\xi-\frac{A_2(\bar{x})}{2\pi\bar{r}}$$

so

$$H(\bar{x},\bar{r})=\frac{2}{\pi\bar{r}^3}a_2(\bar{x}-\bar{r}-\bar{x}_i)+\frac{2(\bar{r}+\bar{x}_i)}{\pi\bar{r}^3}a_2^{(1)}(\bar{x}-\bar{r}-\bar{x}_i)+$$
$$a_2^{(2)}(\bar{x}-\bar{r}-\bar{x}_i)\left[\frac{(\bar{r}+\bar{x}_i)^2}{\pi\bar{r}^3}-\frac{1}{2\pi\bar{r}}\right] \qquad (C14)$$

FIGURE 45.—Range of application of equations (C12) and (C13).

where $\beta^2 a_2^{(2)}(x) = A_2(x)$ and x_i is shown in figure 45 and defined by the equation

$$\bar{x}_i = 0.4 + \bar{x} - \bar{r} - \frac{[10(\bar{x}-\bar{r})]}{10} \tag{C15}$$

the symbol $[10(\bar{x}-\bar{r})]$ meaning, as before, the highest integer value contained in $10(\bar{x}-\bar{r})$. A similar result can be derived for $\varphi_{2\bar{r}}$ and one has finally for $-1 \leq [10(\bar{x}-\bar{r})+11] \leq 5$
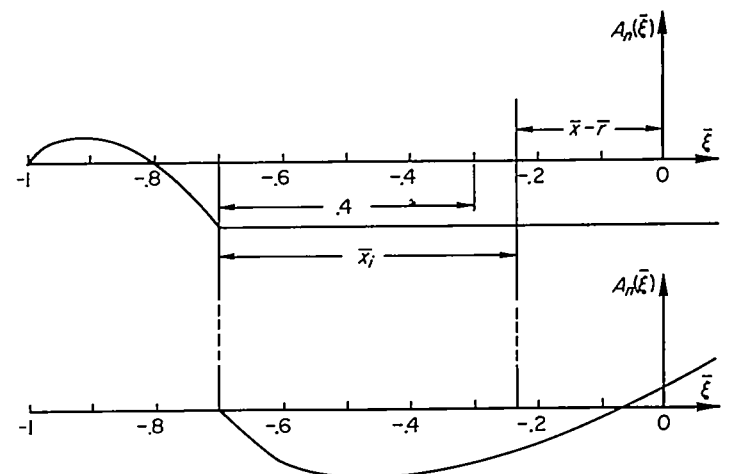
$$\frac{\varphi_{2\theta}(\bar{x})}{\bar{r} \sin 2\theta} = \sum_1^{[10(\bar{x}-\bar{r})+11]} \left[m_i M_{2\theta}\left(\bar{x} - \frac{i-1}{10}\right) + n_i N_{2\theta}\left(\bar{x} - \frac{i-1}{10}\right) \right] \tag{C16a}$$

$$\frac{\varphi_{2\bar{r}}(\bar{x})}{\cos 2\theta} = \sum_1^{[10(\bar{x}-\bar{r})+11]} \left[m_i M_{2\bar{r}}\left(\bar{x} - \frac{i-1}{10}\right) + n_i N_{2\bar{r}}\left(\bar{x} - \frac{i-1}{10}\right) \right] \tag{C16b}$$

and for $[10(\bar{x}-\bar{r})+11] \geq 6$

$$\frac{\varphi_{2\theta}(\bar{x})}{\bar{r} \sin 2\theta} = \sum_{[10(\bar{x}-\bar{r})+11]-5}^{[10(\bar{x}-\bar{r})+11]} \left[m_i M_{2\theta}\left(\bar{x} - \frac{i-1}{10}\right) + n_i N_{2\theta}\left(\bar{x} - \frac{i-1}{10}\right) \right] + H(\bar{x},\bar{r}) \tag{C17a}$$

$$\frac{\varphi_{2\bar{r}}(\bar{x})}{\cos 2\theta} = \sum_{[10(\bar{x}-\bar{r})+11]-5}^{[10(\bar{x}-\bar{r})+11]} \left[m_i M_{2\bar{r}}\left(\bar{x} - \frac{i-1}{10}\right) + n_i N_{2\bar{r}}\left(\bar{x} - \frac{i-1}{10}\right) \right] + H(\bar{x},\bar{r}) - \frac{A_2(\bar{x}-\bar{r}-\bar{x}_i)}{2\pi\bar{r}} \tag{C17b}$$

The streamwise gradients of induced velocities can also be defined in terms of M's and N's as were the velocities $\varphi_{\bar{r}}$ and $\frac{1}{\bar{r}}\varphi_\theta$. Thus

$$\varphi_{o\bar{x}} = m M_{o\bar{x}} + n N_{o\bar{x}}$$

$$\frac{\varphi_{2\bar{x}}}{\cos 2\theta} = m M_{2\bar{x}} + n N_{2\bar{x}}$$

Values of $M_{o\bar{x}}$, $N_{o\bar{x}}$, $M_{2\bar{x}}$, and $N_{2\bar{x}}$ for $\bar{r}$ equal to 0.148, 0.222, and 0.296 are given in tables IV and V.

APPENDIX D

NUMERICAL METHOD USED TO CALCULATE BODY SHAPE

The method used to calculate the body shape was a standard step-by-step solution to the two simultaneous total differential equations (eq. (43) in the text)

$$\left.\begin{array}{l} \dfrac{d\theta}{dx} = \dfrac{1}{U_o \bar{R}^2}\, \varphi_\theta(x,R,\theta) \\[2ex] \dfrac{dR}{dx} = \dfrac{1}{U_o}\, \varphi_r(x,R,\theta) \end{array}\right\} \tag{D1}$$

The essentials of the process are recognized from the following computing-sheet heading set up for initial values of θ and $\bar{R}$ equal to 30° and 0.148, respectively, where $\bar{x}=x/L_o$ and $\bar{R}=\beta R/L_o$

①	②	③	④	⑤	⑥	⑦
n	$\bar{x}$	$\dfrac{⑥_n \times 0.05 +}{③_{n-1}}$ θ	$\dfrac{⑫_n \times 0.05 +}{④_{n-1}}$ $\bar{R}$	$\left(\dfrac{1}{U_o}\dfrac{\partial \varphi}{\partial \theta}\right)$ for ③ and ④	$\left(\dfrac{d\theta}{dx}\right)_1$ $\dfrac{⑤}{④^3}$	$\left(\dfrac{1}{U_o}\dfrac{\partial \varphi}{\partial r}\right)$ for ③ and ④
0	−0.852	0.524	0.148	--------	--------	--------
1	−.802	----------	----------	--------	--------	--------
2	−.752	----------	----------	--------	--------	--------

⑧	⑨	⑩	⑪	⑫	⑬	⑭
$\dfrac{⑥_{n-1} \times 0.05 +}{③_{n-1}}$ θ_1	$\dfrac{⑭_{n-1} \times 0.05 +}{④_{n-1}}$ $\bar{R}_1$	$\left(\dfrac{1}{U_o}\dfrac{\partial \varphi}{\partial \theta}\right)$ for ⑧ and ⑨	$\left(\dfrac{d\theta}{dx}\right)_2$ $\dfrac{⑩}{⑨^3}$	$\left(\dfrac{1}{U_o}\dfrac{\partial \varphi}{\partial r}\right)$ for ⑧ and ⑨	$\left(\dfrac{d\theta}{dx}\right)_{av}$ $\dfrac{⑥_{n-1}+⑪_n}{2}$	$\left(\dfrac{d\bar{R}}{dx}\right)_{av}$ $\dfrac{⑦_{n-1}+⑫_n}{2}$
----------	----------	-------	----	------	----------	----------

APPENDIX E

OPTIMUM VARIATION OF $\alpha_2(x)$ FOR A FIXED VALUE OF $\int_{-L_o}^0 \alpha_2(x)\, dx$

Given

$$D_2 = -\frac{q}{4\pi U_o^2} \int_{-L_o}^{L_o} \int_{-L_o}^{L_o} [a_2^{(3)}(x_1) + \alpha_2^{(3)}(x_1)][a_2^{(3)}(x_2) + \alpha_2^{(3)}(x_2)]$$

$$\ln\left|\frac{x_1-x_2}{L_o}\right| dx_1 dx_2 \tag{E1}$$

where the variation of $a_2^{(3)}(x)$ is fixed, pose the restraint

$$\frac{1}{U_o} \int_{-L_o}^0 \alpha_2(x)\, dx = F^*(0)\frac{\pi}{4} R_o^4 = \text{constant} \tag{E2}$$

and ask for the function $\alpha_2(x)$ which minimizes D_2 for a given value of the constant.

If $f(x)=f(-x)$, then

$$\int_{-1}^1 \int_{-1}^1 f(x_1)f(x_2)\ln|x_1-x_2| dx_1 dx_2$$

$$= 2 \int_{-1}^0 \int_{-1}^0 f(x_1)f(x_2)\ln|x_1^2-x_2^2| dx_1 dx_2$$

and since $\alpha_2(-L_o)=\alpha_2^{(1)}(-L_o)=\alpha_2^{(-2)}(-L_o)=0$

$$\int_{-L_o}^0 \alpha_2(x)\, dx = -\frac{1}{6}\int_{-L_o}^0 x^3 \alpha_2^{(3)}(x)\, dx$$

Therefore, the standard variational problem

$$\delta\left[D_2 + \lambda \int_{-L_o}^0 \frac{\alpha_2(x)}{U_o}\, dx\right] = 0 \tag{E3}$$

reduces to

$$\delta\left\{\frac{-q}{2\pi U_0^2}\int_{-L_o}^{0}\int_{-L_o}^{0}[a_2^{(3)}(x_1)+\alpha_2^{(3)}(x_1)]\,[a_2^{(3)}(x_2)+\alpha_2^{(3)}(x_2)]\right.$$
$$\left. 1n\left|\frac{x_1^2-x_2^2}{L_o^2}\right|dx_1dx_2-\frac{\lambda}{6U_o}\int_{-L_o}^{0}x_1^3\alpha_2^{(3)}(x_1)dx_1\right\}=0$$

and this becomes

$$\int_{-L_o}^{0}\delta\left[\frac{\alpha_2^{(3)}(x_1)}{U_0}\right]dx_1\left\{\frac{q}{\pi U_0}\int_{-L_o}^{0}[\alpha_2^{(3)}(x_2)+\alpha_2^{(3)}(x_2)]\right.$$
$$\left. 1n\left|\frac{x_1^2-x_2^2}{L_o^2}\right|dx_2+\frac{\lambda x_1^3}{6}\right\}=0$$

Integrating three times by parts, using the relations

$$\delta\alpha_2(-L_o)=\delta\alpha_2^{(1)}(-L_o)=\delta\alpha_2^{(2)}(-L_o)=0$$

$$\delta\alpha_2(0)=\delta\alpha_2^{(2)}(0)=0,\text{ by symmetry}$$

and

$$\lim_{n\to 0}\frac{\partial}{\partial x_1}\int_{-L_o}^{0}[a_2^{(3)}(x_2)+\alpha_2^{(3)}(x_2)]\,1n\left|\frac{x_1^2-x_2^2}{L_o^2}\right|dx_2$$
$$=\lim_{x_1\to 0}2x_1\int_{-L_c}^{0}\frac{a_2^{(3)}(x_2)+\alpha_2^{(3)}(x_2)}{x_1-x_2}dx_2=0$$

yields

$$\int_{-L_o}^{0}\delta\left[\frac{\alpha_2(x_1)}{U_o}\right]dx_1\frac{\partial^3}{\partial x_1^3}\left\{\int_{-L_o}^{0}[a_2^{(3)}(x_2)+\alpha_2^{(3)}(x_2)]\right.$$
$$\left. 1n\left|\frac{x_1^2-x_2^2}{L_o^2}\right|dx_2+U_o\lambda_o x_1^3\right\}=0$$

where

$$\lambda_0=\frac{\lambda\pi}{6q} \tag{E4}$$

By the fundamental lemma of the calculus of variations

$$\frac{\partial^3}{\partial x_1^3}\left\{\int_{-L_o}^{0}[a_2^{(3)}(x_2)+\alpha_2^{(3)}(x_2)]\,1n\left|\frac{x_1^2-x_2^2}{L_o^2}\right|dx_2+U_o\lambda_o x_1^3\right\}=0,$$
$$0>x_1>-L_o$$

One can also show

$$\frac{\partial^3}{\partial x_1^3}\left\{\int_{0}^{L_o}[a_2^{(3)}(x_2)+\alpha_2^{(3)}(x_2)]\,1n\left|\frac{x_1^2-x_2^2}{L_o^2}\right|dx_2-U_o\lambda_o x_1^3\right\}=0,$$
$$L_o>x_1>0$$

Hence,

$$\int_{-L_o}^{0}\frac{\alpha_2^{(3)}(x_2)}{U_0}1n\left|\frac{x_1^2-x_2^2}{L_o^2}\right|dx_2=\gamma_o+\gamma_2 x_1^2-\lambda_o x_1^3$$

$$\int_{-L_o}^{0}\frac{a_2^{(3)}(x_2)}{U_o}1n\left|\frac{x_1^2-x_2^2}{L_o^2}\right|dx_2 \tag{E5}$$

Integrating by parts and changing the notation so that

$$\eta_2=\frac{x_2^2}{L_o^2},\qquad f(\eta_2)=\frac{a_2^{(2)}(x_2)}{U_o}$$

$$\eta_1=\frac{x_1^2}{L_o^2},\qquad g(\eta_2)=\frac{a_2^{(2)}(x_2)}{U_o}$$

one has

$$\int_{0}^{1}\frac{f(\eta_2)d\eta_2}{\eta_1-\eta_2}=\gamma_o+\gamma_2\eta_1-\lambda_o\eta_1^{3/2}-\int_{0}^{1}\frac{g(\eta_2)d\eta_2}{\eta_1-\eta_2} \tag{E6}$$

Equation (E6) is the familiar singular integral equation known, in aerodynamic applications, as the airfoil equation. Its inversion is discussed, for example, in reference 3. If one solves equation (E6) and applies the conditions

$$a_2^{(2)}(0)=a_2^{(2)}(L_o)=0$$

then

$$\gamma_o=-\frac{4\lambda_o L_0^3}{15\pi},\qquad \gamma_2=\frac{48\lambda_o L_o}{15\pi}$$

and

$$\frac{\alpha_2(x)}{U_o}+\frac{a_2(x)}{U_o}=\frac{\lambda_o L_o^4 x}{60\pi^2}\left\{\left[10\left(\frac{x}{L_o}\right)^2-4\right]\sqrt{1-\left(\frac{x}{L_o}\right)^2}+\right.$$
$$\left. 3\left(\frac{x}{L_o}\right)^4 1n\frac{L_o-\sqrt{L_o^2-x^2}}{L_o+\sqrt{L_o^2-x^2}}\right\} \tag{E7}$$

Now set

$$\int_{-L_o}^{0}\frac{a_2(x)}{U_o}dx=F_w^*(0)\frac{\pi}{4}R_c^4 \tag{E8}$$

so that $F_w^*(0)$ is a known constant. Then

$$\int_{-L_o}^{0}\frac{\alpha_2(x)dx}{U_o}=F^*(0)\frac{\pi}{4}R_c^4=-F_w^*(0)\frac{\pi}{4}R_o^4+\frac{2\lambda_o L_o^6}{225\pi^2} \tag{E9}$$

Using the above expressions, one can show

$$\frac{\alpha_2(x)}{U_o}+\frac{a_2(x)}{U_o}=\frac{15\pi R_c^4 x}{32L_o^2}[F^*(0)+F_w^*(0)]$$

$$\left\{\left[10\left(\frac{x}{L_o}\right)^2-4\right]\sqrt{1-\left(\frac{x}{L_o}\right)^2}+3\left(\frac{x}{L_o}\right)^4 1n\frac{L_o-\sqrt{L_o^2-x^2}}{L_o+\sqrt{L_o^2-x^2}}\right\} \tag{E10}$$

The wave drag can be calculated by combining equations (E5) and (E1).

$$D_2=-\frac{q}{2\pi}\int_{0}^{L_o}(\gamma_o+\gamma_2 x_1^2-\lambda_o x_1^3)\left[\frac{a_2^{(3)}(x_1)}{U_o}+\frac{\alpha_2^{(3)}(x_1)}{U_o}\right]dx_1$$

Integrate three times by parts and there results, finally

$$D_2=\frac{675}{32}qL_o^2\pi^3\left(\frac{R_c}{L_o}\right)^4[F^*(0)+F_w^*(0)]^2 \tag{E11}$$

REFERENCES

1. Heaslet, Max. A., Lomax, Harvard, and Spreiter, John R.: Linearized Compressible-Flow Theory for Sonic Flight Speeds. NACA Rep. 956, 1950.
2. Lamb, Horace: Hydrodynamics. Sixth ed., Dover Publication (New York), 1945
3. Lomax, Harvard, Heaslet, Max. A., and Fuller, Franklyn B.: Integrals and Integral Equations in Linearized Wing Theory. NACA Rep. 1054, 1951.
4. Watson, G. N.: A Treatise on the Theory of Bessel Functions. Second ed., Cambridge Univ. Press (Cambridge, England), 1952.

5. Erdélyi, Arthur: Table of Integral Transforms. Vol. I, McGraw-Hill Book Co., Inc., 1954.

6. Hayes, Wallace D.: Linearized Supersonic Flow. North American Aviation, Inc., Rep. No. AL-222, June 1947.

7. Lomax, Harvard, and Heaslet, Max. A.: Recent Developments in the Theory of Wing-Body Wave Drag. IAS Preprint 617, 1956.

8. von Kármán, Th.: The Problem of Resistance in Compressible Fluids. (Fifth Volta Congress) Roma Reale Accademia D'Italia 1936.

9. Webster, Arthur Gordon: Partial Differential Equations of Mathematical Physics. Second ed., Hafner Publishing Co., Inc. (New York), 1950.

10. Nielsen, Jack N., and Pitts, William C.: General Theory of Wave-Drag Reduction for Combinations Employing Quasi-Cylindrical Bodies With an Application to Swept Wing and Body Combinations. NACA TN 3722, 1956. (Formerly NACA RM A55B07).

11. Jones, Robert T.: Theoretical Determination of the Minimum Drag of Airfoils at Supersonic Speeds. Jour. Aero. Sic., vol. 19, no. 12, Dec. 1952, pp. 813-822.

12. Jones, Robert T.: Theory of Wing-Body Drag at Supersonic Speeds. NACA RM A53H18a, 1953.

13. Lomax, Harvard: The Wave Drag of Arbitrary Configurations in Linearized Flow as Determined by Areas and Forces in Oblique Planes. NACA RM A55A18, 1955.

14. Nielsen, Jack N., and Pitts, William C.: Wing-Body Interference at Supersonic Speeds With an Application to Combinations With Rectangular Wings. NACA TN 2677, 1952.

15. Jones, Robert T.: Some Recent Developments in the Aerodynamics of Wings for High Speeds. Zeitschrift Für Flugwissenschaften, 4. Jahr., Heft 8, Aug. 1956, pp. 257-262.

16. Graham, Ernest W.: The Pressure on a Slender Body of Non-Uniform Cross-Sectional Shape in Axial Supersonic Flow. Douglas Aircraft Co., Inc., Rep. No. SM-13346-A, July 1949.

TABLE I.—VALUES OF $M_{\sigma\bar{r}}$ AND $N_{\sigma\bar{r}}$.

x	$M_{\sigma\bar{r}}$ Exact	$M_{\sigma\bar{r}}$ Asymptotic	$N_{\sigma\bar{r}}$ Exact	$N_{\sigma\bar{r}}$ Asymptotic	x	$M_{\sigma\bar{r}}$ Exact	$M_{\sigma\bar{r}}$ Asymptotic	$N_{\sigma\bar{r}}$ Exact	$N_{\sigma\bar{r}}$ Asymptotic
	$\bar{r}=0.074$					$\bar{r}=0.148$			
-0.926	0	----	0	----	-0.852	0	----	0	-----
-.876	3.16	----	.56	----	-.802	2.00	----	.42	-----
-.826	-2.96	----	4.86	----	-.752	-2.26	----	3.24	-----
-.776	-.24	----	2.52	----	-.702	-.22	----	1.50	-----
-.726	-.08	----	2.34	----	-.652	-.10	----	1.30	-----
-.676	-.04	----	2.26	----	-.602	-.06	----	1.20	-----
-.626	-.02	----	2.22	----	-.552	-.04	----	1.18	-----
-.576	-.02	----	2.20	----	-.502	-.02	----	1.14	-----
-.526	-.02	0	2.20	2.15	-.452	-.02	0	1.14	1.08
-.476	0	0	2.18	2.15	-.402	0	0	1.12	1.08
-.426	0	0	2.18	2.15	-.352	0	0	1.10	1.08
	$\bar{r}=0.222$					$\bar{r}=0.296$			
-0.778	0	----	0	----	-0.704	0	----	0	-----
-.728	1.56	----	.34	----	-.654	1.32	----	.30	-----
-.678	-1.90	----	2.62	----	-.604	-1.66	----	2.24	-----
-.628	-.22	----	1.13	----	-.554	-.20	----	.92	-----
-.578	-.10	----	.94	----	-.504	-.03	----	.78	-----
-.523	-.06	----	.88	----	-.454	-.06	----	.70	-----
-.478	-.04	----	.84	----	-.404	-.04	----	.66	-----
-.428	-.02	----	.80	----	-.354	-.02	----	.64	-----
-.378	-.02	0	.78	0.72	-.304	-.02	0	.62	0.54
-.328	-.02	0	.78	.72	-.254	-.02	0	.60	.54
-.278	0	0	.76	.72	-.204	0	0	.60	.54

TABLE II.—VALUES OF $M_{x\bar{r}}$ AND $N_{x\bar{r}}$.

x	$M_{x\bar{r}}$ Exact	$M_{x\bar{r}}$ Asymptotic	$N_{x\bar{r}}$ Exact	$N_{x\bar{r}}$ Asymptotic	x	$M_{x\bar{r}}$ Exact	$M_{x\bar{r}}$ Asymptotic	$N_{x\bar{r}}$ Exact	$N_{x\bar{r}}$ Asymptotic
	$\bar{r}=0.074$					$\bar{r}=0.148$			
-0.926	0	----	0	----	-0.852	0	----	0	----
-.876	9.77	----	-.16	----	-.802	3.86	----	2.31	----
-.826	10.61	----	8.31	----	-.752	.03	----	4.38	----
-.776	18.09	----	15.53	----	-.702	3.11	----	4.73	----
-.726	23.44	----	28.41	----	-.652	3.85	----	6.97	----
-.676	28.72	----	45.32	----	-.602	4.53	----	9.77	----
-.626	33.95	----	66.17	----	-.552	5.19	----	13.08	----
-.576	39.15	----	90.98	----	-.502	5.85	----	16.90	----
-.526	44.38	44.41	119.70	119.66	-.452	6.51	6.52	21.20	21.17
-.476	49.62	49.64	152.35	152.32	-.402	7.17	7.17	26.01	25.98
-.426	54.87	54.88	188.91	188.89	-.352	7.83	7.83	31.30	31.23
	$\bar{r}=0.222$					$\bar{r}=0.296$			
-0.778	0	----	0	----	-0.704	0	----	0	----
-.728	2.49	----	.26	----	-.654	1.90	----	.25	----
-.678	-.60	----	3.20	----	-.604	-.92	----	2.02	----
-.628	1.11	----	2.66	----	-.554	.51	----	1.86	----
-.578	1.38	----	3.46	----	-.504	.67	----	2.22	----
-.523	1.61	----	4.47	----	-.454	.78	----	2.72	----
-.478	1.81	----	5.65	----	-.404	.87	----	3.29	----
-.423	2.01	----	6.99	----	-.354	.96	----	3.93	----
-.378	2.21	2.22	8.47	8.44	-.304	1.05	1.00	4.04	4.00
-.323	2.40	2.41	10.10	10.07	-.254	1.13	1.14	5.42	5.39
-.278	2.60	2.61	11.88	11.86	-.204	1.22	1.22	6.20	6.23

TABLE III.—VALUES OF $M_{2\theta}$ AND $N_{2\theta}$.

x	$M_{2\theta}$ Exact	$M_{2\theta}$ Asymptotic	$N_{2\theta}$ Exact	$N_{2\theta}$ Asymptotic	x	$M_{2\theta}$ Exact	$M_{2\theta}$ Asymptotic	$N_{2\theta}$ Exact	$N_{2\theta}$ Asymptotic
	$\bar{r}=0.074$					$\bar{r}=0.148$			
-0.926	0	--------	0	--------	-0.852	0	--------	0	--------
-.876	6.62	--------	-.73	--------	-.802	1.86	--------	-.19	--------
-.826	13.59	--------	3.42	--------	-.752	2.93	--------	1.11	--------
-.776	18.38	--------	12.97	--------	-.702	3.34	--------	3.25	--------
-.726	23.48	--------	26.12	--------	-.652	3.93	--------	5.68	--------
-.676	28.70	--------	43.10	--------	-.602	4.58	--------	8.55	--------
-.626	33.92	--------	63.97	--------	-.553	5.22	--------	11.91	--------
-.576	39.15	--------	88.80	--------	-.502	5.89	--------	15.74	--------
-.526	44.47	44.41	117.48	117.51	-.452	6.49	6.52	20.07	20.09
-.476	49.63	49.64	150.15	150.17	-.402	7.16	7.17	24.89	24.90
-.426	54.85	54.88	186.77	186.74	-.352	7.83	7.83	30.18	30.20
	$\bar{r}=0.222$					$\bar{r}=0.296$			
-0.778	0	--------	0	--------	-0.704	0	--------	0	--------
-.728	.93	--------	-.09	--------	-.654	.58	--------	-.05	--------
-.678	1.29	--------	.59	--------	-.604	.74	--------	.37	--------
-.628	1.32	--------	1.54	--------	-.554	.71	--------	.93	--------
-.578	1.48	--------	2.51	--------	-.504	.76	--------	1.45	--------
-.528	1.66	--------	3.60	--------	-.454	.83	--------	2.02	--------
-.478	1.85	--------	4.82	--------	-.404	.91	--------	2.63	--------
-.423	2.04	--------	6.18	--------	-.354	.98	--------	3.29	--------
-.378	2.23	2.22	7.69	7.72	-.304	1.06	1.06	4.03	4.07
-.328	2.42	2.41	9.33	9.35	-.254	1.15	1.14	4.82	4.85
-.278	2.61	2.61	11.11	11.14	-.204	1.23	1.22	5.67	5.69

TABLE IV.—VALUE OF $M_{\sigma\bar{x}}$ AND $N_{\sigma\bar{x}}$.

x	$M_{\sigma\bar{x}}$	$N_{\sigma\bar{x}}$	x	$M_{\sigma\bar{x}}$	$N_{\sigma\bar{x}}$	x	$M_{\sigma\bar{x}}$	$N_{\sigma\bar{x}}$
	$\bar{r}=0.148$			$\bar{r}=0.222$			$\bar{r}=0.296$	
-0.852	0	0	-0.778	0	0	-0.704	0	0
-.802	-1.663	-.442	-.723	-1.379	-.360	-.654	-1.204	-.311
-.752	2.529	-3.024	-.678	2.051	-2.435	-.604	1.769	-2.150
-.702	.369	-1.019	-.628	.297	-.859	-.554	.255	-.756
-.652	.191	-.723	-.578	.155	-.620	-.504	.133	-.552
-.602	.121	-.572	-.523	.099	-.498	-.454	.085	-.447
-.552	.095	-.477	-.478	.070	-.420	-.404	.061	-.380
-.502	.063	-.410	-.423	.053	-.365	-.354	.046	-.332
-.452	.049	-.361	-.378	.042	-.324	-.304	.036	-.290
-.402	.040	-.323	-.323	.034	-.292	-.254	.030	-.208
-.352	.033	-.292	-.278	.023	-.266	-.204	.025	-.246
-.302	.027	-.267	-.223	.024	-.243	-.154	.021	-.220
-.252	.023	-.245	-.178	.020	-.226	-.104	.018	-.210
-.202	.020	-.227	-.123	.018	-.210	-.054	.016	-.190
-.152	.018	-.212	-.073	.015	-.197	-.004	.014	-.184
-.102	.015	-.199	-.023	.014	-.185	.046	.012	-.174
-.052	.014	-.187	.022	.012	-.174	.096	.011	-.164
-.002	.012	-.176	.072	.011	-.165	.146	.010	-.150
.048	.011	-.167	.122	.010	-.157	.196	.009	-.148
.098	.010	-.158	.172	.009	-.149	.246	.008	-.141
.148	.009	-.151	.222	.008	-.142	.296	.007	-.135
.198	.008	-.144	.272	.007	-.136	.346	.007	-.130
.248	.007	-.138	.322	.007	-.131	.396	.000	-.124
.298	.007	-.132	.372	.006	-.125	.446	.000	-.120
.348	.006	-.127	.423	.006	-.120			
.398	.006	-.122						
.448	.005	-.117						

TABLE V.—VALUES OF $M_{x\bar{x}}$ AND $N_{x\bar{x}}$.

x	$M_{x\bar{x}}$ Exact	$M_{x\bar{x}}$ Asymptotic	$N_{x\bar{x}}$ Exact	$N_{x\bar{x}}$ Asymptotic	x	$M_{x\bar{x}}$ Exact	$M_{x\bar{x}}$ Asymptotic	$N_{x\bar{x}}$ Exact	$N_{x\bar{x}}$ Asymptotic	x	$M_{x\bar{x}}$ Exact	$M_{x\bar{x}}$ Asymptotic	$N_{x\bar{x}}$ Exact	$N_{x\bar{x}}$ Asymptotic
	$\bar{r}=0.148$					$\bar{r}=0.222$					$\bar{r}=0.296$			
-0.852	0	------	0	------	-0.778	0	--------	0	------	-0.704	0	---------	0	--------
-.802	-3.16	------	-.31	------	-.723	-2.18	--------	-.29	------	-.654	-1.72	---------	-.27	--------
-.752	.92	------	-4.05	------	-.678	1.22	--------	-3.04	------	-.604	1.25	---------	-2.52	--------
-.702	-.85	------	-3.23	------	-.623	-.30	--------	-2.05	------	-.554	-.11	---------	-1.52	--------
-.652	-.93	------	-3.91	------	-.578	-.38	--------	-2.27	------	-.504	-.19	---------	-1.60	--------
-.602	-.95	------	-4.61	------	-.523	-.41	--------	-2.56	------	-.454	-.22	---------	-1.74	--------
-.552	-.96	------	-5.23	------	-.478	-.42	--------	-2.86	------	-.404	-.23	---------	-1.90	--------
-.503	-.96	------	-6.04	------	-.423	-.42	--------	-3.18	------	-.354	-.23	---------	-2.07	--------
-.452	-.96	-0.97	-6.76	-6.75	-.378	-.42	-0.43	-3.49	-3.48	-.304	-.24	-0.24	-2.24	-2.23
-.403	-.97	-.97	-7.49	-7.49	-.323	-.43	-.43	-3.81	-3.80	-.254	-.24	-.24	-2.42	-2.41
-.352	-.97	-.97	-8.21	-8.21	-.278	-.43	-.43	-4.13	-4.12	-.204	-.24	-.24	-2.60	-2.59